# Optimal Control And Energy Management For Hybrid Aircraft

Kilian Swannet

May 20th, 2022

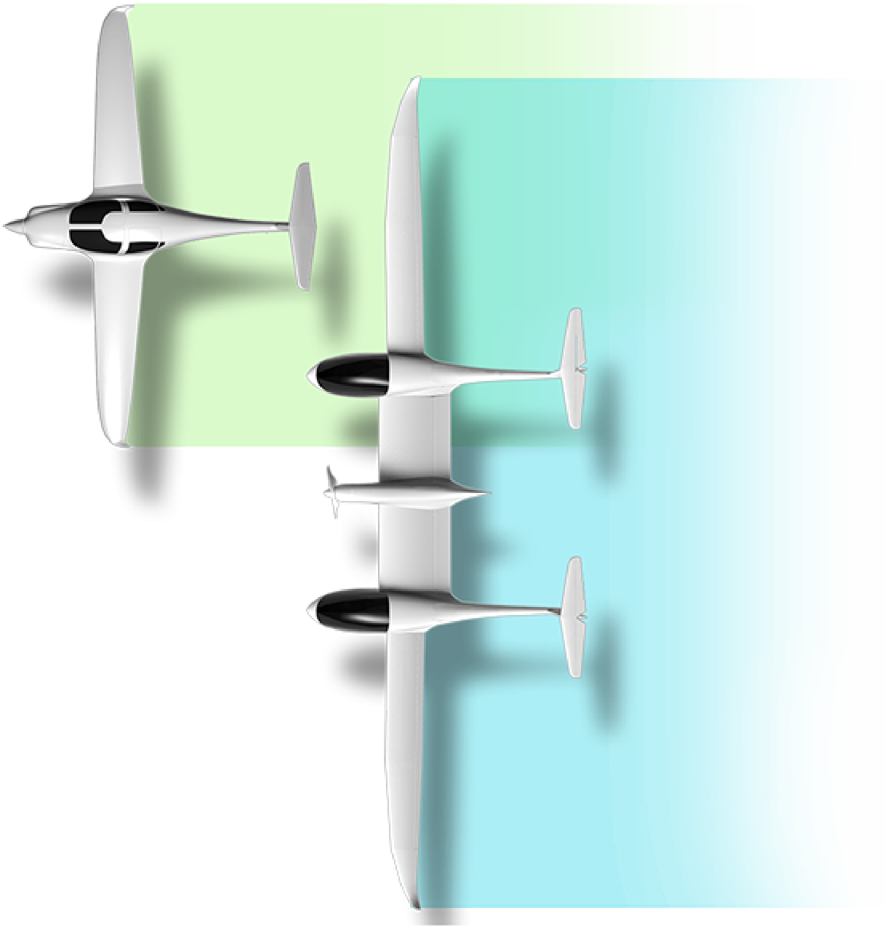

TU Delft

Delft University of Technology
Faculty of Aerospace Engineering

# Optimal Control And Energy Management For Hybrid Aircraft

by

Kilian Swannet

to obtain the degree of Master of Science in Aerospace Engineering
at the Delft University of Technology,
to be defended publicly on Tuesday May 31, 2022.

| | | |
|---|---|---|
| Student number: | 4359895 | |
| Project duration: | February 2021 – May 2022 | |
| Thesis committee: | Dr. F. Oliviero, | TU Delft, supervisor |
| | Dr. ir. G. La Rocca, | TU Delft, committee chair |
| | Dr. J. Sun, | TU Delft |
| | Dr. C. Varriale, | TU Delft |

Cover image from `mahepa.eu`.

# Preface

This work concludes my studies at the TU Delft's Faculty of Aerospace Engineering. It has been a long and laborious, yet formidable and rewarding journey. I can now finally say I achieved a childhood dream of becoming an aircraft designer! I am thankful to my supervisor, Dr. Fabrizio Oliviero, who guided me not only throughout my master's thesis, but also my bachelor's graduation project before it. I would like to acknowledge the help I received from Alessandro Porrini, who spent several hours on call with me to help decipher the many flight test data sets. Furthermore, my appreciation goes out to Dr. Ir. Gianfranco La Rocca, Dr. Junzi Sun, and Dr. Carmine Varriale for offering their time to serve on the thesis defense committee. Finally, I am grateful to my parents and family, for their continued support and patience throughout my studies, and all the friends I made along the way that made my studies memorable and fun. A special thanks goes to San, Miha, Yvonne, Michael, and Carlos, for continuously offering motivating, a listening ear, and making the many months of lockdown during the pandemic a little more bearable.

Kilian Swannet
Delft, May 2022

This page is intentionally left blank.

# Abstract

Interest grows rapidly in electric and hybrid electric aircraft. To determine the optimal performance and energy management required with such novel powertrain configurations, a knowledge-based aircraft and powertrain performance model is developed. The model is then used to set up an optimal control problem, which is transcribed to a non-linear programming problem using global orthogonal Legendre-Gauss-Radau collocation for single phase problems, and Hermite-Simpson local collocation for multiphase problems. The solution to the control problem allows identification of the best control strategies and energy management strategies. A case study is performed on the HY4 hybrid fuel cell aircraft and the hybrid electric Pipistrel Panthera. Solutions show that for best fuel economy, flying at a minimum drag airspeed, and keeping a constant power setting, proved more important than the choice of altitude. This was more noticeable for the HY4, with its relatively low power available and good aerodynamic properties following from its glider-based airframe. The Fuel-optimal energy management strategies proved identical for both aircraft investigated. Batteries are used to provide a power boost during takeoff, after which batteries are discharged gradually throughout the remainder of the flight to maximize discharge efficiency. The engine or fuel cell are kept at approximately constant cruise power settings throughout the flight. The Panthera showed consistent flight profiles with increasing range. For the HY4, however, achieved airspeeds reduced with increasing range, and additional measures were required to force a climb to non-zero altitudes due to its under-powered nature. The fuel-optimal trajectories offered an average of 10-15% of possible fuel savings, depending mostly on the size of the onboard batteries. Fuel savings increased significantly at low ranges (>300 km), where the contributions of the batteries have more impact.

Comparing different transcription methods and problem setups, it was concluded that global orthogonal, or pseudo-spectral, methods like Legendre-gauss-Radau collocation are not only faster, but also more consistent compared to simpler direct collocation methods. However, if the problem complexity increases and the performance limits of the aircraft are pushed, switching to a simpler method like Hermite-Simpson collocation reduced the time required to find a solution, with negligible differences in the resulting trajectories. Opting for a multiphase problem set-up, essentially splitting the problem in a series of individual subproblems, appeared less advantageous. While offering more control over the trajectories, time required to find solutions increased drastically, and offered no additional insight into the best energy management strategies.

This page is intentionally left blank.

# Table of Contents

# List of Symbols

## Abbreviations

| | |
|---|---|
| AC | Alternating current |
| BEMF | back electromotive force, or back EMF |
| CPS | Controlled power source |
| DLR | German Aerospace Center |
| DoD | Depth of discharge |
| EM | Electric motor |
| FC | Fuel cell (single MEA) |
| FCS | Fuel cell stack |
| GR | Gear ratio |
| HEP | Hybrid Electric Powertrain |
| HEPT | Hybrid Electric Powertrain |
| HFCP | Hybrid Fuel Cell Powertrain |
| HFCPT | Hybrid Fuel Cell Powertrain |
| HS | Hermite-Simpson [collocation] |
| LGR | Legendre-Gauss-Radau [collocation] |
| MAHEPA | Modular Approach to Hybrid electric Propulsion Architecture |
| MEA | Membrane-Electrode Assembly |
| MP | Multiphase |
| MTOM | Maximum Take-Off Mass |
| NLP | Non-linear programming problem |
| OCP | Optimal control problem |
| OCV | Open-Circuit Voltage |
| OEM | Operational Empty Mass |
| PEMFC | Proton-Exchange Membrane Fuel Cell |
| PMSEM | Permanent Magnet Synchronous (AC) Electric Motor |
| RD | Relative deviation |
| RMSPE | Root-mean-square percentage error |
| RPM | Rounds Per Minute |
| SoC | State of charge |

| | |
|---|---|
| SP | Single Phase |
| SPS | Supplementary power source |

**Roman Symbols**

| | | |
|---|---|---|
| $\mathcal{U}_{CPS}$ | Dependent control variable for CPS | A – or – /min |
| $A_m$ | Electrolyte membrane area | $\mathrm{m}^2$ |
| $C$ | Battery discharge rate | A |
| $C_D$ | Drag coefficient | – |
| $C_L$ | Lift coefficient | – |
| $C_P$ | Power coefficient | – |
| $C_T$ | Thrust coefficient | – |
| $c_\gamma$ | Flight path angle cost scaling factor | – |
| $c_{cooling}$ | Cooling drag scaling factor | – |
| $C_{D_0}$ | Zero-lift drag coefficient | – |
| $C_{L_0}$ | Lift coefficient at zero angle of attack | – |
| $C_{rated}$ | Rated cell discharge rate | A |
| $D$ | Drag force | N |
| $d$ | Distance | m |
| $D_{prop}$ | Propeller diameter | m |
| $E_{act}$ | Actual effective cell capacity | W h |
| $E_{alt}$ | Fuel boundary cost function | – |
| $E_{rated}$ | Rated cell energy capacity | W h |
| $h$ | Altitude | m |
| $h_{lim_{FC}}$ | Maximum altitude without loss of fuel cell power | m |
| $i$ | Current density | $\mathrm{A\,m^{-2}}$ |
| $i_0$ | Exchange current density | $\mathrm{A\,m^{-2}}$ |
| $i_{lim}$ | Limit current density | $\mathrm{A\,m^{-2}}$ |
| $I_{O_2lim}$ | Maximum fuel cell current draw limited by air mass flow (insufficient oxygen) | A |
| $J$ | Advance ratio | – |
| $J_{fuel}$ | Fuel cost function | – |
| $J_{range}$ | Maximum range cost function | – |
| $J_{time}$ | Flight time cost function | – |
| $K$ | Lift-induced drag coefficient | – |

| | | |
|---|---|---|
| $K_i$ | Empirical coefficients $[i \in \mathbb{N}^+]$ | – |
| $L_\gamma$ | Flight path angle stage cost | – |
| $L_{alt}$ | Altitude stage Lagrange cost function | – |
| $l_{fus}$ | Fuselage length | m |
| $m$ | Mass | kg |
| $n_{cells}$ | Total number of cells in a series-parallel configuration | – |
| $n_{coax}$ | Number of coaxial motors | – |
| $n_{e_{an}}$ | Number of electrons involved in the anode reaction | mol |
| $n_{e_{cat}}$ | Number of electrons involved in the anode reaction | mol |
| $n_{parallel}$ | Number of cell series strings connected in parallel | – |
| $n_{series}$ | Number of cells connected in series | – |
| $p_{amb}$ | Ambient air pressure | Pa |
| $P_{aux}$ | Auxiliary electric power required | W |
| $P_{bat}$ | Battery power output | W |
| $P_{elec_{tot}}$ | Total electric power demand | W |
| $P_{EM}$ | Electric power supplied to the motor | W |
| $P_{engine}$ | Engine output power | W |
| $p_{H_2}$ | Partial pressure of hydrogen gas | atm |
| $p_{O_2}$ | Partial pressure of oxygen gas | atm |
| $P_{shaft}$ | Propeller / motor shaft power | W |
| $q$ | Dynamic pressure | Pa |
| $Q_{bl}$ | Blower volumetric flow rate | $\mathrm{m^3\,s^{-1}}$ |
| $Q_{rated}$ | Rated battery capacity | A h |
| $R_{cell}$ | Battery cell internal resistance | $\Omega$ |
| $R_m$ | Electrolyte membrane resistance | $\Omega$ |
| $S$ | Wing surface area | $\mathrm{m^2}$ |
| $T$ | Thrust force | N |
| $T_{oper}$ | Operating temperature | K |
| $V$ | Cell voltage or potential | V |
| $V_0$ | Ideal fuelcell voltage at $T_{ref} = 25\,°\mathrm{C}$ and $p_{ref} = 1\,\mathrm{atm}$ | V |
| $V_{act}$ | Activation over-potential | V |
| $V_{conc}$ | Concentration over-potential | V |

| | | |
|---|---|---|
| $v_{cr}$ | Cruise airspeed | $\mathrm{m\,s^{-1}}$ |
| $V_{FC}$ | Actual fuel cell potential | V |
| $v_{IAS}$ | Indicated airspeed | $\mathrm{m\,s^{-1}}$ |
| $v_{NE}$ | Never exceed airspeed | $\mathrm{m\,s^{-1}}$ |
| $V_{OC}$ | Open-circuit potential | V |
| $V_{ohm}$ | Ohmic over-potential | V |
| $V_{rated}$ | Rated cell voltage | V |
| $v_{TAS}$ | Indicated airspeed | $\mathrm{m\,s^{-1}}$ |
| $V_{thermoneutral}$ | Thermoneutral potential | V |
| $W$ | Weight | N |
| b | Wingspan | m |

### Greek Symbols

| | | |
|---|---|---|
| $\alpha$ | Charge transfer coefficient | – |
| $\eta$ | Efficiency | – |
| $\eta_{bat}$ | Battery discharge efficiency | – |
| $\eta_{FC_{elec}}$ | Electric efficiency of the fuel cell | – |
| $\eta_{FC_{fuel}}$ | Fuel efficiency of the fuel cell | – |
| $\gamma$ | Flight path angle | ° |
| $\Lambda_{air}$ | Air excess ratio | – |
| $\Lambda_{H_2}$ | Hydrogen fuel excess ratio | – |
| $\Omega_{EM}$ | Rotational velocity of the electric motor | $\mathrm{min^{-1}}$ |
| $\Omega_{ICE}$ | Rotational velocity of the internal combustion engine | $\mathrm{min^{-1}}$ |
| $\Omega_{prop}$ | Rotational velocity of the propeller | $\mathrm{min^{-1}}$ |
| $\rho$ | Ambient air density | $\mathrm{kg\,m^{-3}}$ |
| $\rho_{lim}$ | Limit ambient air density for maximum fuel cell current draw | $\mathrm{kg\,m^{-3}}$ |
| $\tau$ | Torque | $\mathrm{N\,m}$ |
| $\tau_{EM}$ | Electric motor torque | $\mathrm{N\,m}$ |
| $\varepsilon_{RD}$ | Relative deviation error | – |
| $\varepsilon_{RMSP}$ | Root mean squared percentage error | – |
| $v$ | Airspeed | $\mathrm{m\,s^{-1}}$ |

### Chemical Elements

| | | |
|---|---|---|
| $C$ | Carbon | |

| | |
|---|---|
| $Co$ | Cobalt |
| $CO_2$ | Carbon dioxide |
| $e^-$ | Electron |
| $H^+$ | Hydrogen cathion |
| $H_2$ | Hydrogen gas |
| $H_2O$ | Water |
| $Li$ | Lithium |
| $Li^+$ | Lithium ion |
| $NO_x$ | Nitrogen oxides |
| $O_2$ | Oxygen gas |

**Constants**

| | | |
|---|---|---|
| $\rho_0$ | Reference air density at sea level | $1.225\,\mathrm{kg\,m^{-3}}$ |
| $F$ | Faraday's constant | $96\,485.332\,\mathrm{C\,mol^{-1}}$ |
| $g_0$ | Gravitational acceleration | $9.806\,65\,\mathrm{m\,s^{-2}}$ |
| $M_{air}$ | Molar mass of air | $28.96\,\mathrm{g\,mol^{-1}}$ |
| $M_{H_2}$ | Molar mass of hydrogen | $2.016\,\mathrm{g\,mol^{-1}}$ |
| $p_{ref}$ | Reference pressure | $1\,\mathrm{atm}$ |
| $R$ | Universal gas constant | $8.3145\,\mathrm{J\,mol^{-1}\,K^{-1}}$ |
| $T_{ref}$ | Reference temperature | $298.15\,\mathrm{K}$ |
| $x_{O_2}$ | Molar fraction of oxygen in air | $0.21\,-$ |

This page is intentionally left blank.

# List of Figures

# List of Tables

This page is intentionally left blank.

# 1 Introduction

In the effort to move away from fossil fuels, more electric and hybrid aircraft are quickly becoming a reality, motivated by the European Commission's ambitious Flight Path 2050 goals to reduce $CO_2$ and $NO_x$ emissions by 75% and 90% respectively, and noise by at least 60% [1]. While the technology to conceive aircraft with novel electric power trains exists, there are still some major limitations. For now, truly zero-emissions flight is only really feasible for general aviation and short haul aircraft. Nevertheless, the limited energy density of batteries, or lower peak power output of proton-exchange membrane fuel cells, inhibits their practicality. Combining them in a hybrid powertrain, however, can mitigate their shortcomings. Furthermore, conventionally powered aircraft, are equipped with overpowered engines to achieve take-off requirements, while only needing around 50%-60% of that power for the cruise portion of the flight. Here too, switching to a hybrid powertrain architecture could allow for reduction of the engine size with more focus on cruise efficiency, while a secondary power source provides a boost for take-off or even offering the capability of pure electric flight for short segments.

This work will focus on modelling the aircraft built for project MAHEPA, an EU-funded venture to develop the aircraft and powertrain systems of the future for general aviation and regional transport aircraft. A knowledge-based aircraft and powertrain model is developed to identify the best flight procedures which attain the best performance. The model allows for easy swapping of powertrain components, to examine aircraft performance for different architecture concepts. The model is then used to set up an optimal control problem, which returns both the best control functions, and the optimal trajectory for a certain performance index.

## 1.1 Project Scope and Motivation

The *Modular Approach to Hybrid electric Propulsion Architecture* (MAHEPA) consortium is developing hybrid and zero-emissions aircraft using modular powertrain architectures, working towards the Flight Path 2050 emissions goals and the next step in electric aviation propulsion technology. The project has five main objectives [2]:

**Objective 1:** Advancing the fuel-driven serial hybrid electric powertrain.

**Objective 2:** Advancing the reliability of zero-emission serial hybrid electric powertrain.

**Objective 3:** Advancing new airborne qualified, lightweight, high-power density components.

**Objective 4:** Developing 'common building blocks' solutions.

**Objective 5:** Gathering, analysing, and comparing in-flight performance and emission data.

The Goal of this thesis is to develop a tool which supports the analysis part of these objectives, by combining aircraft modeling and trajectory optimization. This work aims to provide a basis for future work on design and performance analysis of future, zero-emissions aircraft and hybrid powertrain configurations. The tool is then used to perform a series of case studies to demonstrate its capabilities and, and at the same time, evaluate the performance of the aircraft under investigation.

Objective 1 and Objective 2 consider two different types of aircraft, namely hybrid electric and fuel cell hybrid, respectively. Therefore, two aircraft will be modeled: the zero-emissions, fuel cell powered DLR HY4, and the hybrid electric Pipistrel Panthera. Both aircraft are described further in Section 1.1.1 and Section 1.1.2. While the reliability aspect of Objective 2 will not be covered, reliability estimation modules can always be added in the future. What is offered is a tool which helps estimate performance of different powertrain configurations and components, per Objective 3, and identifies optimal control strategies which can guide the design process.

Data obtained through Objective 5 is used to increase the accuracy and validate the aircraft and component models. Moreover, Objective 4 implies system modularity. To adhere to this modular approach, the aircraft model will be created using an object-oriented, knowledge-based implementation. This will be elaborated on in Chapter 2.

### 1.1.1 The Fuel-Cell-Hybrid HY4

The HY4, seen in Figure 1.1, was developed by Pipistrel and the German Aerospace Center (DLR) as a manned, hydrogen-powered aircraft. It is currently the only manned, zero-emissions aircraft with a hybrid fuell cell powertrain (HFCP). The airframe consists of two Pipistrel Taurus gliders, connected side-by-side by a shared central wing section. On this center wing section a fairing pod is mounted containing the AC-synchronous electric motor, which drives a four-bladed, fixed pitch propeller, and four proton exchange membrane fuel cell stacks. The fuel cells can be seen in Figure 1.1b. Each of the two fuselages has two passenger/pilot seats place side-by-side. Both fuselages contain a lithium-ion battery pack, and hydrogen storage tank behind the seats [3, 4]. Properties of the aircraft are summarized in Appendix A.1, and sketch of the series hybrid fuel cell powertrain layout is shown in Figure 1.2.

(a) The HY4 in flight [5]

(b) Fuel cell stacks in the central pod [3]

Figure 1.1: The HY4 hybrid fuel cell aircraft

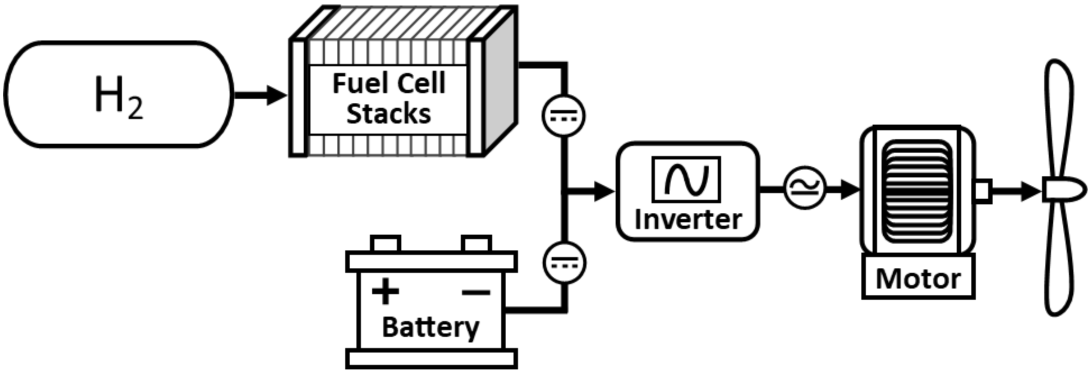

Figure 1.2: Sketch of the hybrid fuel cell powertrain used in the HY4

### 1.1.2 The Hybrid Electric Pipistrel Panthera

The Pipistrel Panthera, shown in Figure 1.3a, is a 4-seater general aviation aircraft designed to be fitted with three different powertrains: conventional, hybrid electric, and full electric. The conventionally powered version is undergoing type certification and is already available as a home-build kit. The version fitted with a series hybrid electric powertrain recently made its first test flight, and is the version which is considered in this work. The fully electric version is still under development.

The hybrid electric powertrain (HEP) consists of a 5-bladed, variable pitch propeller powered by two coaxial, AC-synchronous electric motors. Power is provided by battery packs and an internal combustion engine connected to an electric generator. Fuel tanks and batteries are located inside the wings. Figure 1.4 shows a sketch of the series hybrid electric powertrain, and more detailed properties of the Panthera and its powertrain components are given in Appendix A.2.

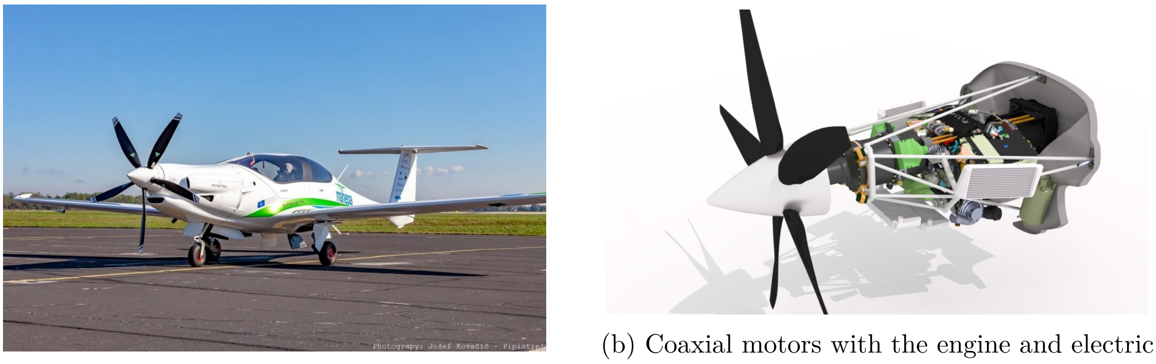

(a) The Panthera parked. [6]

(b) Coaxial motors with the engine and electric generator mounted behind. [6]

Figure 1.3: The hybrid electric Pipistrel Panthera.

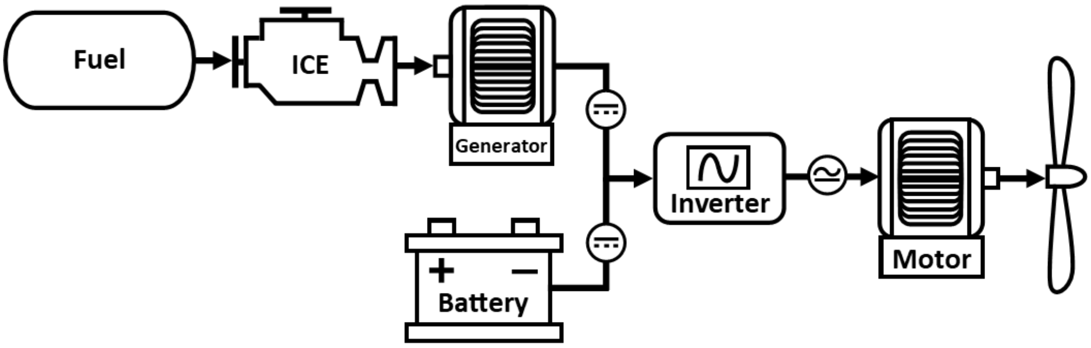

Figure 1.4: Sketch of the hybrid electric powertrain used in the Panthera

## 1.2 Research Objectives

Energy management becomes paramount when considering hybrid power trains. The propeller shaft is no longer directly connected to an engine, but to an electric motor, and electric power is delivered by multiple sources. This adds several degrees of freedom to the problem with an infinite number of possibilities for energy management. Moreover, the use of non-conventional power systems could introduce non-conventional behavior in the powertrain and flight performance. Where a combustion engine's fuel consumption and shaft power are practically linear with RPM setting, batteries and fuel cells show non-linear behaviour, as will be shown in Sections 3.2 and 3.3. In order to achieve the best possible performance and fuel efficiency with these novel architectures, it must be identified which power and energy source should be used at which points during the flight. In case of a hybrid aircraft with both batteries and fuel as energy source, be it hydrogen for a fuel cell or fossil fuel for a combustion engine, it would seem logical to first use up all the fuel, making the aircraft lighter, after which batteries can be used to power the now lighter aircraft. Whether this is truly the most optimal approach, especially for smaller aircraft, needs investigating.

While both the Panthera and the HY4 are modeled, the hybrid fuel cell powered HY4 is the main focus of this work, with the results for the Panthera serving as comparison, and thus the research questions are posed with this standpoint in mind. The research questions focussing on the optimal control of both aircraft are formulated in Research Question 1 and Research Sub-Questions 1.1 and 1.2. With the large emphasis on energy management, proper modeling of the unconventional on-board power sources is crucial. Therefore, special attention is given to the modeling and validation of the batteries and fuel cell models in Research Question 2. Finally, different solution methods for the optimal control problem are considered in Research Question 3.

**RQ-1.** What does the fuel-optimal flight path, and corresponding energy management, look like for a hybrid fuel cell aircraft?

  **RQ-1.1.** How does the minimum fuel flight trajectory and energy management of a hybrid fuel-cell aircraft differ from that of hybrid-electric aircraft?

  **RQ-1.2.** How does the fuel-optimal trajectory and energy management compare to trajectories which minimize flight time?

**RQ-2.** Can an existing numerical model based on a combination of mechanistic equations and empirical methods, also called semi-empirical methods, be used to adequately model performance of electrochemical cells for all conditions in the operating range of the aircraft?

**RQ-3.** Which optimal control transcription method is most suitable for fuel-optimal trajectory optimization for the hybrid aircraft model used?

# 2 Methodology

The process of answering the research questions can be split up in two major parts: modeling of the aircraft, and optimization of its flight performance and energy management through trajectory optimization. Each of these two parts can be further broken down in three steps, as presented in Figure 2.1. The aircraft modeling concepts are discussed in Section 2.1, with the actual models for the aircraft and powertrain detailed in Chapter 3. The final part of creating the aircraft model is the validation, performed in Chapter 5.

Similarly, the general approach to solving the performance and energy management optimization problem is explained in Section 2.2, with the actual optimization set-up provided in Chapter 4. Finally, the obtained solutions will be presented and discussed in Chapter 6.

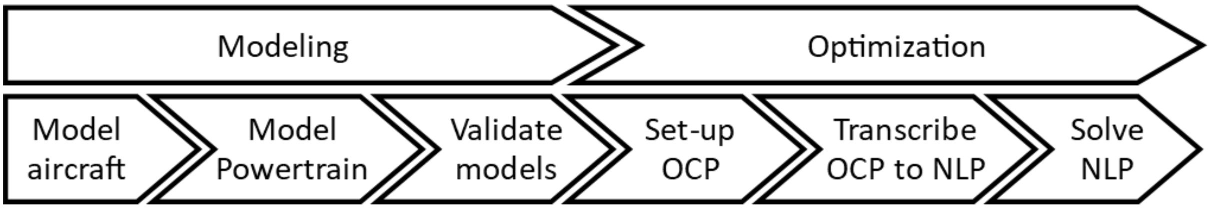

Figure 2.1: Visual representation of the process of answering the research questions

## 2.1 Modular Approach To Aircraft Modeling

The aircraft knowledge-based model is created using object-oriented programming in MATLAB. Using object-oriented programming allows for easy creation of new powertrain components in the future, as well as modularity in the buildup of the desired powertrain. The knowledge base consists of experimental data for each of the components. A basic example of a possible aircraft model class diagram is shown in Figure 2.2. Thanks to the object-oriented implementation, the powertrain components are not interlinked, meaning it is possible to add or swap out components as desired and explore configuration concepts. Linking components together is done in the powertrain object. Additionally, the aircraft (airframe) class also has no direct links with the powertrain, the powertrain is simply a part of it. This allows complete freedom in choosing which powertrain configuration an aircraft is fitted with.

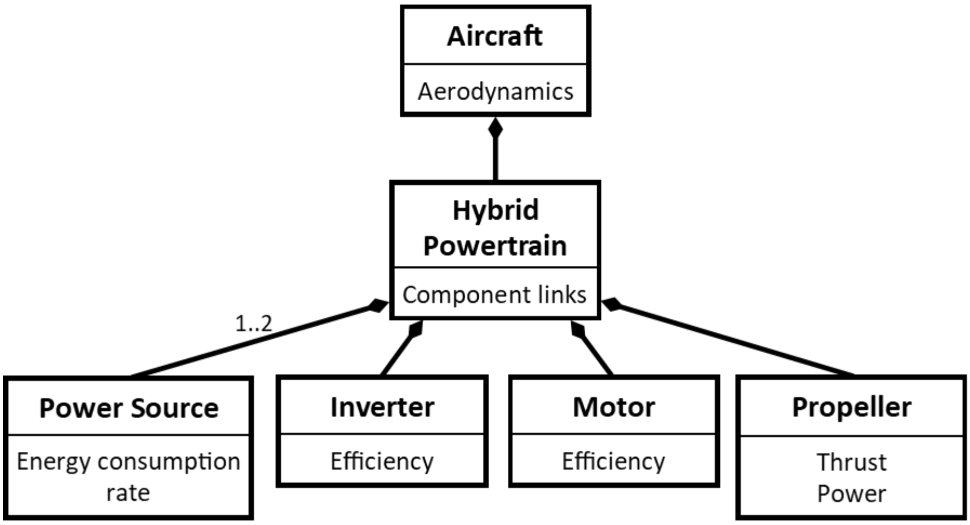

Figure 2.2: Simplified conceptual class diagram of the aircraft model

This modularity of the code is achieved by applying the SOLID principles for object-oriented programming [7], which also ensure the code is sustainable. The SOLID principles are the following:

**Single-Responsibility Principle:** Each piece of code (class, method, or function) should have only a single responsibility or purpose.

**Open-Closed Principle:** Each piece of code should be open for extension, but closed to modification, meaning existing code should not require modification when functionality is added.

**Liskov Substitution Principle:** If functions are redefined in subclasses, their behavior must remain the same to that of the function in the base class, e.g. same input and output types.

**Interface Segregation Principle:** Subclasses should not inherit methods they do not require. Therefore, methods should be separated from certain classes if required.

**Dependency inversion Principle:** Classes should not depend on specific subclasses, but on abstractions.

Specifically, the single-responsibility requirement, open-closed principle, and dependency inversion are considered throughout the creation of the knowledge-based model. The splitting up of tasks to achieve single-responsibility can be seen in the detailed class diagrams (Appendix C), and aids with obtaining required values when interfacing with the transcription and optimization tool. The buildup of the model using composition links, presented in Figure 2.2, is a good example of dependency inversion, where the aircraft and powertrain classes do not depend on one specific component class. For example, there is no single propeller class which can be part of the powertrain, it can be either a fixed-pitch or variable-pitch class instance, and the rest of the code depends on propellers, but not the specific propeller type. Applying Liskov's substitution principle results in the possibility of using different powertrain configurations, without the need to change functions which call the powertrain or its components, even though the components can be different. Interface segregation is used to separate the component models and parameter estimation functions which fit the model to experimental data, as will be discussed for the fuel cell and battery models in Sections 3.2 and 3.3. Thanks to the increased sustainability of the code when applying the SOLID principles, specifically the open-closed principle, which the remaining principles work towards in some way, the model and code can easily grow in the future.

## 2.2 Optimal Control And Transcription

Using control or trajectory optimization makes it possible to find the optimal flight path and energy management for certain performance indices. Specifically, the optimal state and control trajectories, $x^*(t)$ and $u^*(t)$, are determined for a minimum value of a certain cost function, $J(x,u)$.The cost function is defined in Equation 2.1, and consist of the Mayer term $E$ and Lagrange term $L$. These define the boundary cost and integral or stage cost respectively. The problem is subject to the system dynamics constraints $\boldsymbol{f}$, the inequality path constraints $\boldsymbol{g}_{path}$, and the boundary constraints $\boldsymbol{b}$, defined by Equations 2.2 to 2.4. The cost function has two distinct parts. The first term, $E$, is the Mayer term and returns the boundary cost. The integral part is the Lagrange cost, also referred to as the stage cost.[8]

$$\min J = E(\boldsymbol{x}(t_0), \boldsymbol{x}(t_f), \boldsymbol{u}(t_0), \boldsymbol{u}(t_f), t_0, t_f) + \int_{t_0}^{t_f} L(\boldsymbol{x}(t), \boldsymbol{u}(t))dt \tag{2.1}$$

$$\dot{\boldsymbol{x}}(t) = \boldsymbol{f}(\boldsymbol{x}(t), \boldsymbol{u}(t)) \tag{2.2}$$

$$\boldsymbol{g}_{path}(\boldsymbol{x}(t), \boldsymbol{u}(t)) \leq \boldsymbol{0} \tag{2.3}$$

$$\boldsymbol{b}(\boldsymbol{x}(t), \boldsymbol{u}(t), t_0, t_f) \leq \boldsymbol{0} \tag{2.4}$$

A generalized XDSM diagram describing the trajectory optimization is provided in Figure 2.3. The aircraft and powertrain models are used to determine the aircraft dynamics, which are applied as constraints when determining the optimal state and control functions. Path constraints are applied as required to avoid exceeding component limitations, and the objective is the cost as a function of the current iterates of the states and controls.

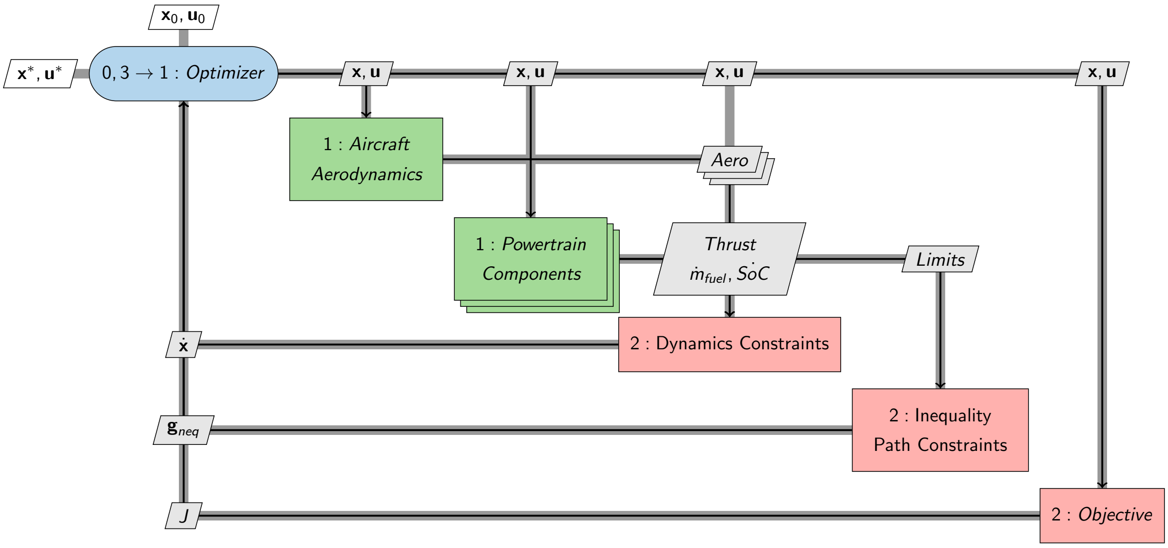

Figure 2.3: Conceptual design structure matrix diagram

To solve an optimal control problem, it must first be converted or transcribed from a time-continuous problem into a finite-dimensional non-linear programming problem (NLP). An NLP's cost function is defined by Equation 2.5, subject to inequality constraints and equality constraints, given by Equations 2.6 and 2.7 respectively. [9]

$$\min J = J(\boldsymbol{z}) \tag{2.5}$$

$$\boldsymbol{g}(\boldsymbol{z}) \leq \boldsymbol{0} \tag{2.6}$$

$$\boldsymbol{h}(\boldsymbol{z}) = \boldsymbol{0} \tag{2.7}$$

Both transcription and solving of the control problem is taken care of by ICLOCS [10], an open-source MATLAB optimal control tool, which uses IPOPT[11] to solve the transcribed problem. Two different direct collocation methods implemented by ICLOCS are considered: Hermite-Simpson (HS) direct collocation and Legendre-Gauss-Radau (LGR) orthogonal collocation. Both of these are explained further in Section 2.2.1 and Section 2.2.1 respectively. While there are other direct collocation methods available, each one defined by the interpolation and integral approximation techniques used [9, 12], these are not considered due to their lower accuracy, and thus HS collocation is assumed to be synonymous with direct collocation in the remainder of this paper [13].

### 2.2.1 Direct Collocation

Direct collocation is a transcription method, which transcribes the OCP to a NLP through discretization of the state, control, and objective functions, without the need to derive the optimality conditions of the Hamiltonian boundary-value problem (HBVP). A simple way to explain the difference between direct and indirect methods is that direct methods first discretize the problem, then optimize, while indirect methods first optimize and then discretize [8, 14]. Indirect methods will not be covered further.

Direct collocation methods are also simultaneous methods, which means both the state and control functions are varied simultaneously. To ensure the controls match the states solutions, the system dynamics are applied as derivative constraints, also called dynamics constraints or collocation constraints [13, 14]. In contrast, shooting methods are an example of non-simultanuous methods. They only discretize and vary the control functions, and approximate the states through simulation of the system dynamics. However, since shooting methods are less efficient, less accurate, and make imposing path constraints difficult, they appear inferior to collocation methods and will thus not be considered further [9, 15].

The derivative constraints can be applied in either the derivative form, or the integral form, depicted in Figure 2.4, and both will lead to the same expression for the constraint, confirmed in Appendix E. However, using the integral form of the dynamics constraint is more suited for shooting methods, while the direct collocation methods considered here use the derivative form [16].

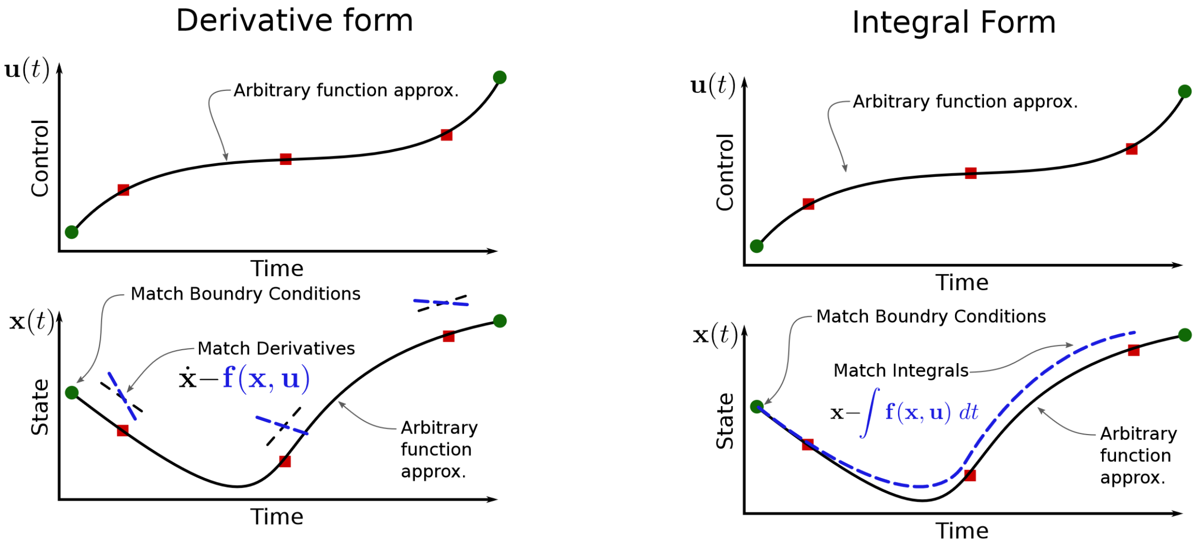

Figure 2.4: Graphical representation of the difference between the dynamics in derivative form (left), and the integral form (right).[8]

There are three parts which set different direct collocation methods apart. First, functions are discretized in time by three different types of points:

- *Nodes* are points used to interpolate the solution function, meaning the function approximation is exact in these points.
- *Knot points* are a subset of nodes marking the boundaries between segments, splitting the time domain in separate sub-intervals.
- *Collocation points* are points where the dynamics/derivative/collocation constraints, defined by Equation 2.2, are applied.

After the optimizer has changed the values at the nodes, they are interpolated to again obtain a time continuous function which approximates the solution. Integrals in the objective function and collocation constraints, if the integral form is used, are approximated using some form of quadrature. The name of the collocation algorithm refers to the techniques used for each of these three processes. Each of these points are explained further for HS and LGR collocation in Section 2.2.1 respectively. Figure 2.5 provides a schematic break-down of the methods to solve optimal control problems, and some (dis)advantages of each one. Hermite-Simpson falls under the local collocation methods, and the Radau form of Legendre-Gauss considered is a form of pseudo-spectral collocation.

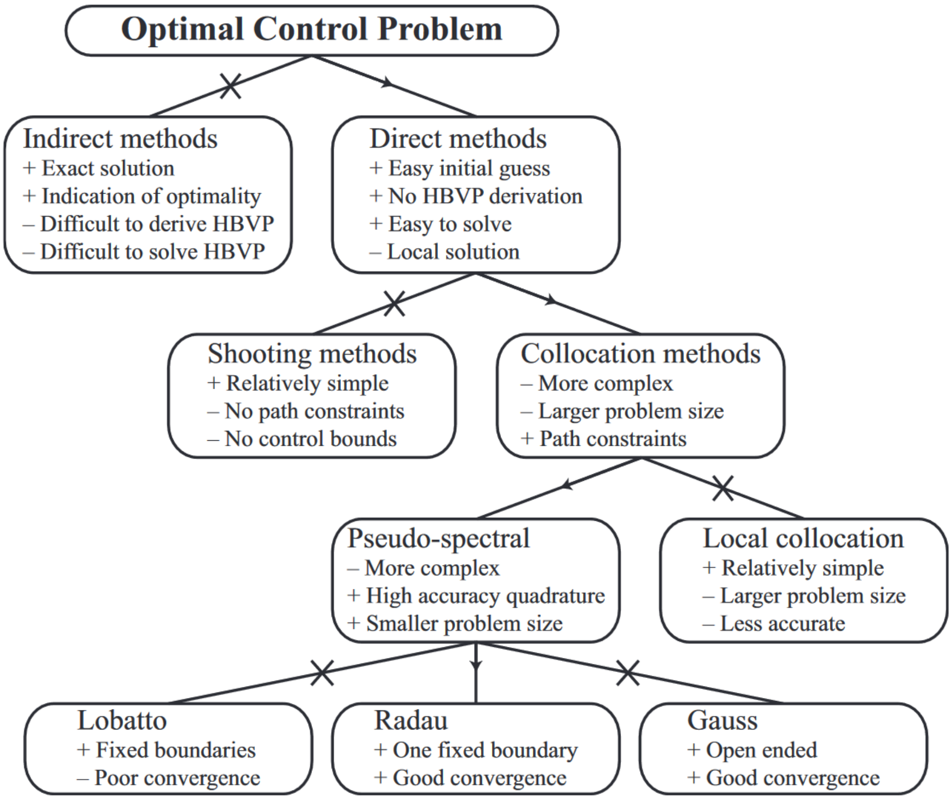

Figure 2.5: Breakdown of different transcription methods.[15]

### Hermite-Simpson Collocation

Hermite-Simpson collocation is a local collocation method (Figure 2.5) which uses the same discretization as simpler methods, like trapezoidal collocation, but uses higher order interpolation polynomials to obtain more accurate results.
First, all functions are discretized in the time domain, $[t_0 \; t_f]$, by equispaced knot points, which split the total time interval into equal-length segments. With HS collocation, the knot points are the only nodes used. Finally, collocation points are added in the midpoints of the segments, where the derivative constraints are imposed.

Using the state and state derivative values in the nodes, a cubic Hermite spline is constructed to interpolate the state functions for each segment. Taking the derivative of this spline yields a piece-wise quadratic spline which approximates the dynamics. For the control functions simple linear interpolation is used [13, 16]. Discretization and interpolation are visualized in Figure 2.6. Finally, integrals are approximated using Simpson's quadrature rule, given in Equation E.9. The interpolation and integral approximation process is given in more detail in Appendix E.1

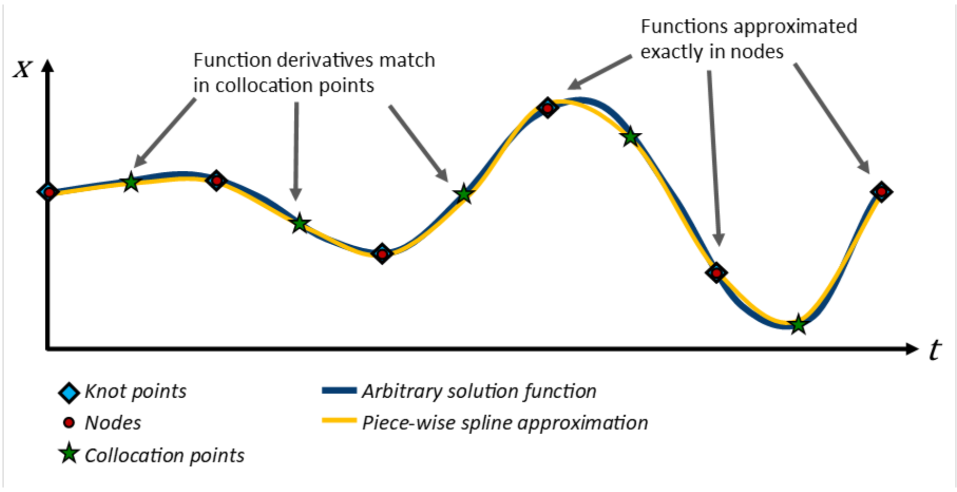

Figure 2.6: Approximation of a state function by a piece-wise spline, with collocation points placed in the segment midpoints.[9]

### Orthogonal and Pseudo-Spectral Collocation

Orthogonal collocation is a special kind of direct collocation. Similar to HS direct collocation, the functions are first split into one or more segments by knot points. When multiple segments are used, the method is called local orthogonal, and it applies higher accuracy quadrature to a local method. Contrarily, if only a single segment is used which spans the entire time domain, the method is called global orthogonal, or pseudo-spectral collocation [9]. Only global orthogonal collocation will be considered, as it is proven to be more computationally efficient and produces more accurate results for smooth problems than local orthogonal collocation (see Figure 2.5) [17].

With orthogonal collocation, nodes and collocation points coincide, and are Gauss-type quadrature points. Their location is determined by the roots of an orthogonal polynomial, and focussed more towards the knot points of the segment. Figure 2.7 shows a comparison between HS collocation and global orthogonal or pseudo-spectral collocation. Which orthogonal polynomial exactly defines the node locations depends again on the type of collocation method used.

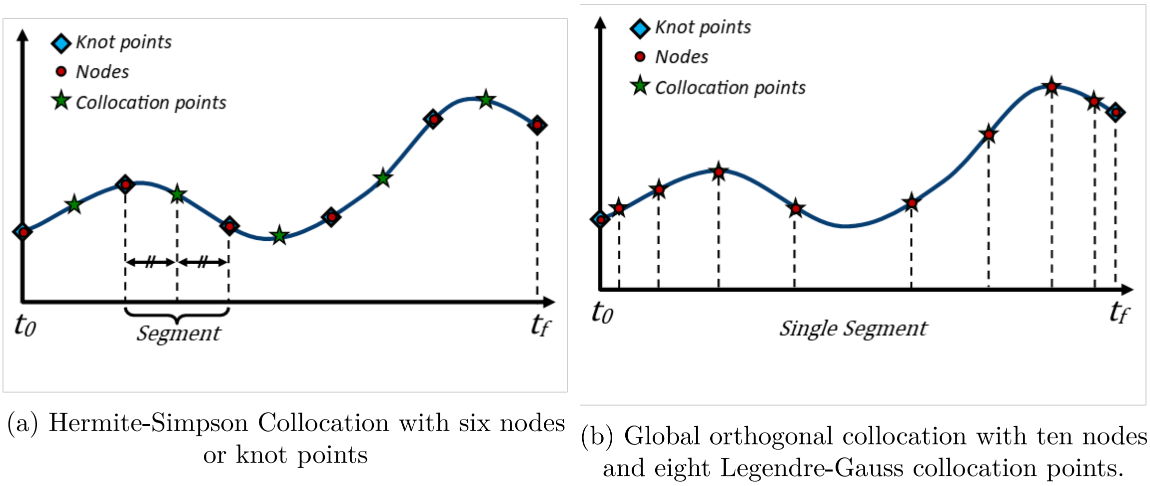

(a) Hermite-Simpson Collocation with six nodes or knot points

(b) Global orthogonal collocation with ten nodes and eight Legendre-Gauss collocation points.

Figure 2.7: Visual comparison between direct and orthogonal collocation on an arbitrary function. [8, 13]

The three orthogonal collocation methods discussed most in literature are Legendre-Gauss (LG), Legendre-Gauss-Radau (LGR), and Legendre-Gauss-Lobatto (LGL) collocation. As suggested by the names, all of these methods use Legendre polynomials to determine the discretization of the functions. Figure 2.8 shows that LG collocation includes neither of the end-points, while LGL includes both. In case of Legendre-Gauss-Radau (LGR) collocation, only the first knot point of each segment is considered. Note that the knot points are always nodes, regardless of whether they are collocated. Radau collocation offers better accuracy than standard LG, and allows the first point to be fixed, and seems the most suitable for the problem at hand. LGR collocaiton is chosed over LGL collocation, as the latter potentially impedes convergence by constraining the dynamics in the final point (see Figure 2.5)[15]. Henceforth, PS collocation will be considered synonymous with LGR collocation specifically.

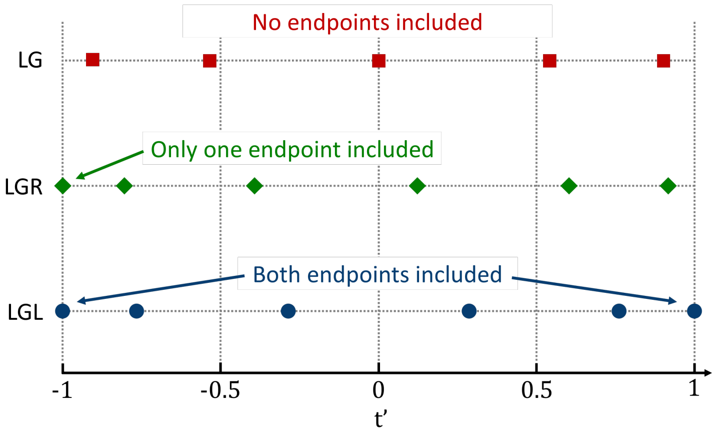

Figure 2.8: Comparison between the location of the collocation points for LG, LGR, and LGL collocation.[18]

After transforming the time domain from $[t_0,\ t_f]$ to $[t'_0,\ t'_f] = [-1,\ 1]$, $n$ LGR collocation points are placed in the roots obtained from $\mathcal{P}_{n-1}(t') + \mathcal{P}_n(t')$, where $\mathcal{P}_n$ is the $n$-th degree Legendre polynomial. This is equivalent to placing $n-1$ collocation points in the roots of the $n$-th degree Legendre polynomial, $\mathcal{P}_n$, and simply adding one extra collocation point in the first knot points, at $t' = -1$. [13, 18]

The final knot point is not collocated, but is used as a node to construct the function interpolant. Therefore, the states and control functions are approximated using $n+1$ points to construct a global Lagrange interpolating polynomial of degree at most $n$. The derivative of the state interpolants will yield an expression which approximated the dynamics functions, used to impose the derivative constraints in the collocation points. Finally, integrals are approximated using the Radau form of Legendre-Gaussian quadrature. [13, 14, 16, 18]

The main advantage of using orthogonal collocation over direct collocation methods like HS, is that spectral convergence can be achieved, meaning the error convergence rate increases exponentially with increasing number of nodes [13]. This resulted in optimal solution being found faster than when HS collocation was used, but only for simpler problems (see Chapter 6). Additionally, the optimization results obtained using orthogonal collocation methods were less sensitive to initial guesses. Therefore, all single phase solutions considered are obtained using the LGR transcription algorithm. More mathematical background on Radau orthogonal collocation is given in Appendix E.2.

### 2.2.2 Multiphase Problems

Defining the problem in a multiphase format allows for more realistic flight profiles. For example, the gradual climb seen in the single phase solutions might not be possible in reality due to obstacle clearance issues. Likewise, a continuously changing cruise altitude requires constant input from the (auto)pilots, not to mention the air traffic controllers will probably prefer a more constant altitude. Additionally, having dedicated climb and descent phases can be used to prevent the issue for the minimum fuel case, where the solution would keep an aircraft at zero altitude instead of climbing. This behavior was observed for the case of the HY4, and will be discussed further in Section 6.2.1.

The multiphase problem is similar to a multisegment problem. First, the time domain is split into phases. Each phase is its own individual problem. This means each phase can have different variable bounds, error tolerances, dynamics equations, cost functions, and even transcription methods. The phases are linked together by the phase boundary link constraints, which ensure that the states, inputs, and time in the first point of a phase equal those in the last point of the previous phase. These boundary link constraints are given by Equations 2.8 to 2.10, where $p$ indicates the phase number and $n_{phases}$ is the total number of phases used. Phases and phase links are visualized in Figure 2.9.

$$x_p(t_f) - x_{p+1}(t_0) = 0 \ , \qquad p \in [1, ..., n_{phases} - 1] \tag{2.8}$$

$$u_p(t_f) - u_{p+1}(t_0) = 0 \ , \qquad p \in [1, ..., n_{phases} - 1] \tag{2.9}$$

$$t_{f_p} - t_{0_{p+1}} = 0 \ , \qquad p \in [1, ..., n_{phases} - 1] \tag{2.10}$$

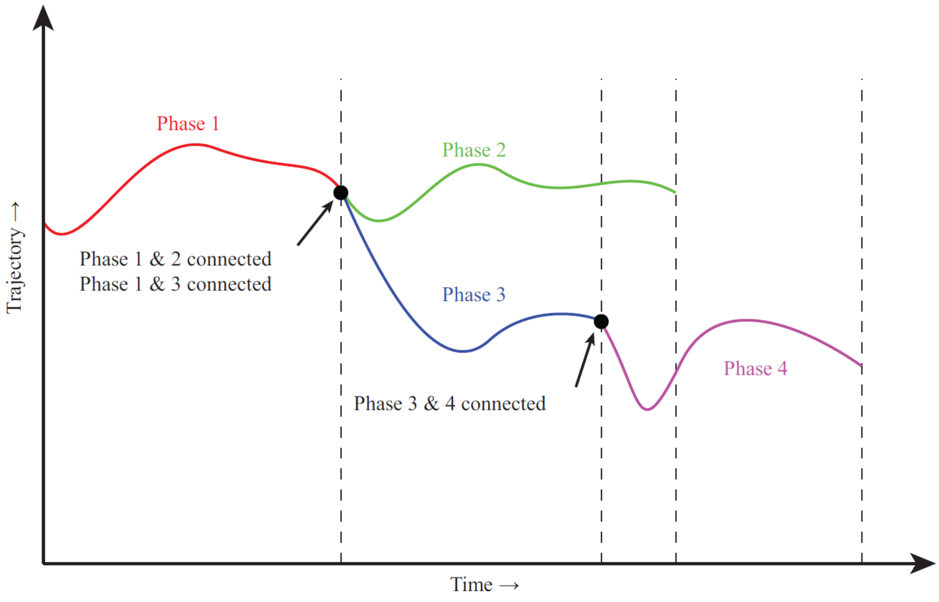

Figure 2.9: Visualization of a multiphase problem with phase links.[15]

For the multiphase problem setup, five phases are considered:

**Phase 1:** an initial obstacle climb to 150 m in minimum distance.

**Phase 2:** a free climb to an altitude of at least 300 m with a climb rate of at least 0.1 m s$^{-1}$.

**Phase 3:** a constant altitude cruise.

**Phase 4:** a free descent to an altitude of 30 m with a descent rate of 0.1 m s$^{-1}$ or more. In the final boundary point, the airspeed must equal the reference airspeed $v = 1.3 v_s$ [19].

**Phase 5:** a final approach which requires the airspeed to equal the stall speed and a vertical airspeed between $-0.3\,\mathrm{m\,s^{-1}}$ and $-0.9\,\mathrm{m\,s^{-1}}$ to ensure a smooth yet firm touchdown.

With these phases, a more realistic flight profile is replicated. The minimum values for climb and descent rates are put in place to avoid plateaus in the altitude profile when the optimizer gets caught in a local minimum, or is reluctant to climb (see Section 6.2).

Since the multiphase problem is a more constrained subproblem of the single phase problem, also the solution will be a suboptimal one compared to what is obtained from a single phase setup. Moreover, since multisegment methods (local methods) are computationally less efficient, so is the multiphase problem. Unfortunately, no solutions could be obtained for the multiphase problem when using LGR collocation. Instead, the solutions reported in Chapter 6 for the multiphase problems are obtained using HS collocation.

This page is intentionally left blank.

# 3 Knowledge-Based Aircraft Model

As discussed in Section 2.1, the complete aircraft model consists of the aircraft airframe model, the powertrain components, and the links between the components. The complete model class diagram is shown Appendix C. The aircraft (airframe) model is first discussed in Section 3.1. The different components which require modeling can be identified by looking at the powertrain diagrams in Figures 1.2 and 1.4. The models for all these components are given in Sections 3.2 to 3.6. The powertrain model itself, which links the components together, is covered in Section 3.7. The fuel cells and batteries, covered in Sections 3.2 and 3.3, are modeled explicitly, while all other components' performance is determined by interpolating performance look-up tables containing test data.

## 3.1 Aircraft Model

The aircraft model mostly consists of the aerodynamics equations. Assuming a simple point-mass model, the aircraft's two-dimensional equations of motion are given by the horizontal speed or ground speed, Equation 3.1, the vertical speed, Equation 3.2, and the acceleration, Equation 3.3. The lift of the aircraft is assumed to equal the weight times the cosine of the flight path angle, according to Equation 3.4. Appendix D elaborates on the assumptions made to obtain this expression.

$$\dot{d} = v\cos\gamma \tag{3.1}$$

$$\dot{h} = v\sin\gamma \tag{3.2}$$

$$\dot{v} = \frac{T-D}{m} - g_0 \cdot \sin\gamma \tag{3.3}$$

The lift coefficient, $C_L$, is then found using Equation 3.5, where $q$ is the dynamic pressure. The drag coefficient is determined slightly differently for the HY4 and the Panthera. For the latter, the drag coefficient is found using the classic quadratic drag function, given in Equation 3.6, where the lift-induced drag factor, $K$, is determined experimentally. The HY4 drag coefficient uses the adjusted drag model [19], augmented with an extra term accounting for the additional drag generated by the fuel cell cooling radiators. The adjusted drag coefficient equation can be seen in Equation 3.7 [4].

$$L = W\cos\gamma \tag{3.4}$$

$$C_L = \frac{W\sin\gamma}{qS} \tag{3.5}$$

$$C_D = C_{D_0} + KC_L^2 \tag{3.6}$$

$$C_{D_{HY4}} = C_{D_0} + K\left(C_L - C_{L_0}\right)^2 + c_{cooling}C_{D_{cooling}} \tag{3.7}$$

## 3.2 Proton-Exchange Membrane Fuel Cell

A fuel cell is an electrochemical device which converts chemical energy into electrical energy. The electrochemical process resembles that of a battery, but where a battery is a closed, self-contained cell, fuel cells require a constant supply of fuel, just like combustion engines. Unlike combustion engines, however, there is no combustion, meaning lower energy losses in the form of heat resulting in a more efficient power generation process [20, 21].

The proton-exchange membrane fuel cell (PEMFC), also called the solid polymer fuel cell, is the most common fuel cell type used in electric vehicles [3, 20, 22, 23]. A solid-polymer ion-exchange-membrane serves as the electrolyte. A single cell consists of a membrane-electrode assembly (MEA), shown in Figure 3.1, and is no more than a couple of microns thick. Several MEAs are stacked together, separated by gas channels which supply the fuel to each cell, to increase the terminal voltage. Both electrodes are porous to increase the surface area and coated in a catalyst layer to increase the reaction rate. To ensure hydrogen protons are able to pass through to electrolyte, the membrane must contain free hydrogen ions ($H^+$) and is therefore kept hydrated.

The balance of plant (BOP) consists of all auxiliary components of the fuel cell system. This includes thermal and water management systems, potential fuel preparation such as filtering and/or humidifying, compressors or blowers, and power conditioning to stabilize output voltage. The BOP is not modeled for the current problem. Instead, a constant auxiliary power requirement of $P_{aux} = 1\,\text{kW}$ is added per fuel cell to account for the blower, thermal and water management systems [4].

### 3.2.1 The Electrochemical Process

For a PEM fuel cell, the electrochemical process which generates electric current is the reverse electrolysis of water, Equation 3.10. Electrolysis of water can be used to split water in hydrogen and oxygen gas by applying a current. This process is reversible by replacing the applied potential difference with an electric load. Hydrogen ($H_2$) and oxygen ($O_2$) will react to form water as well as generate a current flow through electrodes.

At the anode of the fuel cell, or the negative electrode, the reaction is given by Equation 3.8. Hydrogen gas will undergo oxidation and give off electrons ($e^-$), which the anode carries away. The remaining $H^+$ ions will move through the electrolyte to the cathode. At the cathode, or positive electrode, reduction takes place as oxygen gas reacts with the electrons from the cathode and the hydrogen ions in the electrolyte to form water molecules, according to Equation 3.9. Combining the half-reactions from Equations 3.8 and 3.9 yields the simplified reaction shown in Equation 3.10. The process is visualized in Figure 3.1.

$$H_2 \rightarrow 2H^+ + 2e^- \tag{3.8}$$

$$O_2 + 4e^- + 4H^+ \rightarrow 2H_2O \tag{3.9}$$

$$2H_2 + O_2 \rightarrow 2H_2O \tag{3.10}$$

Equation 3.10 may be interpreted as hydrogen being ‘burnt’, yet instead of combustion and heat energy being released, an electric current is generated [24]. Therefore, the energy losses due to heat are much lower.

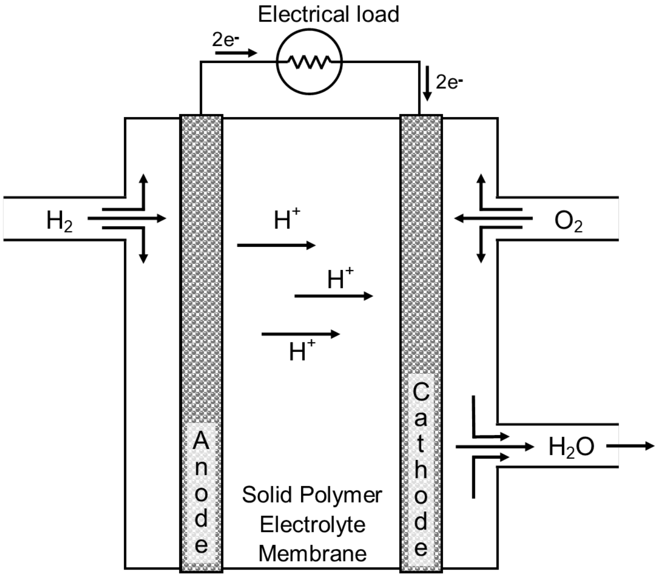

Figure 3.1: Simplified representation of a single membrane-electrode assembly

### 3.2.2 Performance Model

To estimate the performance of the fuel cell, a semi-empirical, static model is used to construct the polarization curve, an example of which is shown in Figure 3.2. Semi-empirical models combine analytical equations with parameter estimation to determine the unknowns. The polarization curve is then used to find the cell terminal voltage for a given current density, $i = \frac{I}{A_m}$, which is the current per unit area of the electrolyte membrane. Since the cells in a stack are connected in series, the current (density) is equal for each cell.

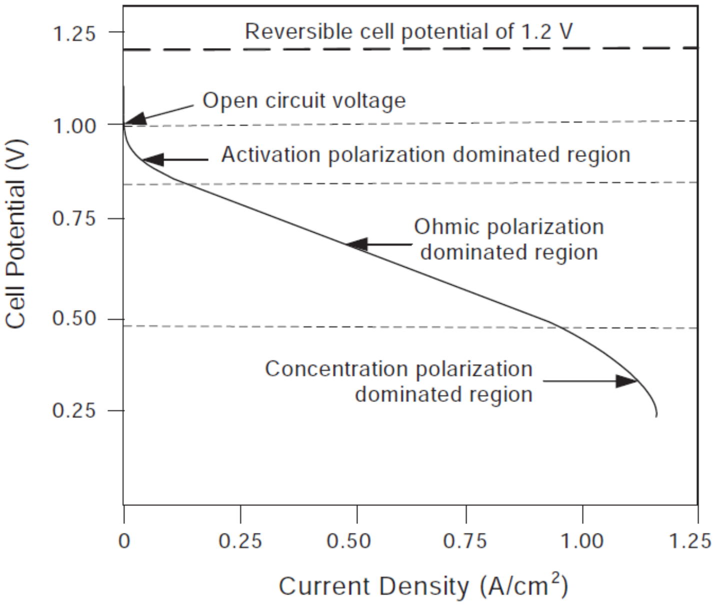

Figure 3.2: Example of a fuel cell polarization curve showing different losses [25]

For a given current draw, the cell voltage is found by first determining the open-circuit voltage, $V_{OC}$, which is the voltage when no current flows, and subtracting the activation ($V_{act}$), ohmic ($V_{ohm}$), and concentration ($V_{conc}$) voltage losses or overpotentials (Equation 3.11).

$$V_{FC} = V_{OC} - V_{act} - V_{conc} - V_{ohm} \tag{3.11}$$

The ideal cell voltage is known to be $V_0 = 1.229\,\mathrm{V}$ for a temperature of $T_{ref} = 25\,°\mathrm{C} = 298.15\,\mathrm{K}$ and gas pressure of $p_{ref} = 1\,\mathrm{atm}$. The open-circuit voltage is determined using Nernst equation to correct the ideal voltage for non-standard temperature and pressure. The Nernst equation is shown in Equation 3.12, where $R$ is the universal gas constant, $F$ is Faraday's constant, $n_{ean} = 2$ is the number of electrons involved in the anode reaction (Equation 3.8), and $p_{H_2}$ and $p_{O_2}$ are the partial pressures of hydrogen and oxygen gas in atmosphere respectively [25, 26, 27, 28, 29, 30, 31].

$$V_{OC} = V_0 - 0.85 \times 10^{-3}(T_{oper} - 298.15) + \frac{RT_{oper}}{n_{ean}F} \ln\left(p_{H_2}\sqrt{p_{O_2}}\right) \tag{3.12}$$

A minimum potential difference between the electrodes is required to overcome the energy barrier and keep the reaction going and the electrons and protons moving. This non-useful potential difference is called the Activation over-potential and is the dominant loss at low current densities, varying logarithmically with current density. The activation over-potential is found using the Buttler-Volmer equation, Equation 3.13, where $\alpha$ is the charge transfer coefficient, $i_0$ is the exchange current density, and $n_e$ is the amount of electrons involved in the reaction. From Equations 3.8 and 3.9 this is known to be 2 and 4 for the anode and cathode respectively. The exchange current density is the current density where no useful current can be drawn from the cell. It is an equilibrium state where the reaction from Equation 3.10 proceeds in both directions. Protons move in both directions between the anode and cathode and reactant gasses repeatedly give off and take on electrons from the electrodes [26, 27, 32].

$$V_{act} = \frac{RT_{oper}}{n_e\alpha F} \ln \frac{i}{i_0}\bigg|_{anode} + \frac{RT_{oper}}{n_e\alpha F} \ln \frac{i}{i_0}\bigg|_{cathode} \tag{3.13}$$

Ohmic voltage losses are caused by resistance of the electrolyte membrane to the flow of ions. The ohmic overpotential is found using Ohm's law, Equation 3.14, if the resistance value of the electrolyte is known. The membrane resistance is a function of membrane hydration and temperature, but is simplified here to a constant value $R_m$ [26].

$$V_{ohm} = iR_m \tag{3.14}$$

Concentration losses occur due to reduced availability of the reactants at the electrodes as they are used up. Additionally, at high current densities, the large amount of water produced will cause the electrodes to flood, preventing more reactants to reach them. Because of this, the concentration losses are most prominent at high current density values. The concentration over-potential is estimated using Equation 3.15, where $i_{max}$ is the maximum current density. This equation will result in a very sudden drop-off in voltage near the maximum current value. A simplified empirical relation could be used to obtain a more realistic, gradual decrease if required [26], however, the current values for which concentration losses become significant fall outside the normal operating range of the fuel cell. It is therefore possible to leave the concentration losses out of the model entirely without significant influence on the performance results as long as current values remain in the predefined range [32].

$$V_{conc} = \frac{RT_{oper}}{n_e F} \ln \frac{i_{lim}}{i_{lim} - i}\bigg|_{anode} + \frac{RT_{oper}}{n_e F} \ln \frac{i_{lim}}{i_{lim} - i}\bigg|_{cathode} \tag{3.15}$$

The stack power can now be determined using Equation 3.16, where $A_m$ is the area of the cell's electrolyte membrane, and $n_{cells}$ is the amount of MEAs or cells stacked together. The electrical efficiency of the fuel cell equals the ratio of the actual cell voltage and the ideal cell voltage $V_0 = 1.229\,\mathrm{V}$ (Equation 3.17). To find the total fuel efficiency, shown in Equation 3.18, the cell voltage must be compared to the thermoneutral voltage $V_{thermoneutral} = 1.482\,\mathrm{V}$, which accounts for both the electrical and the thermal potential of the fuel. Taking the ratio of the ideal cell voltage and the thermoneutral voltage yields the theoretical maximum fuel efficiency of a fuel cell $\eta_{FC_{fuelmax}} = \frac{1.229}{1.482} = 83\%$.

$$P_{FCS} = V_{FC} \cdot i \cdot A \cdot n_{cells} \tag{3.16}$$

$$\eta_{FC_{elec}} = \frac{V_{FC}}{1.229} \tag{3.17}$$

$$\eta_{FC_{fuel}} = \frac{V_{FC}}{1.482} \tag{3.18}$$

Finally, the mass flow rate of the reactant gasses is determined using Equations 3.19 and 3.20, by determining the molar flow rate based on the number of electrons involved in the reactions. $n_{e_{an}} = 2$ for the anode and $n_{e_{cat}} = 4$ for the cathode, according to Equations 3.8 and 3.9, and $M_{H_2} = 2.016\,\mathrm{g\,mol^{-1}}$ and $M_{air} = 28.96\,\mathrm{g\,mol^{-1}}$ are the molar masses of hydrogen and air, respectively. The air mass flow rate is corrected for ambient air density and the fact that the molar fraction of oxygen in air is only $x_{O_2} = 0.21$.

An excess ratio $\Lambda_{H_2} = 1.05$, or stoichiometric ratio, is added on the anode side to account for losses due to leakage, fuel cross-over, or use of a purge valve. Fuel crossover occurs when hydrogen gas molecules seep into the electrolyte membrane without giving off electrons to the anode. If no electrons are given off, they do not add to the current output. A purge valve can be installed on the gas channels to quickly refresh the reactant gasses. On the cathode side, oxygen, and thus air, should be supplied with excess ratio of at least $\Lambda_{air} = 1.3$ [26]. A more conservative value of $\Lambda_{air} = 1.7$ is used for the HY4 model[4]. This accounts not only for part of the oxygen not being used in the reaction, but also makes sure there is adequate air flow to carry away the product water [26].

$$\dot{m_{H_2}} = \Lambda_{H_2} M_{H_2} \frac{I}{F n_{e_{an}}} n_{cells} \tag{3.19}$$

$$\dot{m_{air}} = \Lambda_{air} \frac{\rho_0}{\rho} \frac{M_{air}}{x_{O_2}} \frac{I}{F n_{e_{cat}}} n_{cells} \tag{3.20}$$

Most fuel cells are either equipped with a compressor, or a blower, as is the case for the HY4 [4]. Blowers differ from compressors in that they focus solely on volumetric flow, rather than pressure. Therefore, the pressure increase due to the blower is negligible. If the maximum volumetric flow rate of the blower, $Q_{bl}$, is known, Equation 3.20 can be rewritten as shown in Equation 3.21, by substituting $\dot{m_{air}} = \rho Q_{bl}$, to determine the maximum achievable current for a given air density. If this value is lower than the maximum rated current of the fuel cell, power output is limited due to a lack of oxygen supplied.

$$I_{O_2 lim} = \frac{\rho^2}{\rho_0} \frac{Q_{bl}}{\Lambda_{air}} \frac{x_{O_2}}{M_{air}} \frac{F n_{e_{cat}}}{n_{cells}} \tag{3.21}$$

$$\rho_{lim} = \sqrt{\frac{\rho_0}{Q_{bl}} \frac{M_{air}}{x_{O_2}} \frac{I_{max}}{F n_{e_{cat}}} n_{cells}} \tag{3.22}$$

Equation 3.21 can in turn be rewritten to obtain Equation 3.22. This allows the limit value of the ambient air density, $\rho_{lim}$, to be determined, which in turn is used to solve for the maximum altitude the aircraft can reach without performance loss in the fuel cells due to a lack of oxygen.

Each fuel cell system in the HY4 powertrain is equipped with a blower capable of supplying $Q_{bl} = 1500\,\mathrm{L\,min^{-1}} = 0.025\,\mathrm{m^3\,s^{-1}}$ of air [4]. If the maximum rated current output of the fuel cells is $I_{max} = 195\,\mathrm{A}$, the air density limit found using Equation 3.22 corresponds to an altitude of $h_{lim_{FC}} = 5000\,\mathrm{m}$. At altitudes above $h_{lim_{FC}}$, the maximum achievable output current is constraint by Equation 3.21.

### 3.2.3 Parameter Estimation

The exchange current densities, charge transfer coefficients, membrane resistance, and membrane surface area are all unknown. These parameters are determined using parameter estimation, using available flight test data of the HY4. The recorded current draw from the test flight is used to determine the single cell voltage using Equation 3.11. An optimizer then minimizes the root-mean-square percentage error (RMSPE) of the calculated single-cell voltage with respect to the voltages recorded during the test flight, divided by the number of cells in the stack. This way, parameters are determined on a per cell basis, allowing for scalability of the stack in the model. For the initial conditions, the properties of the Ballard MkIV fuel cell are used [32]. The RMSPE, $\varepsilon_{RMSP}$, is defined by Equation 3.23, where $x_{i_{calc}}$ is the calculated value of a certain parameter, in this case cell voltage $V_{FC}$, $x_{i_{ref}}$ is the reference value, $i$ is the specific data point, and $n$ is the total amount of data points. If RMSPE is not specified, the error given is the relative deviation obtained using Equation 3.24, which returns a decimal value, whereas the RMSPE is a percentage.

$$\varepsilon_{RMSP} = \sqrt{\frac{\sum_{i=1}^{n}\left(\frac{x_{i_{calc}}}{x_{i_{ref}}} - 1\right)^2}{n}} \times 100 \tag{3.23}$$

$$\varepsilon_{RD} = \sqrt{\left(\frac{x_{i_{calc}}}{x_{i_{ref}}} - 1\right)^2} \tag{3.24}$$

The results of the parameter estimation are given in Table B.1. The resulting polarization curve is plotted in Figure 3.3, together with the data points used, and a polarization curve obtained from an early test-bench run. The choice was made to use the flight test data for the parameter estimation, rather than the test bench data, as the model better represents the actual fuel cell performance in the aircraft this way. The RMSPE of the model, compared to the test data, turns out to be $\varepsilon_{RMSPE} = 0.65\%$.

Since there are no data points available for the operating range where concentration losses become significant, the value of the limit current density has little to no effect on the parameter estimation and is thus not estimated properly. Therefore, the limit current density is set to be slightly higher than the maximum fuel cell current density, according to Equation 3.25, and $\Delta I$ is chosen as the smallest value which does not alter the results of the parameter estimation, while ensuring the exponential concentration losses begin immediately after the maximum current value is exceeded. The maximum current achieved on the test bench is $I_{max} = 195\,\mathrm{A}$, as seen in Figure 3.3. While the fuel cell stacks installed in the aircraft can be seen to perform worse than the bench tests, the maximum current value is assumed to be maintained. The lowest value for $\Delta I$ which does not influence the results of the parameter estimation is found to be $\Delta I = 35\,\mathrm{A}$. The resulting polarization and power curve for one of the fuel cell stacks is shown in Figure 3.4.

$$i_{lim} = \frac{I_{max} + \Delta I}{A_m} \tag{3.25}$$

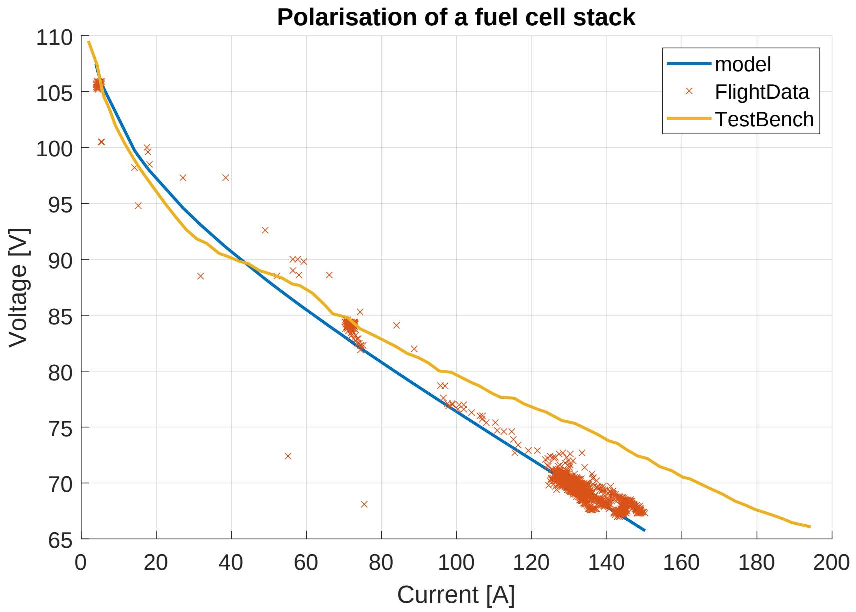

Figure 3.3: Stack polarization data comparison

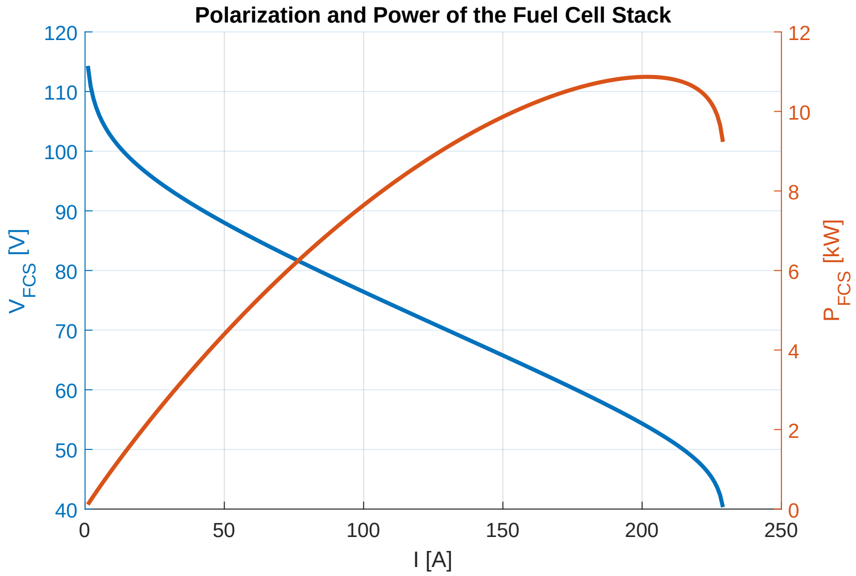

Figure 3.4: Polarization and power curve of one of the fuel cell stacks with $p_{cath} = 1\text{ATM}$.

### 3.2.4 Summary of Assumptions

The fuel cell model is subject to the following assumptions:

$\mathbf{p_{H_2O} = 0}$

All water produced by the reaction (Equation 3.10) is assumed to be in liquid state, which allows the partial pressure of water vapor to be left out of the Nernst equation.

$\mathbf{x_{H_2} = 1}$

The molar fraction of hydrogen in the fuel is one, meaning the fuel cell is supplied with pure hydrogen. Therefore, the partial pressure of hydrogen equals the total pressure at the anode.

$\mathbf{p_{H_2} = 0.2 \cdot p_{tank}}$

The pressure of hydrogen gas at the anode is assumed to be regulated by a pressure valve and equal one fifth of the pressure in the hydrogen storage tank, which in turn is assumed to vary linearly as a function of the amount of fuel remaining. This translates to an anode pressure varying between approximately 1 and 1.6 ATM in case of the HY4.

**$\mathbf{p_{O_2} = 0.21 \cdot p_{amb}}$**

Partial pressure of oxygen at the cathode is 21% of the ambient air pressure. This implies the molar fraction of oxygen in air is a constant $x_{O_2} = 0.21$ regardless of altitude or density.

**$\mathbf{T_{oper} = 70°C = 343K}$**

Operating temperature of a PEM fuel cell generally lies between $30 - 120°C$ [20, 24]. For the HY4, fuel cells are assumed to be operating at a constant $70°C$.

**Ideal water management**

The membrane is assumed to always be ideally hydrated, and limit current is never reached when remaining within the normal operating range of the fuel cell, meaning flooding of the electrodes is not an issue. This, combined with the static nature of the model, also means that hysteresis is not considered.

**Constant $\mathbf{R_m}$**

The electrolyte membrane has a constant resistance value.

**$\mathbf{I_{lim} = I_{max} + 35A}$**

Due to a lack of data points at high current densities, the limit current density has little to no effect on the parameter estimation results and is thus poorly estimated. The limit current density is therefore assumed to be slightly higher than the maximum current density. This will be further explained in Section 3.2.3.

## 3.3 Lithium-Ion Batteries

In both the hybrid powertrains considered, the secondary power source consists of one or more battery packs made out of multiple lithium-ion cells. Like fuel cells, they are electrochemical cells, but are self-contained. This means that once the chemical reaction has depleted the reactants, a potential must be applied to the electrodes to reverse the process.

When a potential is applied to the electrodes, meaning the cell is being charged, electrons are carried away from the lithium metal oxide anode, causing lithium ions to split from the electrode. These lithium ions then travel through the lithium salt electrolyte towards the graphite cathode to re-combine with the electrons and form lithiated carbon. During discharge, this process is reversed, and lithium ions will split from the carbon anode and travel back to the lithium cathode to form lithium metal, while the electrons pass through an external load and create a current. The processes at the anode and cathode during discharge of the cell are described by Equations 3.26 and 3.27 respectively. The simplified reaction is given in Equation 3.28. During charging, these reactions are reversed. The charge and discharge process of a cell are shown graphically in Figure 3.5. The cathode is assumed to be made up of lithium cobalt oxide, though there are several other metals which can be used.

$$LiC_6 \rightarrow C_6 + Li^+ + e^- \tag{3.26}$$

$$CoO_2 + Li^+ + e^- \rightarrow LiCoO_2 \tag{3.27}$$

$$LiC_6 + CoO_2 \rightarrow LiCoO_2 \tag{3.28}$$

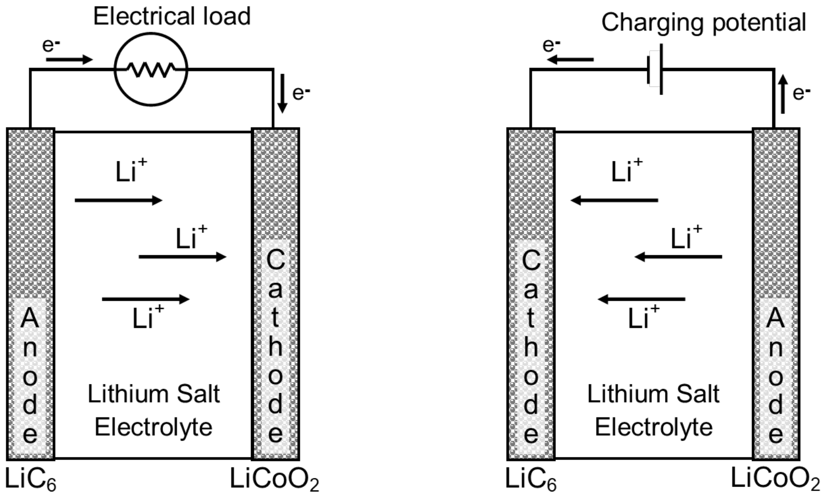

Figure 3.5: Simplified representation of the discharge (left) and charge (right) process in a single battery cell

### 3.3.1 Performance Model

The battery cell discharge curves are constructed using a simple empirical model. The cell voltage is then determined as a function of state-of-charge ($SoC$) and current draw ($I$). The cell is represented by an equivalent circuit model, specifically the Rint model, shown in Figure 3.6. This equivalent circuit model represents each cell as a potential source and an internal resistance. The cell voltage is then found using Equation 3.29. [33]

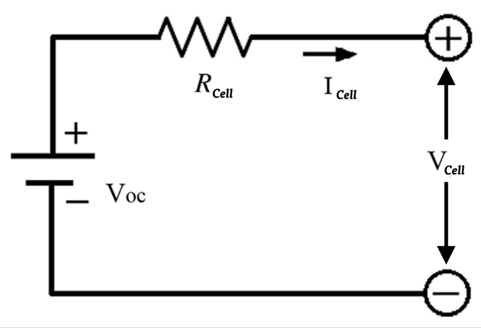

Figure 3.6: Simple equivalent electrical circuit of a battery based on the Rint model [34].

$$V_{cell} = V_{OC} - R_{cell} I_{cell} \tag{3.29}$$

First, the open-circuit voltage is determined using Equation 3.30, which accounts for activation (logarithmic), ohmic (linear), and concentration (exponential) voltage losses as a function of the cell depth-of-discharge, $DoD$ [35]. $DoD$ is the opposite of $SoC$, and describes the relative amount of energy extracted from the battery, while $SoC$ is the relative amount of energy which remains, meaning $DoD = 1 - SoC$. The maximum cell voltage for lithium-ion cells is $V_{max} = 4.2\,\mathrm{V}$. Internal losses due to current draw are accounted for by the internal resistance value found using Equation 3.31 [36]. Here the $SoC$ rather than the $DoD$ is used, and $Q_{rated}$ is the nominal capacity of the cell. The empirical coefficients $K_1$ through $K_9$ are determined once again using parameter estimation.

$$V_{OC} = V_{max} - K_1 \ln(K_2 DoD) - K_3 DoD - K_4 e^{K_5(DoD - K_6)} \tag{3.30}$$

$$R_{cell} = \frac{K_7 e^{K_8 SoC} + K_9}{Q_{rated}} \tag{3.31}$$

With the open-circuit voltage and internal resistance known, it is possible to determine the current drawn from the cell to achieve a certain output power. The battery power is defined by Equation 3.32. Note that voltages and currents are always referring to the cell values, and ‘cell’ subscripts are omitted for legibility. Only $P_{bat}$ refers to the total battery pack power, as indicated by the subscript. Note that if multiple battery packs are used in the powertrain, they are represented by a single, equivalent battery pack. If battery packs are connected in series, the number of parallel strings remains constant (e.i. equal to the number of parallel strings in a single pack), while the number of cells in a series string are added together. Alternatively, if the battery packs are connected in parallel, the number of cells in a series string remains unchanged, while the amount of parallel strings are summed. Combining Equations 3.29 and 3.32 yields a polynomial, shown in Equation 3.33, which can be solved to find the current drawn from the cell. The solution is given by Equation 3.34.

$$P_{bat} = V n_{series} I n_{parallel} = V I n_{cells} \tag{3.32}$$

$$R n_{cells} I^2 - V n_{cells} I + P_{bat} = 0 \tag{3.33}$$

$$I = \frac{V - \sqrt{V^2 - \frac{4RP_{bat}}{n_{cells}}}}{2R} \tag{3.34}$$

The current draw can now be used to determine the discharge rate of the battery through Coulomb counting, using Equation 3.35. Just like with fuel cells, the discharge efficiency is determined by the ratio between the open-circuit voltage and the actual voltage, Equation 3.36.

$$C = S\dot{o}C = \frac{I}{3600 Q_{rated}} \tag{3.35}$$

$$\eta_{bat} = \frac{V_{cell}}{V_{OC}} \tag{3.36}$$

Finally, if the rated energy capacity, $E_{rated}$, of the battery cell is not given, it can be found using Equation 3.37. The effective, useful capacity, $E_{act}$, which takes into account the internal losses, is a function of the current draw and internal resistance, and can be determined using Equation 3.38. Subtracting the effective energy capacity from the rated capacity will give the amount of energy which is lost [35].

$$E_{rated} = Q_{rated} V_{rated} + R I_{rated}^2 \frac{1}{C_{rated}} \tag{3.37}$$

$$E_{act} = E_{rated} - R I^2 \frac{1}{C} \tag{3.38}$$

### 3.3.2 Parameter Estimation

As with the fuel cell, coefficients $K_1$ through $K_9$ are determined by minimizing the value of the RMSPE, defined in Equation 3.23, of the cell voltages as a function of state of charge and current draw. The data used for the optimization, however, is different for the HY4's batteries to those in the Panthera.

The Panthera's battery packs are made up out of Samsung cells, for which discharge curves are available, and thus the coefficients are found by reducing the error of the voltages given in these curves. The results are shown in Figure 3.7. As indicated in the figure title, the optimization achieves an $\varepsilon_{RMSP} = 0.79\%$. More details of the parameter estimation results for the Panthera's batteries are given in Appendix B.2.2.

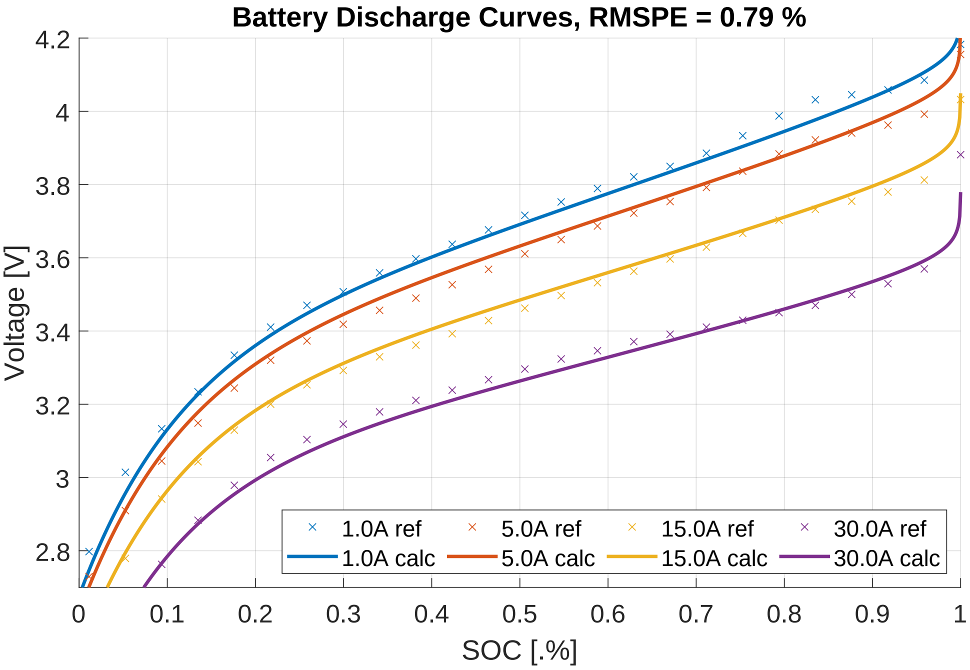

Figure 3.7: Panthera batteries discharge curve validation

The HY4 uses KOKAM cells in its battery packs, of which no discharge curves are readily available at the time of writing. Therefore, as with the fuel cell, the current, voltage, and $SoC$ data from the test flight will be used in the parameter estimation. Since there once again are no data points for low voltage or low $SoC$ values, a constraint is added to obtain more realistic discharge curves, which requires 10% of the capacity is lost when the cell is discharged at the maximum continuous current value. The resulting discharge curves returned by the model after determining $K_1 - K_9$ are shown in Figure 3.8. The detailed parameter estimation results for the HY4's batteries are given in Appendix B.2.1.

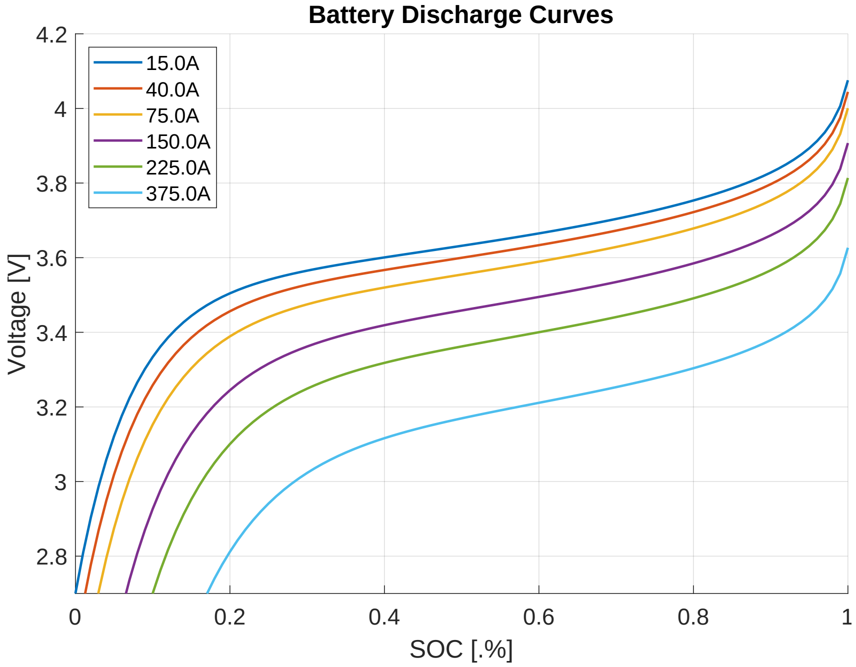

Figure 3.8: HY4 battery cell discharge curves resulting from parameter estimation

### 3.3.3 Summary of Assumptions

The battery model is subject to the following assumptions:

**Ideal Cell management**

Each cell in the battery packs is discharged at equal rates, meaning there never is a charge imbalance between the cells and all cells have equal voltages.

**Equivalent Battery Pack**

If multiple battery packs are installed in the aircraft, they are assumed to have the same configuration. They are modeled as a single battery pack which combines all separate packs in a single equivalent battery pack with equal performance.

$\mathbf{\Delta E_{cell}(I_{max}) = -10\%}$

If due to a lack of data points the discharge curves are poorly estimated at low voltage / state-of-charge values, a constraint is added which requires 10% of the cell capacity to be lost when discharging at the maximum continuous current draw.

$\mathbf{V_{max},\ V_{min} = 4.2V,\ 2.7V}$

The maximum and minimum voltages of a Lithium-ion cell are assumed to be 4.2 V and 2.7 V respectively. The nominal voltage is 3.7 V. While it is possible to overcharge the cells beyond the maximum voltage, and discharge as low as 2.5 V, this is not considered here as it greatly reduces the lifespan of the battery.

## 3.4 Internal Combustion Engine

The Panthera is fitted with a Rotax 915, a four-stroke 100 kW piston engine, which supplies most of the power during cruise flight. The engine class simply reads the performance table, obtained from the engine's operator manual [37], and interpolates the output power and fuel flow as a function of engine RPM and ambient air pressure (altitude).

$$P_{engine},\ \dot{m}_{fuel} = f_{interp}(\omega_{ICE}, p_{amb}) \tag{3.39}$$

## 3.5 Electric Motor and Generator

Both the HY4 and Panthera used permanent magnet synchronous AC electric motor (PMSEM) To drive the propeller shaft. A comparison made by Hayes and Goodarzi[35] shows that indeed AC motors are superiorly suited for EV application. As the name suggests, PMSEMs operate on alternating current. The magnetic field generated by the current in the stator windings, which interacts with the magnets to generate torque, spins at the same frequency as the current. The use of permanent magnets means the cost of PMSEMs is higher, but results in a higher efficiency, and lower operating cost due to the construction [38].

For the electric motors, performance tables are available which are used to determine the motor efficiency as a function of motor torque, $\tau_{EM}$, and motor RPM, $\Omega_{EM}$ (Equation 3.40). First, Equation 3.41 is used to determine the shaft torque from the shaft power, $P_{shaft}$, and rotational velocity, $\Omega_{EM}$. The electric power required is then determined using Equation 3.42. If an external torque is applied to the shaft, the electric motor will function as a generator and the electric power becomes an output. The output power of a generator connected to the shaft of the internal combustion engine is therefore determined using the same equations.

$$\eta_{EM} = f(\tau_{EM},\, \Omega_{EM}) \tag{3.40}$$

$$\tau_{EM} = \frac{30 P_{shaft}}{\pi \Omega_{EM}} \tag{3.41}$$

$$P_{EM} = \frac{P_{shaft}}{\eta_{EM}} \tag{3.42}$$

### 3.5.1 Summary of Assumptions

The electric motor / generator model is subject to the following assumptions:

$\tau_{\mathbf{BEMF}} = \tau_{\mathbf{shaft}}$

For an electric generator, the back-electromotive force (BEMF), or counter-electromotive force, which is the counter-torque generated by the produced current, equals the applied shaft torque. In case of an electric motor, the back EMF causes a counter voltage and limits the torque output at high RPM, but is assumed to be accounted for in the experimental data.

## 3.6 Propeller

The thrust and power required by the propeller are once again determined using performance maps. For the two aircraft under consideration, these data tables have a slightly different format, since one uses a fixed-pitch propeller, while the other is equipped with a constant-speed or variable pitch propeller. Both cases are covered in Sections 3.6.1 and 3.6.2. Since there is no test data available for the propeller specifically, the flight test data will be used for validation. This will be covered in Chapter 5.

### 3.6.1 Fixed Pitch Propeller

The HY4 has a fixed pitch propeller, which means that the thrust and power coefficients, $C_T$ and $C_P$, can be determined using a polynomial function of advance ratio, $J$, represented by Equation 3.44, where $J$ is defined by Equation 3.43. The required shaft power is then determined using Equation 3.46.

The propeller thrust, $T$, can then be determined by on of two ways. Either the thrust is determined directly from the thrust coefficient using Equation 3.48, or by first determining the propeller efficiency with Equation 3.45, followed by the thrust formula in Equation 3.47 [19, 39]. Therefore, if the airspeed is known, thrust is controlled by the propeller RPM, $\Omega_{prop}$.

$$J = \frac{60v}{D_{prop}\Omega_{prop}} \tag{3.43}$$

$$C_P,\ C_T = f(J) \tag{3.44}$$

$$\eta_{prop} = J\frac{C_T}{C_P} \tag{3.45}$$

$$P_{shaft} = \rho\left(\frac{\Omega_{prop}}{60}\right)^3 D_{prop}^5 C_P \tag{3.46}$$

$$T = \eta_{prop}\frac{P_{shaft}}{v} \tag{3.47}$$

$$T = \rho\left(\frac{\Omega_{prop}}{60}\right)^2 D_{prop}^4 C_T \tag{3.48}$$

### 3.6.2 Constant Speed Propeller

The Panthera uses a constant speed or variable pitch propeller. In this case the thrust coefficient is given by a lookup table as a function of $C_P$ and $J$ (Equation 3.49). The power coefficient then is determined by rewriting Equation 3.46 into the form given by Equation 3.50, where both RPM and shaft power are now inputs. The thrust is found using the same methods as for a fixed pitch propeller, either using Equations 3.45 and 3.47 or using Equation 3.48.

$$C_T = f(J, C_P) \tag{3.49}$$

$$C_P = \frac{P_{shaft}}{\rho\left(\frac{\Omega_{prop}}{60}\right)^3 D_{prop}^5} \tag{3.50}$$

## 3.7 Powertrain Assembly Model

The Powertrain model links all components together and passes on information where needed. First, the powertrain model accounts for a potential gearbox. To increase the efficiency and torque output, sometimes electric motors come with integrated, planetary gearboxes. An exampled of such a motor is shown in Figure 3.9. The gear ratio is defined as the ratio between the propeller (or power) shaft rotational speed and the motor (or generator) rotational speed. Whether a gearbox is used in the powertrain model depends on the provided data. If the motor efficiency map uses the same range for rotational speed as the propeller limits, no gearbox is used. If data shows that the motor has a significantly higher speed range, a gearbox is added with the gear ratio determined by Equation 3.51. In this case, a constant efficiency factor $\eta_{GB} = 0.98$ is added to account for mechanical losses.

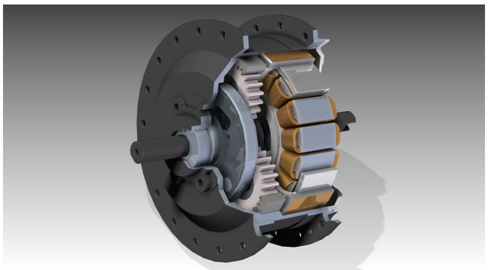

Figure 3.9: Example of an electric motor with integrated gear system [i]

$$GR = \frac{\Omega_{prop_{max}}}{\Omega_{EM_{max}}} \tag{3.51}$$

If several coaxial motors are connected to the same shaft, they all run at equal RPM, but each one provides an equal part of the total shaft power and torque. The motor torque, accounting for the gearbox and number of coaxially mounted motors, is determined by Equation 3.52.

$$\tau_{EM} = \frac{GR \cdot \tau_{prop}}{n_{coax}} \tag{3.52}$$

Next, since the batteries, fuel cells, and electric generator all supply DC current, while the electric motor requires AC current, an inverter is required which also acts as the motor's speed controller. An electric efficiency for the inverter of $\eta_{inv} = 0.95$ is assumed by default. This value is adjusted as needed to reduce errors when comparing power draw from experimental data during validation.

For the hybrid fuel cell powertrain, the required shaft power, found as described in Section 3.6, is multiplied with the motor and inverter efficiencies to determine the electrical power required. Any auxiliary power requirements are added to obtained to total electric load, as given by Equation 3.53. The fuel cells, or engine, methods are called to determined their respective power outputs and the required battery power is then determined by simply subtracting their power output from the total power required, as shown in Equation 3.54. For the hybrid electric powertrain, the same method is used, though now the battery power is found using Equation 3.55.

$$P_{elec_{tot}} = P_{shaft}\eta_{EM}\eta_{inv} + P_{aux} \tag{3.53}$$

$$P_{bat}|_{HY4} = P_{elec_{tot}} - P_{FCS} \tag{3.54}$$

$$P_{bat}|_{Panth} = P_{elec_{tot}} - P_{engine}\eta_{gen} \tag{3.55}$$

### 3.7.1 Summary of Assumptions

The powertrain model is subject to the following assumptions:

$\boldsymbol{\Omega_{prop_{max}} \neq \Omega_{EM_{max}} \rightarrow GR = \frac{\Omega_{prop_{max}}}{\Omega_{EM_{max}}}}$

If the maximum propeller RPM and maximum motor RPM from the data tables do not match, a gearbox is assumed to be in place to make sure that both can operate at their respective maximum rotational velocities, unless specified otherwise.

$\boldsymbol{\eta_{GB} = 0.98}$

If a gearbox is used, a 2% mechanical loss is added when determining the power required.

$\boldsymbol{\eta_{inv} = 0.95}$

The electric efficiency of the inverter is assumed to be $\eta_{inv} = 0.95$.

---

[i] Image from https://www.avdweb.nl/

This page is intentionally left blank.

# 4 Control Problem Formulation

To determine the performance capabilities of different powertrain configurations, an optimal control problem is defined which returns the optimal flight trajectory for certain performance indices, and the control and energy management strategies. In Section 4.1, the state variables and system dynamics are defined, and the control variables are identified. The system dynamics can then also be used, combined with the control variable values obtained from the flight test data, to reconstruct the flight path and validate the combination of the aircraft model and state equations in Chapter 5.

## 4.1 State Equations and Control Variables

The first three state variables are distance $d$, altitude $h$, and indicated airspeed $v_{IAS}$, which describe the two-dimensional flight profile as covered in Section 3.1. The fuel mass, $m_{fuel}$, and battery state-of-charge, $SoC$, are added to describe the amount of energy stored, leading to the final state variable vector shown in Equation 4.1.

The state derivative equations, which form the system dynamics, were defined previously in Equations 3.1 to 3.3 for the equations of motion, Equations 3.19 and 3.39 giving the fuel mass rate for a fuel cell or engine, and Equation 3.35 for the battery discharge rate. This results in two different state derivative vectors: the one in Equation 4.2 for the HY4, and Equation 4.3 for the Panthera.

$$\boldsymbol{x} = \begin{bmatrix} d & h & v_{IAS} & m_{fuel} & SoC \end{bmatrix} \tag{4.1}$$

$$\dot{\boldsymbol{x}}_{HFCP} = \begin{bmatrix} v_{TAS} \cdot \cos\gamma \\ v_{TAS} \cdot \sin\gamma \\ \frac{T-D}{m} - g_0 \cdot \sin\gamma \\ \Lambda_{H_2} M_{H_2} \frac{I}{F n_{ean}} n_{cells} \\ \frac{I_{bat}}{3600 Q_{rated}} \end{bmatrix} \tag{4.2}$$

$$\dot{\boldsymbol{x}}_{HEP} = \begin{bmatrix} v_{TAS} \cdot \cos\gamma \\ v_{TAS} \cdot \sin\gamma \\ \frac{T-D}{m} - g_0 \cdot \sin\gamma \\ f(\Omega_{ICE},\ h) \\ \frac{I_{bat}}{3600 Q_{rated}} \end{bmatrix} \tag{4.3}$$

The control parameters required to calculate the system dynamics also vary for both aircraft. For the HY4, with its fuel cells and fixed pitch propeller, there are three control variables needed: propeller RPM $\Omega_{prop}$, flight path angle $\gamma$, and fuel cell current draw $I_{FC}$. The control variable vector is thus given by Equation 4.4. The Panthera, whoever, requires engine RPM $\omega_{ICE}$, as a control parameter instead of fuel cell current draw, and since it is equipped with a variable pitch propeller, shaft power $P_{shaft}$ is needed as additional input. This results in the control vector given by Equation 4.5.

$$\boldsymbol{u}_{HFCP} = \begin{bmatrix} \Omega_{prop} & \gamma & I_{FC} \end{bmatrix} \tag{4.4}$$

$$\boldsymbol{u}_{HEP} = \begin{bmatrix} P_{shaft} & \Omega_{prop} & \gamma & \Omega_{ICE} \end{bmatrix} \tag{4.5}$$

To account for the different state and control vectors for different powertrains, one option is to create completely separate problem definitions for each powertrain architecture. However, to increase the user-friendliness of the code, new variables and constraints are introduced, allowing different powertrain configurations to be defined without the need to alter the code, in accordance with the SOLID principles, discussed in section 2.1.

A dependent variable, $CPS$, is introduced, which stands for "controlled power system". This variable points towards the power system object controlled directly by a control variable (e.i. the fuel cell or engine). The batteries can then be referred to using the "supplementary power system" dependent variable, $SPS$. This allows the control variables $I_{FC}$ and $\Omega_{ICE}$ to be replaced by a single, dependent control variable, $\mathcal{U}_{CPS}$. Likewise, the fuel mass derivative function is defined by $f_{CPS_{fuel}}(\mathcal{U}_{CPS})$. This change has no effect on the solution of the optimal control problem, but facilitates the problem definition and allows for a single, universal notation of the state and control vectors and the system dynamics vector, regardless of powertrain configuration.

To avoid the control vector changing size, shaft power is always included as a control parameter. Since the shaft power control variable has no effect when a fixed pitch propeller is used, a consistency constraint is added to the problem in that case, which requires the shaft power input equals the shaft power required by the propeller, according to Equation 3.46. While it is kept in the control vector, it no longer serves as an input at that point, but as indicator of the power required.

Finally, after an initial set of runs, the solutions showed over-controlling of the flight path angle, resulting in large oscillations in the results for state functions. To mitigate this, the choice was made to move the flight path angle to the state vector, and instead control it indirectly through the value of its derivative. This allows an integral cost to be added to the cost function Equation 2.1, defined by Equation 4.6, which aims to dampen the control of the flight path angle. $c_\gamma$ is a scaling factor which is varied to avoid this part of the cost function dominating the cost function of the performance index of interest.

$$L_\gamma = \int_{t_0}^{t_f} c_\gamma \dot{\gamma}^2 \, dt \tag{4.6}$$

The final state and control vectors are then defined by Equations 4.7 and 4.8, and the state dynamics are specified in Equation 4.9, where $\mathcal{U}_{CPS}$ refers to either the engine RPM or fuel cell current, depending on which component is used, and $f_{CPS_{fuel}}(\mathcal{U}_{CPS})$ refers to either Equation 3.19 or Equation 3.39.

$$\boldsymbol{x} = \begin{bmatrix} d & h & v_{IAS} & \gamma & m_{fuel} & SoC \end{bmatrix} \tag{4.7}$$

$$\boldsymbol{u} = \begin{bmatrix} P_{shaft} & \Omega_{prop} & \dot{\gamma} & \mathcal{U}_{CPS} \end{bmatrix} \tag{4.8}$$

$$\dot{\boldsymbol{x}} = \begin{bmatrix} \dot{d} \\ \dot{h} \\ \dot{v} \\ \dot{\gamma} \\ \dot{m}_{fuel} \\ \dot{SoC} \end{bmatrix} = \begin{bmatrix} v_{TAS} \cdot \cos\gamma \\ v_{TAS} \cdot \sin\gamma \\ \frac{T-D}{m} - g_0 \cdot \sin\gamma \\ \dot{\gamma} \\ f_{CPS_{fuel}}(\mathcal{U}_{CPS}) \\ \frac{I_{bat}}{3600 Q_{rated}} \end{bmatrix} \tag{4.9}$$

Another important consideration is the use of indicated airspeed in the state vector, while the equations of motion, used to determine the state derivatives, require the use of true airspeed. To account for this, indicated airspeed is converted to true airspeed based on the altitude, and the change in true airspeed is subsequently converted back to indicated airspeed using Equation 4.10.

$$\dot{\boldsymbol{v}}_{IAS} = f_{tas2cas}(v_{TAS} + \dot{v}_{TAS},\ h) - v_{IAS} \tag{4.10}$$

Conversion from indicated airspeed, assumed to equal calibrated airspeed, to true airspeed is done using Equation 4.11 [40]. Contrarily, the function to convert true airspeed back to indicated airspeed, denoted by $f_{tas2cas}$, is obtained by rewriting Equation 4.11.

$$v_{TAS} = \sqrt{\frac{2\gamma}{\gamma-1}\frac{p}{\rho}\left(\left[1+\frac{p_0}{p}\left(\left[1+\frac{\gamma-1}{2\gamma}\frac{\rho_0}{p_0}v_{CAS}^2\right]^{\frac{\gamma}{\gamma-1}}-1\right)\right]^{\frac{\gamma-1}{\gamma}}-1\right)} \tag{4.11}$$

Using indicated airspeed as a state variable over true airspeed, while adding this extra required conversion step when determining the dynamics, makes it easier to apply bounds. The indicated airspeed, assumed equal to calibrated airspeed and equivalent airspeed, $v_{IAS} = v_{CAS} = v_{eq}$, does not vary with altitude. This means that any published airspeed limits can be applied as constant bounds.

## 4.2 Path Constraints

Path constraints are applied at every point in time. Three path constraints are required in combination with the chosen dynamics model. First, Equation 4.12 prevents excessive load on the batteries by limiting the battery current draw, found using Equation 3.34, to the maximum rated current draw for the used cell.

$$g_{path_1}: \quad I_{batt} \leq I_{batt_{max}} \tag{4.12}$$

Similarly, the torque of the electric motor, which follows from the propeller shaft power and RPM, must not exceed the maximum torque specified by the manufacturer, forming the second path constraint given by Equation 4.13.

$$g_{path_2}: \quad \tau_{EM} \leq \tau_{EM_{max}} \tag{4.13}$$

Finally, to avoid runaway values when extrapolating the propeller power and thrust coefficients, the advance ratio is bound by the maximum and minimum values occurring in the provided propeller data file, as shown in Equation 4.14.

$$g_{path_3}: \quad J_{min} \leq J \leq J_{max} \tag{4.14}$$

The consistency constraint defined by Equation 4.15 is applied only when a fixed-pitch propeller is used. In that case, the constraint ensures that the value of the shaft power control variable, represented as $u_{P_{shaft}}$, is equal to the propeller shaft power determined as a function of the propeller RPM. Once again, this is implemented to comply with the SOLID principles. While the fixed pitch propeller only requires a single input, RPM, the variable pitch propeller requires two control variables: RPM and shaft power. Adding this consistency constraint means the code does not need to be modified when switching propeller types.

$$g_{path_{eq_1}}: \quad u_{P_{shaft}} = \rho\left(\frac{\Omega_{prop}}{60}\right)^3 D_{prop}^5 C_P \tag{4.15}$$

## 4.3 Objectives

The main focus is to determine the trajectories and energy management behavior for fuel-optimal flight. Optimizing the flight path for minimum fuel consumption is the best way to identify the best energy management strategies, as each component must perform optimally to achieve this. To minimize fuel consumption, naturally the engine or fuel cell should run at best efficiency, or at least optimally trade-off efficiency for power only when absolutely necessary. Furthermore, it also ensures the batteries are discharged with minimal energy losses, and to their full capacity, which requires minimal internal losses.

Therefore, the main cost function is defined in Equation 4.16. The fuel cost is defined as the square of the percentage fuel used per 100km. This cost function is chosen as it normalizes the cost with respect to the range and the fuel capacity of the aircraft, reducing potential scaling issues [16]. The integral cost contains the square of the flight path angle rate to avoid over-control, as mentioned previously. $c_\gamma$ is a scaling coefficient which is varied when needed to vary the influence of the integral cost.

$$J_{fuel} = \left[ \frac{\left(1 - \frac{m_{fuel}(t_0)}{m_{fuel}(t_f)}\right) \times 100}{d(t_f) \times 10^{-5}} \right]^2 + \int_{t_0}^{t_f} c_\gamma \dot{\gamma}^2(t)\, dt \tag{4.16}$$

To determine how much fuel exactly is saved by flying the fuel-optimal trajectory, the minimum flight time trajectory is found as means of comparison, using the cost function given in Equation 4.17. The flight time is normalized with respect to the flight time required to fly the specified range at the maximum allowed airspeed, $v_{NE}$.

$$J_{time} = \left( \frac{t_f \times v_{NE}}{d(t_f)} \right)^2 + \int_{t_0}^{t_f} c_\gamma \dot{\gamma}^2(t)\, dt \tag{4.17}$$

Finally, Equation 4.18 is used as cost function to determine the maximum range of an aircraft. Again, range is expressed in hundreds of kilometers to avoid scaling issues. The maximum range problem is effectively a special case of the fuel minimization problem, as maximum range will only be achieved when flight conditions are similar to those for best fuel economy.

$$J_{range} = -\left( d(t_f) \times 10^{-5} \right)^2 + \int_{t_0}^{t_f} c_\gamma \dot{\gamma}^2(t)\, dt \tag{4.18}$$

# 5 Validation

Validation of the models is performed by using the values of the control variables from flight test data of the HY4 fuel cell aircraft. Combining the aircraft model with the defined control problem, specifically the dynamics equations in Equation 4.9, allows reconstruction of the flight profile from the flight test data using the values of the control variables (Equation 4.8) from the flight data. To reconstruct the flight trajectory, the state variables are assumed to vary linearly according to Equation 5.1, with a time step of $\Delta t = 1\,\mathrm{s}$.

$$x_{t+\Delta t} = x_t + \dot{x}(u_t) \tag{5.1}$$

No values are available for the flight path angle or its derivative, $\gamma$ and $\dot{\gamma}$, so the flight path angle is estimated by Equation 5.2 using speed and altitude data instead, and $\gamma$ is used as a control variable instead of its derivative. Plots of the state variables returned by the model compared to the flight test data, as well as the respective error plots, are shown in Figure 5.1. Note that whenever experimental data is used for parameter estimations or validation, Gaussian data smoothing is applied.This removes outliers and excessive jitter in the data, and makes plots easier to read while having minimal impact on the results.

$$\gamma_t = \sin^{-1}\frac{\dot{h}}{v_{TAS}} = \sin^{-1}\frac{h_{t+1} - h_t}{v_{TAS_t}} \tag{5.2}$$

Results for the distance, altitude, and fuel mass all have errors with an order of magnitude $\mathcal{O}(\varepsilon_{RD}) < 1$, with RMSPE values of $\varepsilon_{RMSP_d} = 2.24\%$, $\varepsilon_{RMSP_h} = 2.74\%$, and $\varepsilon_{RMSP_{m_{fuel}}} = 1.79\%$ respectively. The indicated airspeed and battery state-of-charge, however, show significant deviations. Investigating the origin of these errors leads to the propeller model for both cases. A possible source of significant errors is the airspeed data from the test flight itself. During the flight test, the pitot-static system had calibration issues, which means that there are inherent errors in the airspeed data. These errors are likely aggravated by the estimation of the flight path angle using Equation 5.2. If we compare the recorded shaft power and the shaft power determined by Equation 3.46, again a function of airspeed, using the available propeller performance table, Figure 5.2 shows that these values also have considerable differences.

Singling out the individual components will give more insight in the source of the differences. Starting with the battery state-of-charge differences. Comparing the battery SoC from the flight data with the SoC predicted by Equation 5.1 using the battery current draw data from the flight test in Figure 5.3 shows that the errors introduced by the Coulomb counting method are reasonable, with an RMSPE of only $\varepsilon_{RMSP} = 2\%$, meaning the calculation of SoC and discharge rate is done correctly.
The battery current draw and cell voltages in function of the battery power draw from the flight test data are plotted in Figure 5.4 and Figure 5.5. This proves that the battery model accurately approximates the current and voltage values from the flight data, with a root-mean-squared error of at most $\varepsilon_{RMS} = 0.18\%$. The battery model is thus proven accurate.

This leads to the conclusion that the battery power required is the main source of these errors. Shifting focus to the fuel cell model, Figure 5.6 shows that the fuel cell voltages are modeled accurately as a function of current draw. With the fuel cell and battery model both validated, and the only possible cause of the errors in battery SoC being the power demanded from the batteries, this means that, according to Equation 3.53 and Equation 3.54, the erroneous power requirements can be traced back to either the electric motor or the propeller model. Comparing the recorded shaft power and the shaft power determined by Equation 3.46, a function of airspeed, using the available propeller performance data, Figure 5.2 shows that these values also have considerable differences. Unless there are errors in the provided motor or propeller

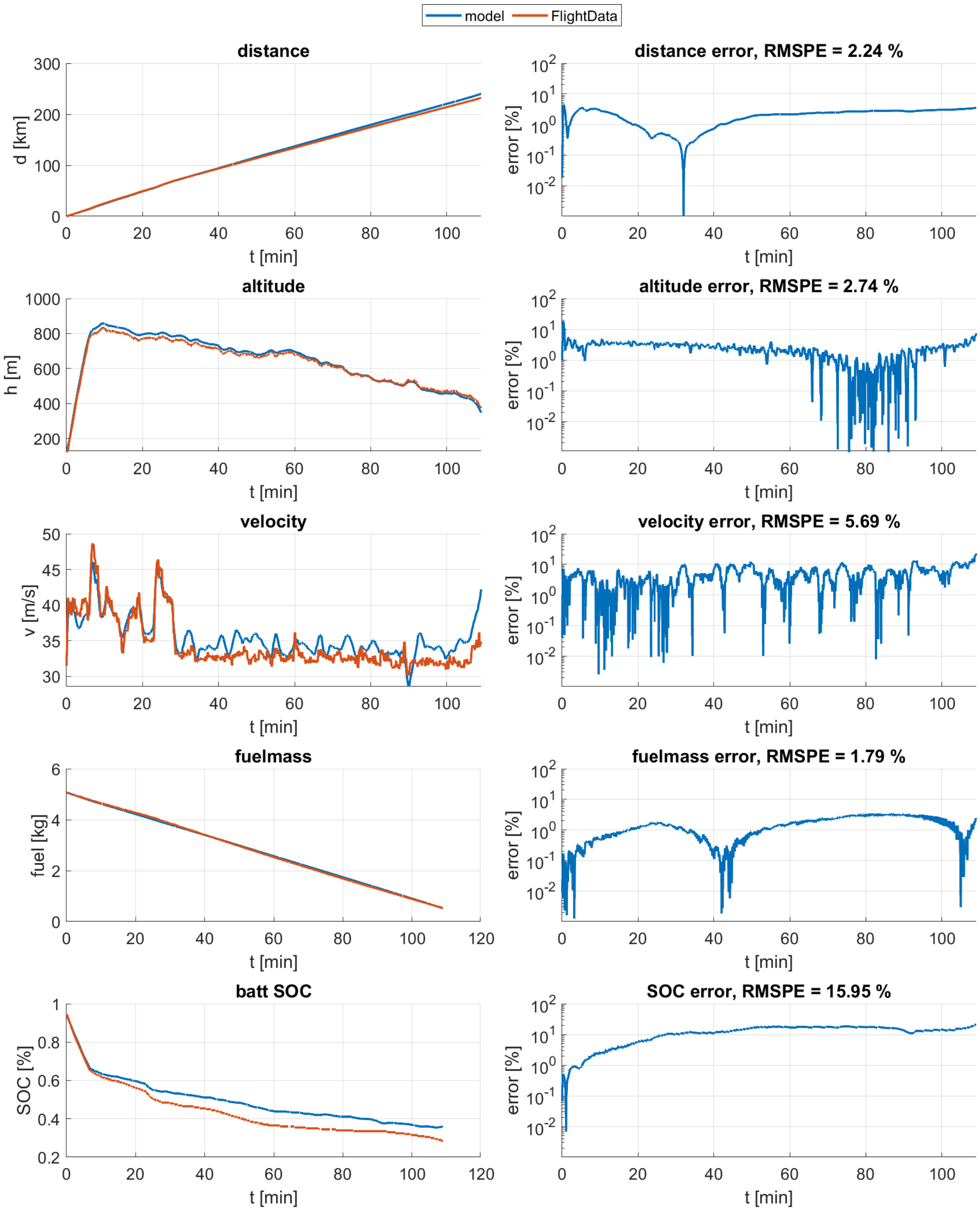

Figure 5.1: Flight path validation using flight test data of the HY4

performance data, the errors in the airspeed test data are the main cause of the observed discrepancies.

To compensate for the underestimation of shaft power, the errors in battery state of charge are reduced by decreasing the constant efficiency of the inverter in the powertrain by $\Delta eta_{inv} \approx -0.05$, which could account for any power demands from unknown components or other aircraft systems.

Since the errors are caused by erroneous airspeed data, and all components return expected values, the model is still considered validated. The decision is therefore made to retain the cur-

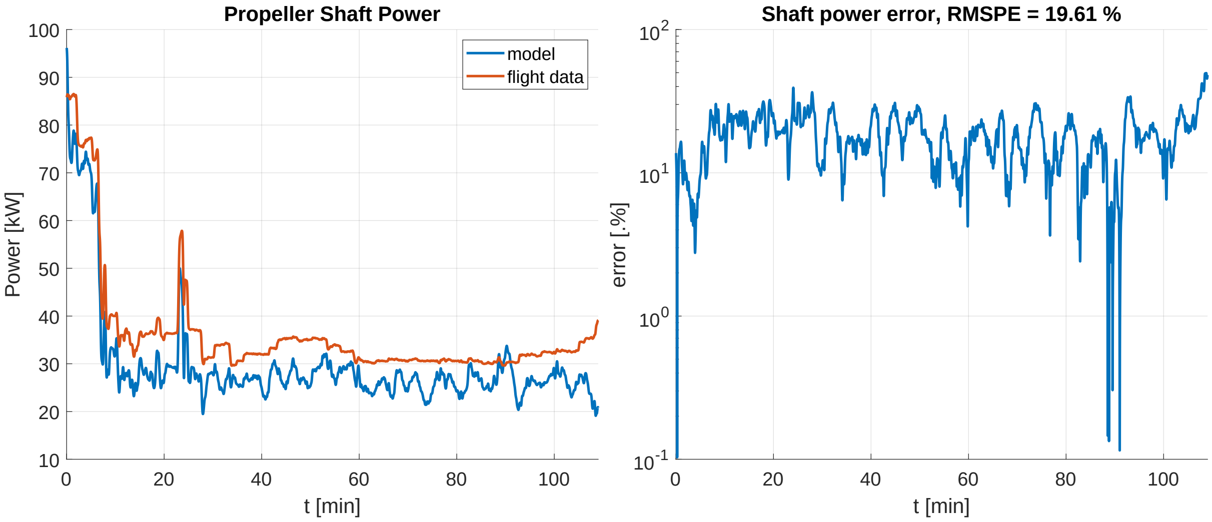

Figure 5.2: Propeller shaft power validation

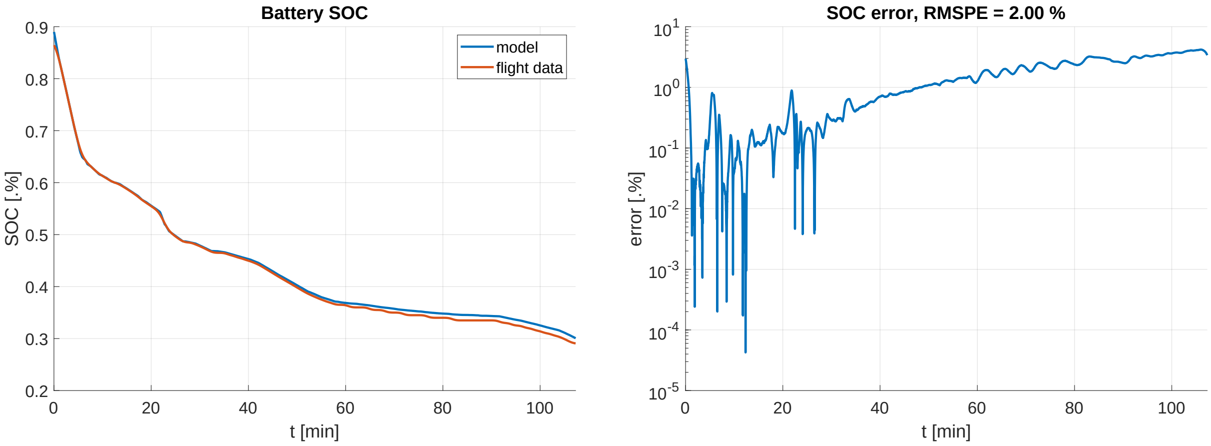

Figure 5.3: Battery SOC validation using current data from the test flight

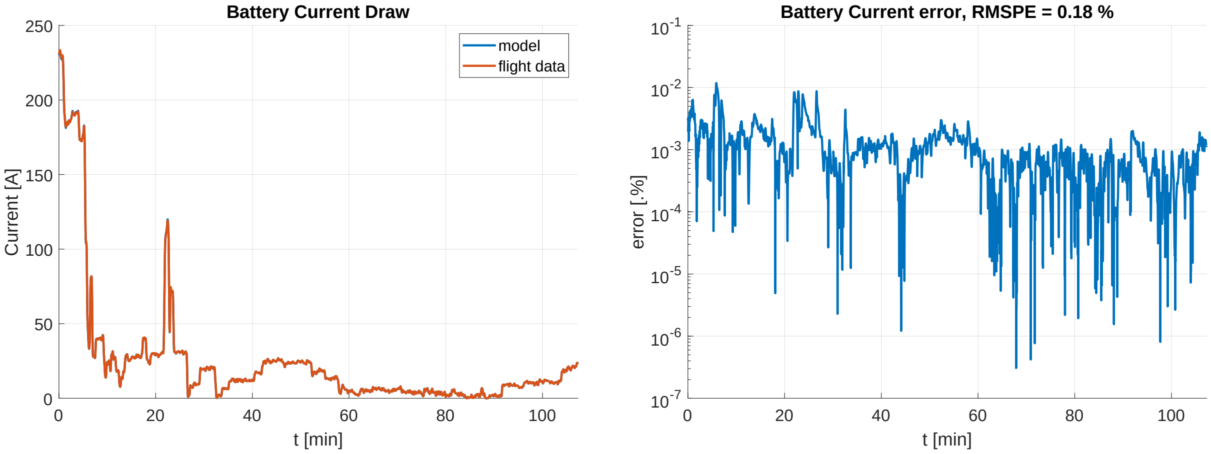

Figure 5.4: HY4 batteries current draw validation

rent model and performance data, and use it as is in the upcoming optimal control evaluations. If more accurate data would become available in the future, the validation can be revisited. Additionally, as more accurate data sets become available for the components, these can simply be added to, or replace the current files in the tool's file structure to expand the knowledge base

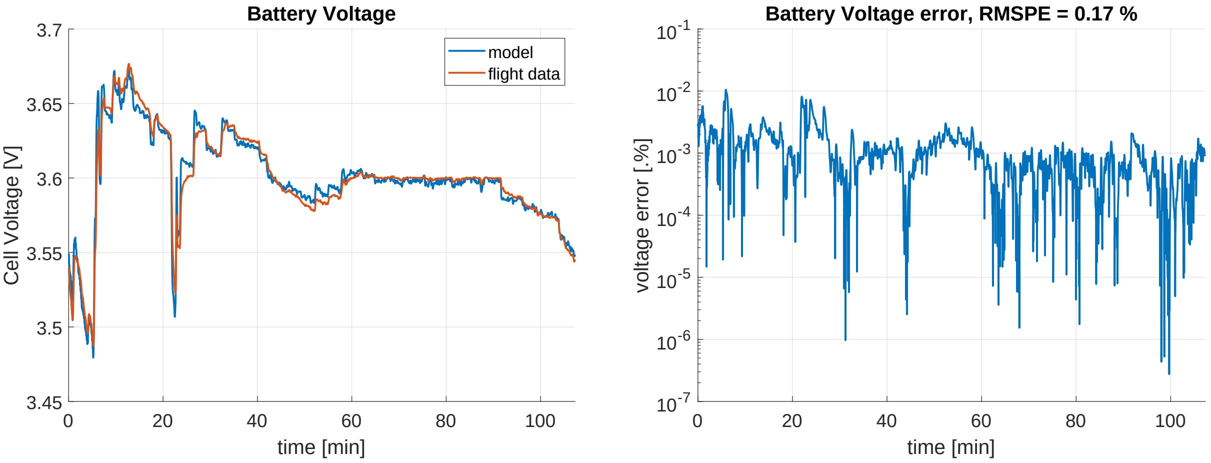

Figure 5.5: Discharge curves obtained after parameter estimation

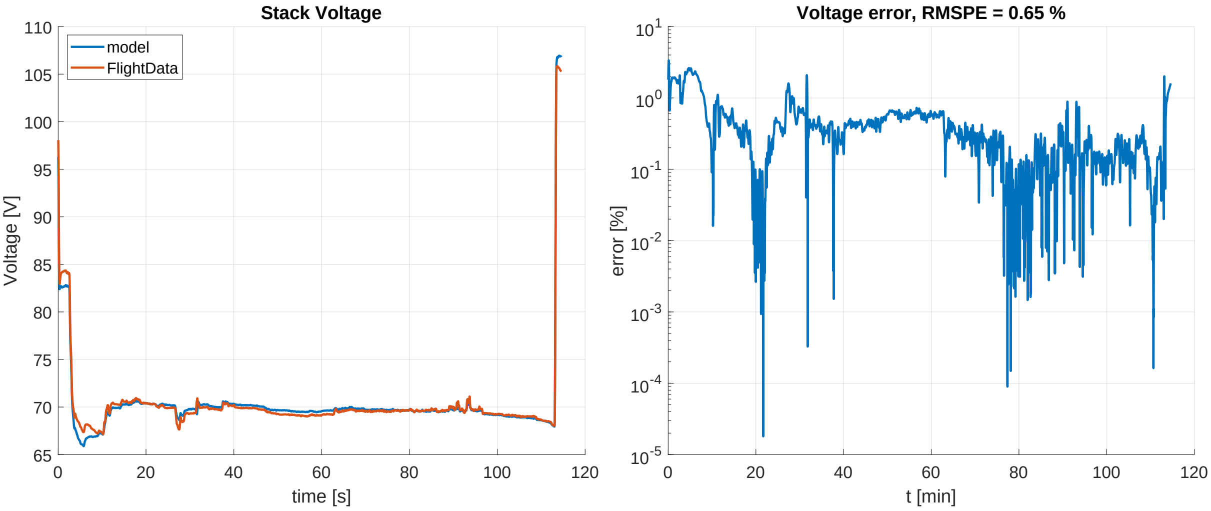

Figure 5.6: Stack Voltage data comparison and errors after parameter estimation

and improve the accuracy of the results.

Finally, Figures 5.4 to 5.6 show that the static, semi-empirical suffice to model electrochemical cells when evaluating powertrain and aircraft flight performance, yielding a positive answer to Research Question 2, posed in Section 1.2.

# 6 Results

The results obtained for the Panthera are discussed first in Section 6.1, to obtain a baseline for comparison with the HY4. Solutions for the HY4 are covered next in Section 6.2. For general performance evaluations, a single phase problem setup is used. The single phase solutions are compared to their multiphase equivalents in Section 6.4. Note that functions of flight path angle, flight path angle rate, distance, and fuel mass will not be included in the plots. The function for flight path angle in time, and its derivative, do not add much to the performance evaluation, and are thus left out. Fuel mass and distance, on the other hand, appear linear in time, and therefore only their values in the final boundary points are reported. Complete plots of all state and control functions can be found in Appendix G.

In general, it was found that the objective functions showed very 'flat' behavior for the fuel-minimization problems, particularly for the HY4. This means that for small changes in boundary conditions or convergence tolerances, the trajectories, particularly the altitude profiles, could vary wildly while the differences in the objective value remain negligible. Hence, the objective function contains many local minima which the optimizer gets caught in.

## 6.1 Panthera Hybrid Electric Aircraft

This section discusses the optimal trajectories obtained for the Panthera hybrid electric aircraft for different cost functions. Starting off with the main focus of the analysis, Section 6.1.1 reviews the solutions for fuel-optimal flight, and determines the potential general target values of the flight parameters to approximate the ideal trajectories for any range. Next, Section 6.1.2 presents the solutions for minimum flight time, and compares these with the fuel-optimal flight profiles to get an understanding of exactly how much fuel or time can be saved using either.

### 6.1.1 Minimizing Fuel Consumption

For ranges of 100 km, 300 km, 500 km, and 1000 km, the fuel consumed and the fuel remaining are given in Figure 6.1 after optimizing the flight path for minimum fuel consumption.
The flight profile, described by the altitude and airspeed, power setting, given by shaft power and propeller RPM, and energy management, defined by the engine RPM and (slope of) the battery state of charge, are plotted as a function of time in Figure 6.2. The flight times are given in the figure legend. This plot also includes the solution for the maximum range of 1524 km.
The results show flight profiles which remain consistent with increasing range. For shorter ranges where the cruise altitude is not reached before the start of the descent, the flight profile takes a parabolic shape. Additionally, the airspeed plot for a range of 100 km in Figure 6.2 reaches a slightly higher value of $v \approx 63.9\,\mathrm{m\,s^{-1}}$, than the flight profiles for longer ranges. This is due to the batteries delivering relatively more power compared to longer range flights, as indicated by the steeper slope of the state-of-charge function.

For ranges where the desired cruise altitude is achievable, the aircraft accelerates to a speed of about $v \approx 61.5\,\mathrm{m\,s^{-1}}$ while climbing to $h \approx 670\,\mathrm{m}$. Approximately 23% of the batteries is used to boost power output during the climb, while the engine is kept running at a constant $\Omega_{ICE} \approx 4850 RPM$. As fuel is burned, the aircraft keeps climbing gradually during the cruise. Also, the airspeed keeps reducing slowly as the aircraft becomes lighter. Once the initial climb is over, the batteries are discharge more or less evenly along the flight, and reach their minimum state-of-charge when the descent begins. The exception to this is the maximum range case, where the batteries are already depleted fully at a point before the start of the descent, at around 300 min into the flight. However, its seems like performance does not suffer, as the airspeed is maintained and the engine RPM is not increased for the loss of power. This, combined with

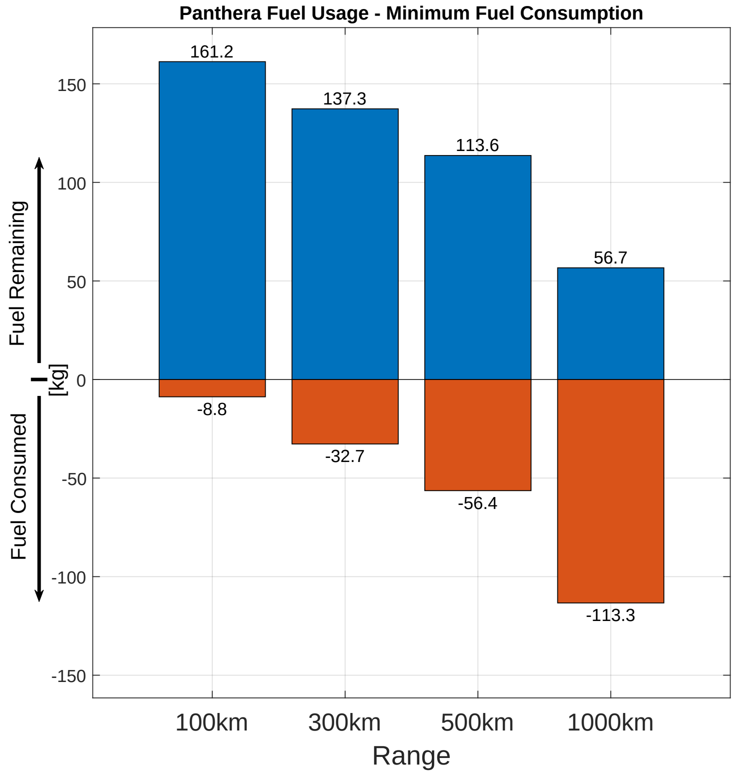

Figure 6.1: Fuel consumption of the Panthera for different ranges.

the slow discharge of the batteries, indicates that the batteries do not contribute significantly to the power delivery past the initial climb.

### Power Draw Distribution and Battery Uilization

Figure 6.3 offers a closer look at the electric power delivered by the batteries and the generator connected to the combustion engine for two ranges, 100 km and 500 km. The power plots confirm the findings from before: the generator power, which equals the engine power multiplied with the generator efficiency, remains fairly constant throughout both flights, while the battery power, after giving an initial boost during climb, quickly reduces. This makes sense, since the battery discharge efficiency, Equation 3.36, lowers with cell voltage, which in turn decreases with state-of-charge and increasing current draw. Hence, by keeping the discharge current low, a high discharge efficiency is maintained. Battery current and discharge efficiency are plotted in the right-hand side plots of Figure 6.3. To minimize fuel consumption, the battery current draw must remain sufficiently high, however, to ensure they are fully depleted by the end of the flight. Therefore, battery power reduces with increasing range. Due to the low energy capacity of the batteries, this results in low power contributions of the batteries at longer ranges (median $P_{batt} \approx 4\,\mathrm{kW}$ for a 500 km flight), and thus has little influence on the actual airspeed which can be maintained.

### Generalized Parameter Targets

Using the median values of each of the parameters from Figure 6.2, listed in Table 6.1, and taking the weighted average with respect to flight range, yields a general target value for each one to minimize fuel consumption when flying the aircraft. The values for a range of 100 km are ignored here, as the target cruise altitude is not reached during such a short flight. Not accounting for variations due to the changing mass, this results in the Panthera having best fuel economy when

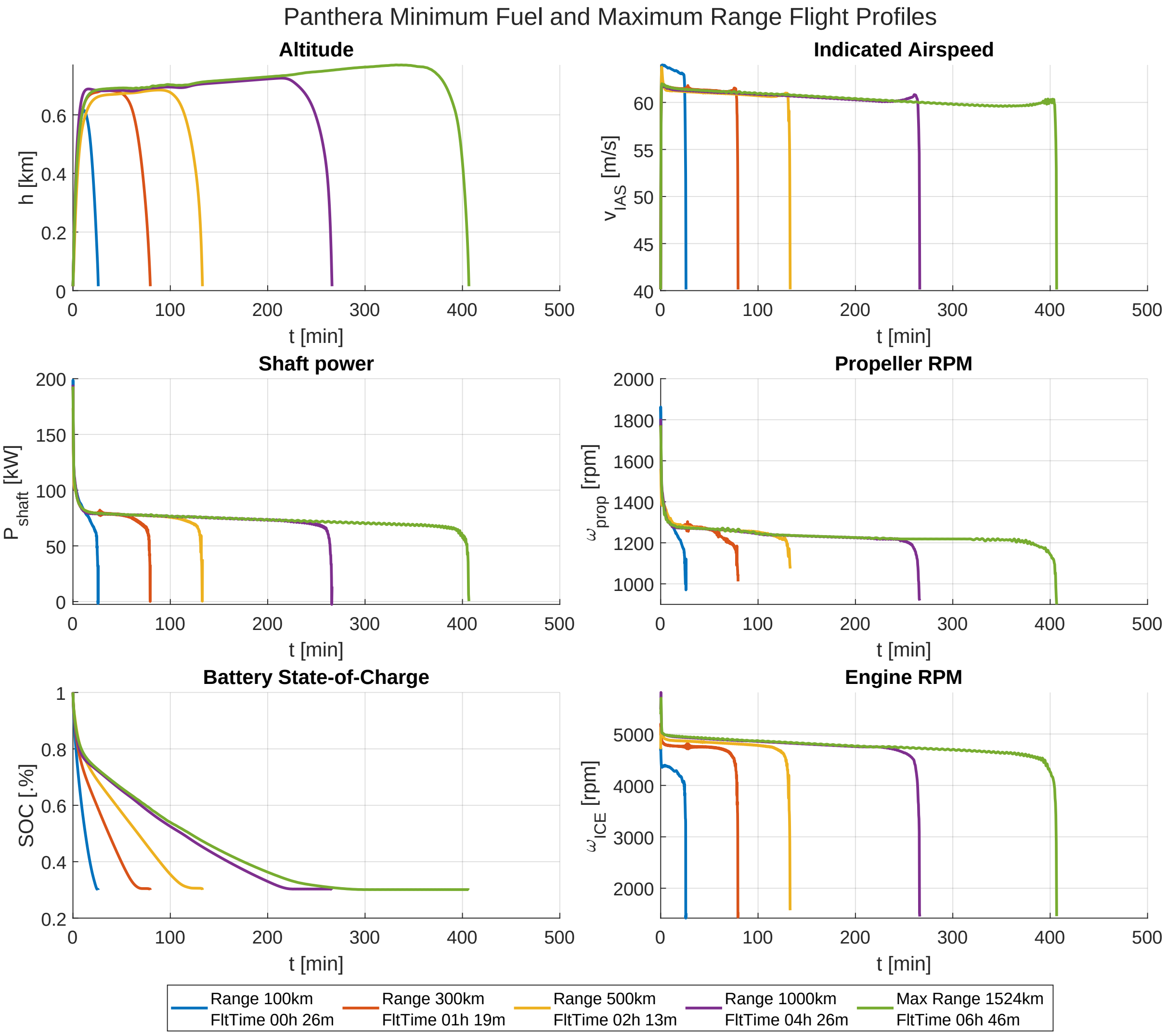

Figure 6.2: Optimal flight path results for minimum fuel consumption, including maximum range, for the Hybrid Panthera.

flown at an altitude of $h \approx 700\,\mathrm{m}$ at an indicated airspeed of $v \approx 61\,\mathrm{m\,s^{-1}}$. The shaft power is kept more or less constant at $P_{shaft} \approx 75\,\mathrm{kW}$ during cruise, with the propeller spinning at $\Omega_{ICE} \approx 1240 RPM$. The batteries are used to boost power delivery during climb, after which the current drawn is reduced to a minimum, while still ensuring batteries are depleted at the end of the flight. For shorter flights, the median values of the100 km range case are taken as targets. However, values like altitude and engine power settings will vary more as a function of range.

The airspeeds match the best range airspeed for propeller aircraft, given by Equation 6.1[19]. For the Panthera, the analytical solution for the best range airspeed is found to be $v_{R_{max}} = 62\,\mathrm{m\,s^{-1}}$ at maximum take-off mass.

$$v_{R_{max}} = v_{D_{min}} = \sqrt{\frac{2}{\rho}\frac{W}{S}\sqrt{\frac{K}{C_{D_0}}}} \tag{6.1}$$

### 6.1.2 Minimum Flight Time Vs Minimum Fuel Consumption

To get an idea of how much fuel can be saved by following the flight profiles obtained in Section 6.1.1, the results for minimum flight time are examined next. The results are shown in

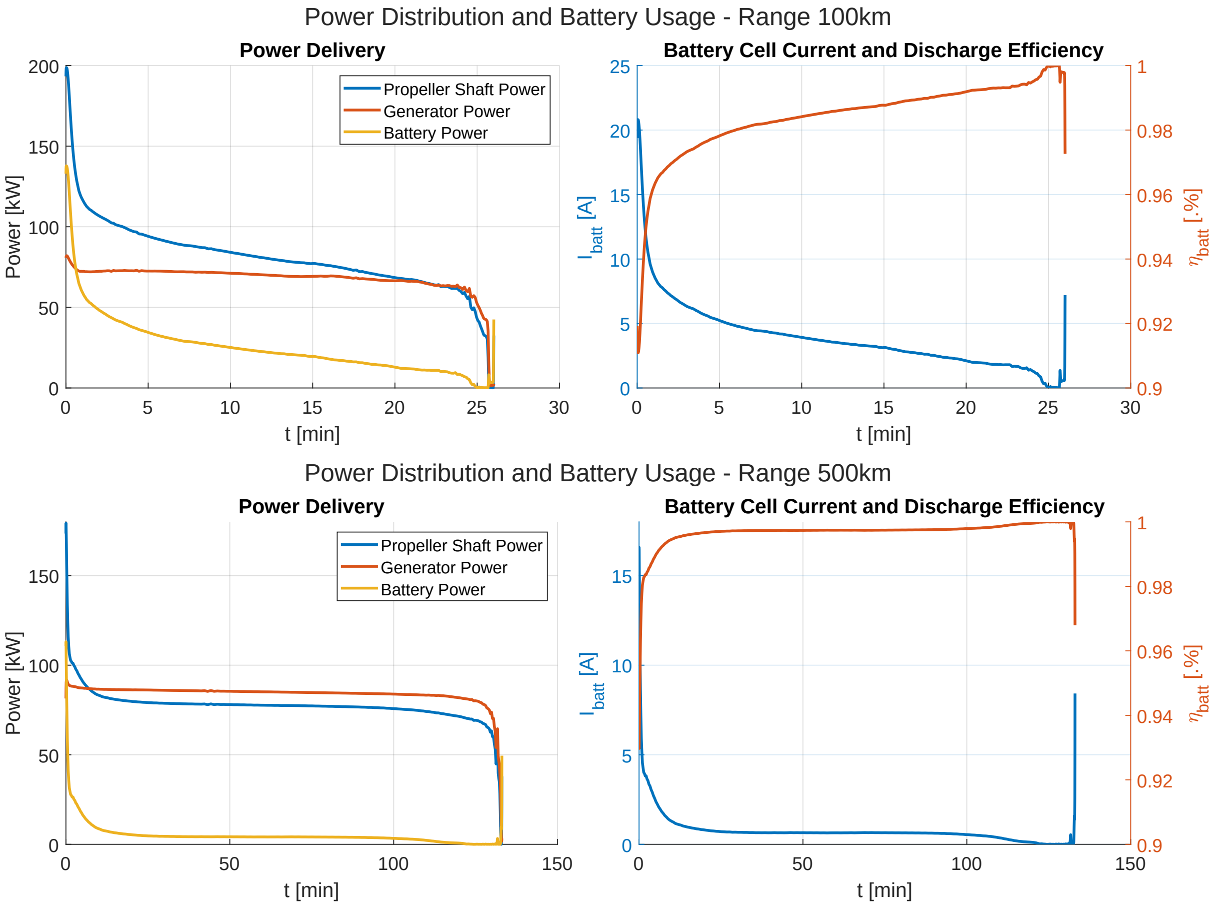

Figure 6.3: Optimal flight path results for minimum fuel consumption, including maximum range, for the Hybrid Panthera.

Table 6.1: Median and target parameter values for fuel-optimal flight with the Panthera

| Range [km] | $h$ [m] | $v_{IAS}$ [m s$^{-1}$] | $P_{shaft}$ [kW] | $\Omega_{prop}$ [min$^{-1}$] | $\Omega_{ICE}$ [min$^{-1}$] | $I_{bat}$ [A] |
|---|---|---|---|---|---|---|
| 100 | 493 | 63.4 | 79.1 | 1274 | 4294 | 3.5 |
| 300 | 660 | 61.3 | 78.4 | 1274 | 4747 | 1.1 |
| 500 | 669 | 60.9 | 77.5 | 1261 | 4819 | 0.6 |
| 1000 | 694 | 60.7 | 75.5 | 1236 | 4820 | 0.3 |
| 1524 | 723 | 60.9 | 73.3 | 1225 | 4763 | 0.2 |
| Weighted avg. | 700 | 60.9 | 75.0 | 1238 | 4787 | 0.5 |

Figure 6.4. The fuel consumption is given in Figure 6.5. To give an idea of the difference in fuel usage between the minimum time and minimum fuel results, the green lines superimpose the values of fuel mass from Figure 6.5.

Figure 6.4 shows that the engine is now run at its maximum power continuously, while the batteries are fully depleted during the climb. The altitude at the top of the climb increases with range, and the maximum altitudes reached are now much higher than for the fuel-optimal flights. As a long climb requires the batteries to last longer, the discharge rate and airspeed are lower with increasing altitude and range. Once at the top of the climb, a descent is initiated

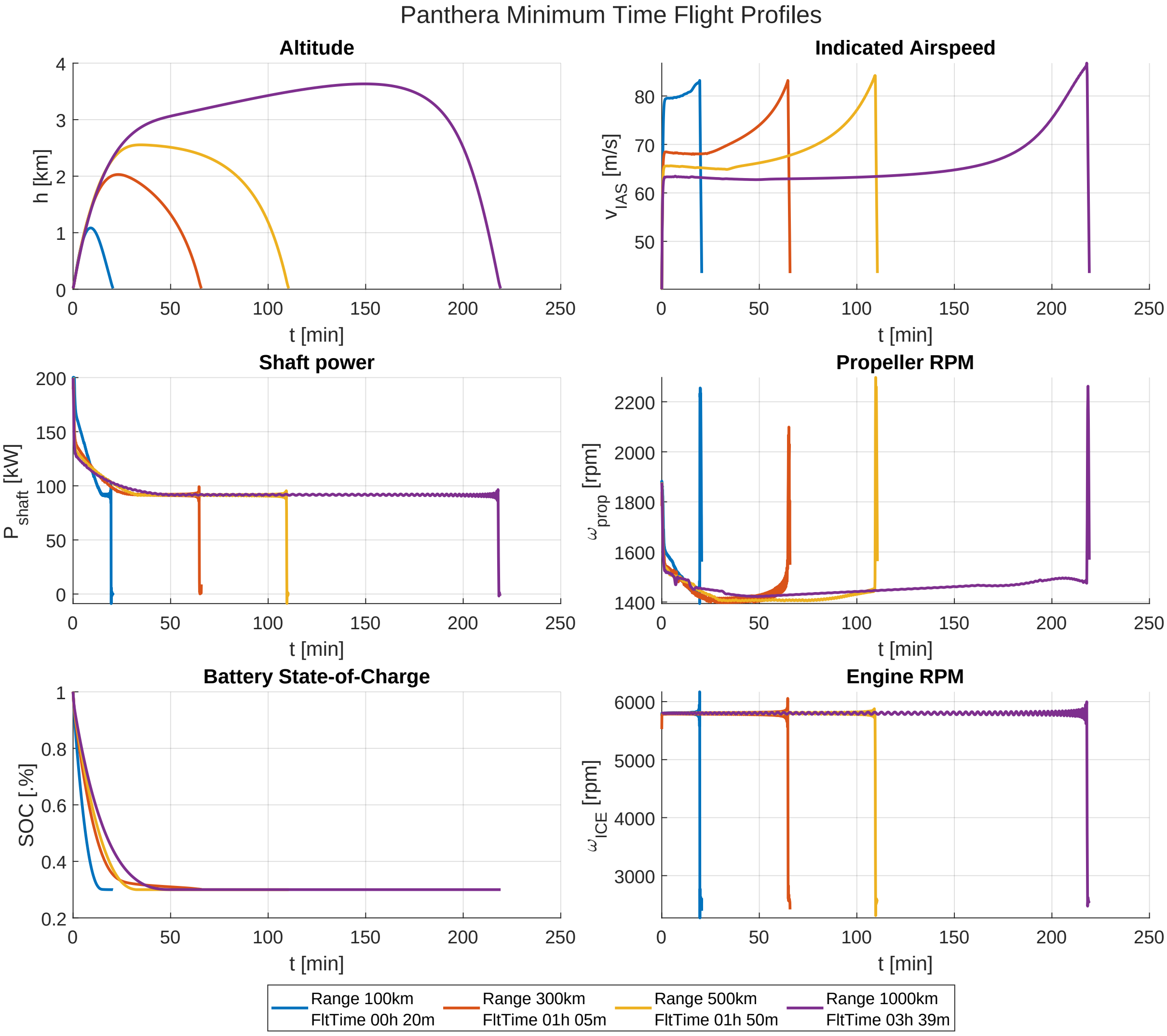

Figure 6.4: Panthera minimum time results.

to pick up airspeed. Only at longer ranges (see the 1000 km case), where starting the descent immediately after the climb is finished would be premature, the climb continues at a reduced climb rate. Propeller shaft power is kept constant at $P_{shaft} = 92\,\mathrm{kW}$ after the initial climb is completed.

The flight times and differences in flight time and fuel consumption are listed in Table 6.2. Again branding the 100 km case as an outlier, taking the weighted averages of the relative differences shows that the time-optimal trajectory reduces flight time by 17.6%, at a cost of 9.7% more fuel burn. For shorter ranges, the amount of power drawn from the batteries is higher, hence the fuel savings when flying a fuel-optimal trajectory increase rapidly with decreasing range. On the other hand, if time is the priority, this extra power from the batteries can be used to increase airspeed. For a range of 100 km, this means that the flight time can be reduced by 23%, but 26.1% more fuel will be burned compared to the fuel-optimal trajectory. Direct comparison plots are provided in Figure G.3 in Appendix G.1.

## 6.2 HY4 Hybrid Fuel Cell Aircraft

Shifting attention to the fuel-cell-powered HY4, Section 6.2.1 again starts with the discussion of the fuel minimization problem. Section 6.2.2 follows with the results for minimum flight time and

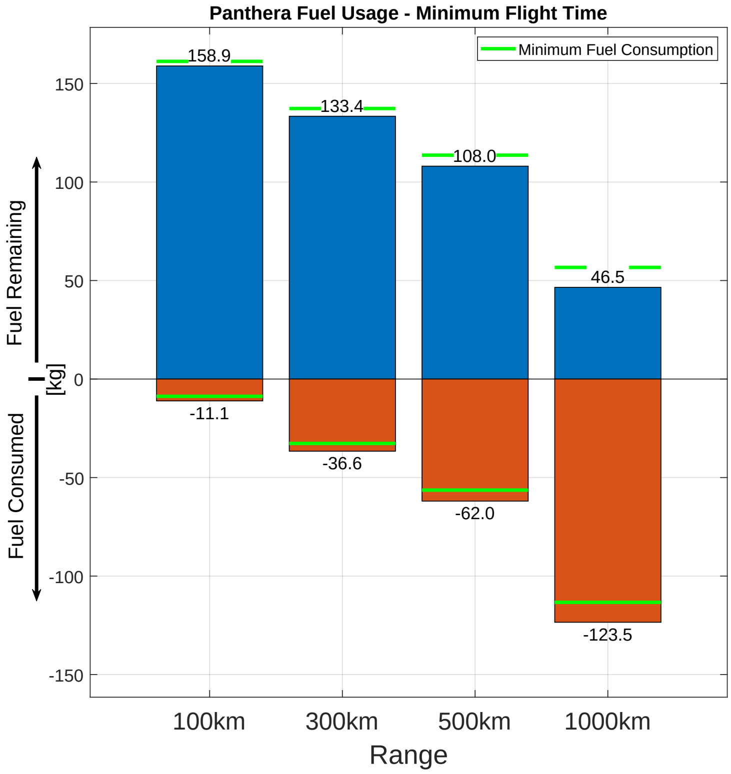

Figure 6.5: Fuel consumption of the Panthera for different ranges when minimizing flight time.

Table 6.2: Difference in flight time and fuel consumption between time- and fuel-optimal trajectories for the Panthera.

| | | Comparison relative to fuel-optimal case | | | |
|---|---|---|---|---|---|
| Range | Flight time | ΔFlight time [h:mm] | ΔFlight time [%] | Δ Fuel burn [kg] | Δ% Fuel burn [%] |
| 100 | 0:20 | 0:06 | -23.1% | +2.3 | +26.1% |
| 300 | 1:05 | 0:14 | -17.7% | +3.9 | +11.9% |
| 500 | 1:50 | 0:23 | -17.3% | +5.6 | +9.9% |
| 1000 | 3:39 | 0:47 | -17.7% | +10.2 | +9.0% |
| Weighted avg. | | | -17.6% | | +9.7% |

how these compare with the trajectories for minimum fuel consumption. It is worth noting that for the HY4, surprisingly, using HS collocation resulted in lower time needed to find a solution. This is likely due to the increased complexity of the problem, as elaborated in Section 6.2.1. The difference between the actual solutions obtained with HS and LGR collocation, however, was negligible. For the sake of consistency, the results shown in this section were the ones obtained using LGR collocation. This could nonetheless be an indication that for problems of higher complexity, it could be beneficial to choose for Hermite-Simpson collocation, even though it is less accurate.

### 6.2.1 Minimizing Fuel Consumption

Obtaining fuel-optimal trajectory solutions for the HY4 is significantly more challenging compared to the Panthera. The main reason for this seems to be the fact that the HY4 is relatively under-powered. If the four fuel cell stacks each have a maximum output power of $P_{FCS} \approx 11\,\mathrm{kW}$ (Figure 3.4), and the batteries deliver $P_{bat} \approx 65\,\mathrm{kW}$ (at full state-of-charge, drawing $I_{bat} \approx 225\,\mathrm{A}$), the ratio of the combined maximum power output of the battery to the maximum take-off mass for the HY4 rounds to $64\,\mathrm{W\,kg^{-1}}$, compared to $225\,\mathrm{W\,kg^{-1}}$ for the Panthera (100 kW from the engine and 195 kW from the batteries). This caused the optimizer to return trajectories where the altitude remains zero, presumably to avoid any scenario where power demand is high, like during a climb. To solve this, and force a climb, an additional integral cost function is added which equals one at every point where the altitude equals zero. The cost decreases quadratically as altitude increases until the cost becomes zero for altitudes equal to or higher than 300 m. The altitude cost function is given in Equation 6.2, which means the total cost function of the problem is now defined by Equation 6.3, where $E_{fuel}$ and $L_\gamma$ were defined previously in Equations 4.6 and 4.16 respectively. The scaling coefficient $c_{alt} = 10^{-3}$ is added to bring down the order of magnitude of the altitude cost and avoids it dominating over the fuel cost. Besides the problem already being more difficult to solve due to the under-powered nature of the HY4, the problem complexity increases further, as there are now three elements in the cost function which the optimizer needs to juggle.

$$L_{alt} = \frac{1}{2}\sqrt{\left[1 - \left(\frac{h(t)^2}{300}\right)\right]^2} + \frac{1}{2}\left[1 - \left(\frac{h(t)}{300}\right)^2\right] \tag{6.2}$$

$$J_{fuel_{HY4}} = E_{fuel} + \int_{t_0}^{t_f} L_\gamma + c_{alt} L_{alt}\, dt \tag{6.3}$$

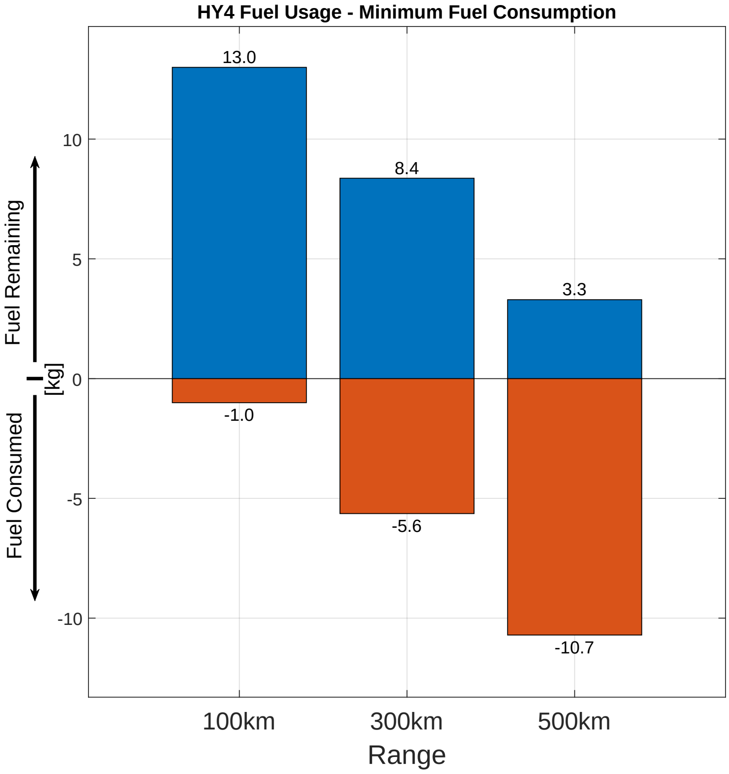

Figure 6.6: Fuel consumption of the HY4 for different ranges.

The solutions are plotted in Figure 6.7, with the fuel consumption presented in Figure 6.6. The general behavior of the functions is very similar to the ones obtained for the Panthera. It can be seen that the current drawn from the fuel cell is approximately constant throughout each of the

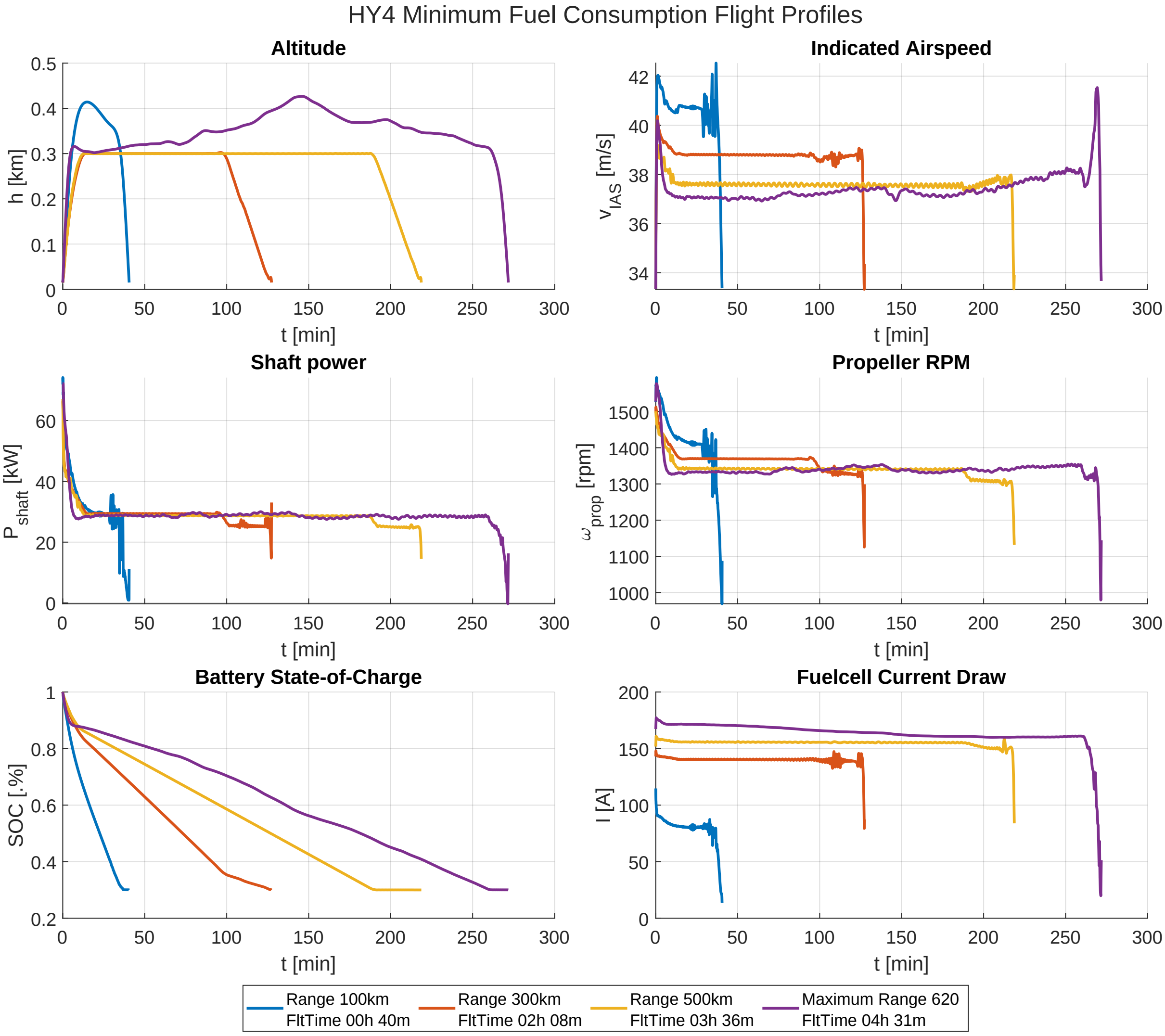

Figure 6.7: Optimal flight path results for minimum fuel consumption, including maximum range, for the HY4.

flights, and changes in shaft power are entirely compensated by the batteries. The shaft power is consistent across the different ranges. Since the contribution of the battery to the total power is less for longer ranges, the fuel cell load is increased to compensate. The higher current draw from the fuel cells, however, is not sufficient to maintain the same airspeed, and both airspeed and propeller RPM are reduced as flight range increases.

### Power Draw Distribution and Battery Utilization

The battery rate of discharge shows similar behavior to what was observed with the solutions for the Panthera, meaning the energy management strategy does not change for the different aircraft. Looking at the power distribution plots in Figure 6.8, the batteries again deliver an initial power boost during the climb, after which priority goes to higher discharge efficiencies, and thus lower current draw. This becomes more noticeable if the range increases. The power delivered by the fuel cell is practically constant throughout the individual flights, and increases with range to compensate for the lower power contributions of the batteries.

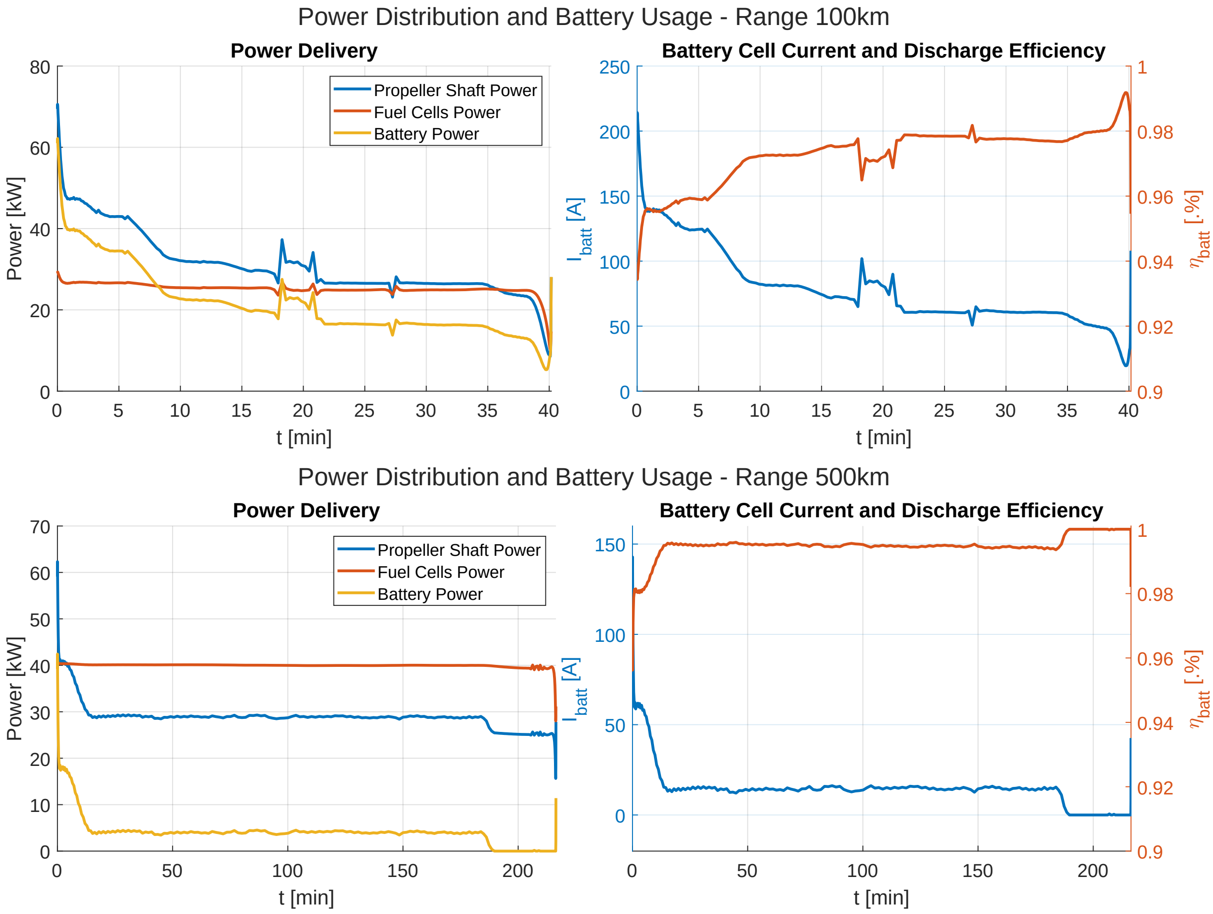

Figure 6.8: Distribution of the power load and battery efficiency for the HY4 for 100 km and 500 km ranges.

### Generalized Parameter Targets

Determining general target values for best fuel economy is not so straightforward in this case, since almost all parameters plotted in Figure 6.7 change with range. Moreover, unlike the Panthera, the HY4 does not have sufficient power to maintain the airspeed for best range, which is $v_{R_{max}} = 43.6\,\mathrm{m\,s^{-1}}$ according to Equation 6.1. Instead, the average airspeed decreases with increasing range.
The one consistency throughout all flight profiles is the shaft power $P_{shaft} \approx 29\,\mathrm{kW}$. The current drawn from the batteries is kept low enough, such that they are discharged at a consistent rate until the start of the descent. To compensate for the lower battery power, the constant power delivered by the fuel cell increases with range.

Nevertheless, the weighted averages of the median values, given in Table 6.3, offer a general target for each of the plotted values to approach fuel-optimal flight without the need to rerun the optimization for every possible range. Since benefits of flying at higher altitudes appear negligible, simply the minimum safe (or practical) altitude can be chosen. In this case 300 m was considered the minimum safe altitude for flight. This is likely due to the limited power available from the hybrid fuel cell powertrain, especially considering the high maximum take-off mass. Climbing to high altitudes would require high electrical loads on the batteries and fuel cells leading to unnecessary energy losses. Additionally, the airframe of the HY4 is made up of two conjoined gliders, which naturally have superior aerodynamic properties compared to classic aircraft of this size. This could result in relatively limited benefits in terms of drag reduction with increasing altitudes.

Table 6.3: Median and target parameter values for fuel-optimal flight with the HY4

| Range<br>[km] | $h$<br>[m] | $v_{IAS}$<br>[$\mathrm{m\,s^{-1}}$] | $P_{shaft}$<br>[kW] | $\Omega_{prop}$<br>[$\mathrm{min^{-1}}$] | $I_{FC}$<br>[$\mathrm{min^{-1}}$] | $I_{bat}$<br>[A] |
|---|---|---|---|---|---|---|
| 100 | 365 | 40.7 | 29.8 | 1416 | 80.9 | 71.7 |
| 300 | 300 | 38.8 | 29.4 | 1369 | 140.4 | 24.9 |
| 500 | 300 | 37.6 | 28.7 | 1341 | 155.5 | 14.2 |
| 620 | 346 | 37.3 | 28.6 | 1337 | 163.8 | 10.2 |
| Weighted avg. | 323 | 37.9 | 28.9 | 1350 | 151.0 | 18.5 |

The average airspeed for fuel-optimal flight, lies around $v \approx 38\,\mathrm{m\,s^{-1}}$. Again, this is less than the analytically determined best airspeed, likely due to a lack of available power. The shaft power and propeller RPM to achieve this airspeed will be around $P_{shaft} \approx 29\,\mathrm{kW}$ and $\Omega_{prop} \approx 1350\,\mathrm{min^{-1}}$, respectively. There is no single value that can be used as a target for both the fuel cell and battery current draw, since these values change significantly with range. Generally, beyond the initial climb, battery current should be chosen such that the batteries are depleted when the top of the climb is reached, and fuel cell current draw should then take on the value which ensures the total power demand is met.

### 6.2.2 Minimum Flight Time Vs Minimum Fuel Consumption

To get an appreciation for the amount of fuel which can be saved with the trajectories obtained in Section 6.2.1, they are combined again to their minimum flight time counterparts. In this case, the extra integral cost for altitude, Equation 6.2, is no longer required, and the cost function equals the one given by Equation 4.17. The solution functions are plotted in Figure 6.9, and the fuel mass values are given in Figure 6.10, again with the fuel mass values from the fuel-optimal solutions superimposed for visual comparison.

Table 6.4: Difference in flight time and fuel consumption between time- and fuel-optimal trajectories for the Panthera

| | | Comparison with fuel-optimal case | | | |
|---|---|---|---|---|---|
| Range | Flight time | ΔFlight time [h:mm] | ΔFlight time [%] | Δ Fuel burn [kg] | Δ% Fuel burn [%] |
| 100 | 0:31 | -0:09 | -22.5% | +0.9 | +90.0% |
| 300 | 1:52 | -0:16 | -12.5% | +1.2 | +21.4% |
| 500 | 3:18 | -0:18 | -8.3% | +1.4 | +13.8% |
| Weighted avg. | | | -11.3% | | +24.8% |

As expected, the fuel cells are now run at maximum output power, similarly to what was observed with the engine in the Panthera. Batteries are mostly used to boost climb power. Specifically, the batteries are almost completely discharged during climb for ranges 100 km and 300 km. For longer ranges, like the 500 km case, the batteries are discharged about 30% during climb, and the rest is used to provide a small increase in available power during the remainder of the flight. This also results in a lower achieved altitude, with more emphasis on a long powered descent. Surprisingly, the airspeeds remain constant for the 300 km and 500 km cases, rather

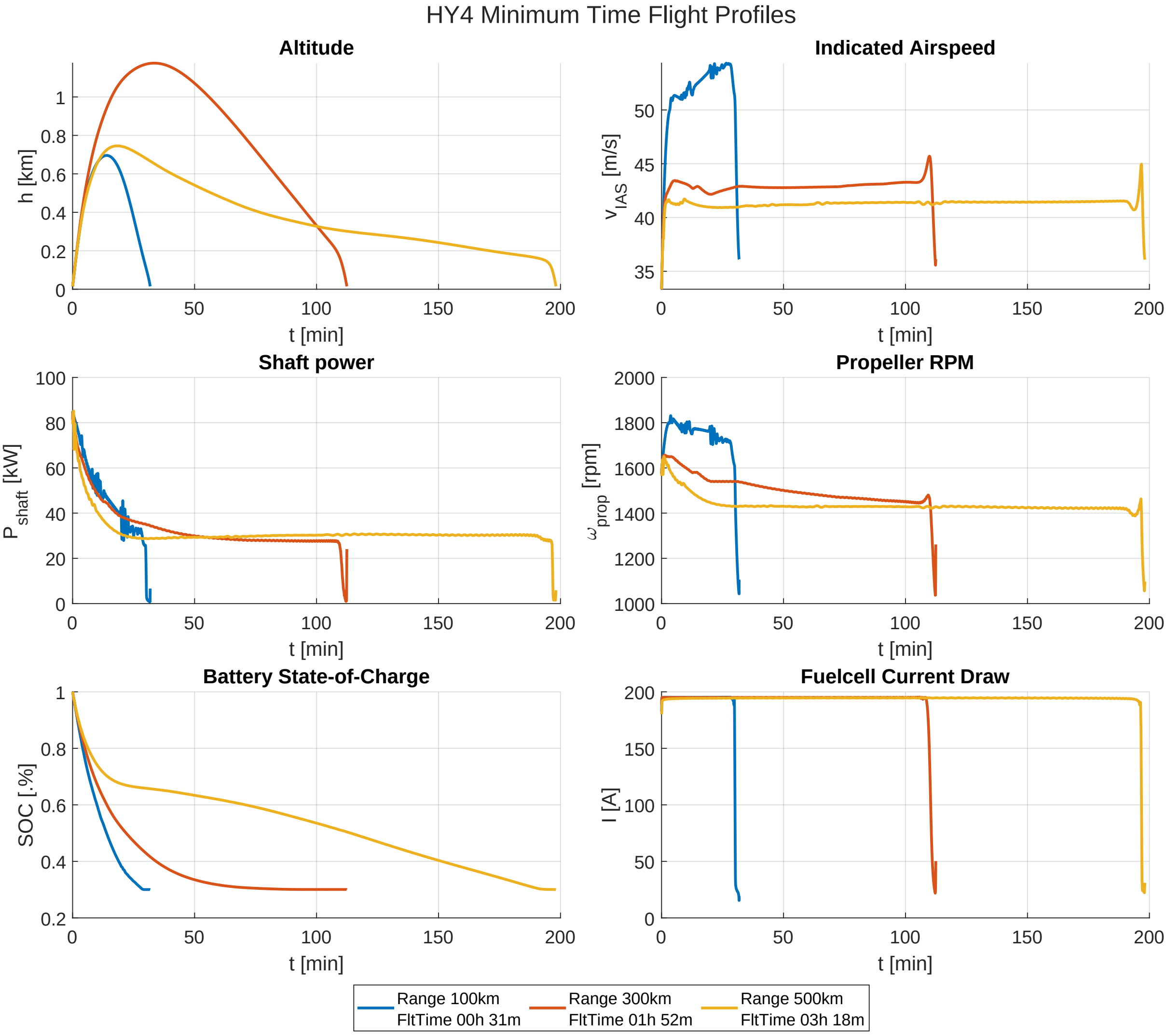

Figure 6.9: Panthera minimum time results.

than picking up during the descent as was seen with the Panthera. This can again be attributed to the lack of power available for the HY4, and the fact that less battery power is available. This is supported by the 100 km range flight data. In that case, the batteries have enough energy left, which can be used in a shorter period of time during the descent, leading to more available power and thus higher airspeeds.

The differences in fuel and flight times are listed in Table 6.4. Again, the numbers show that the benefits in terms of both flight time and fuel consumption are higher for shorter ranges, where more battery power is available. For shorter ranges, the fuel consumption in particular can be reduced by almost half when switching from a minimum time trajectory to a trajectory for minimum fuel consumption.

Compared to the values obtained for the Panthera, the differences in flight time are slightly lower for the HY4, with an average of 11.3% shorter flight times. This can again be attributed to the lower available power. Fuel savings, on the other hand, especially for low ranges, are significantly higher for the HY4, thanks to the larger capacity of its batteries (21 kW h compared to 7.7 kW h for the Panthera). Figure G.11 (Appendix G.2) plots both the fuel- and time-optimal trajectories for ranges of 100 km and 500 km, emphasising the different altitude profiles and battery usage.

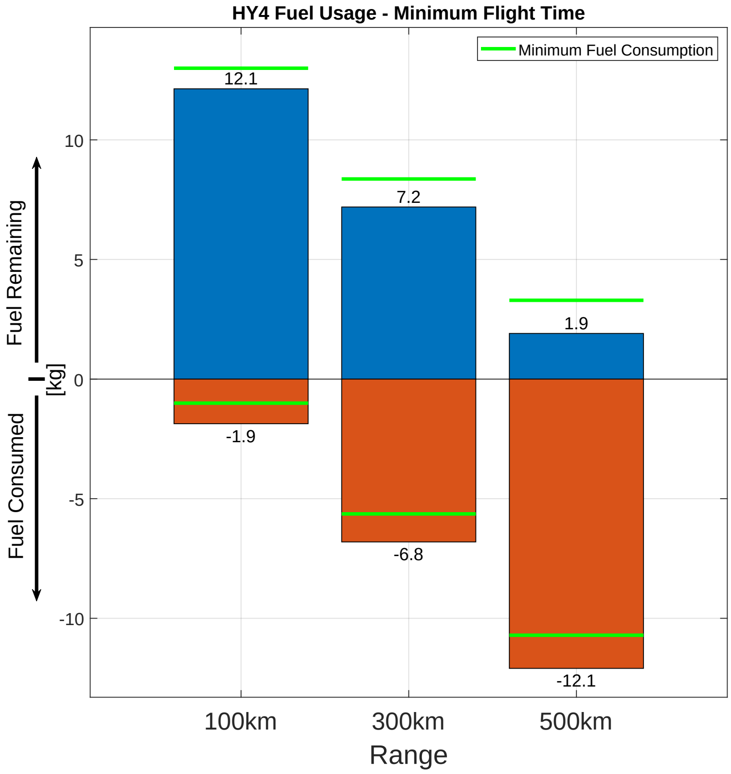

Figure 6.10: Fuel consumption of the HY4 for different ranges.

## 6.3 Legendre-Gauss-Radau Vs Hermite-Simpson

For the single phase case, a brief comparison will be made between the solutions obtained using Hermite-Simpson and Legendre-Gauss-Radau collocation. The minimum time case will be used for the comparison, as it is easier to obtain consistent results than with the more complex fuel minimization problem. However, the same observations are made for the minimum fuel case, the only difference being more variety in the altitude profiles. Solutions obtained using both transcription algorithms are plotted in Figures 6.11 and 6.12. The plots indicate only minimal difference between the obtained trajectories. The objective value, flight time in this case, is practically identical between both methods. However, the run time required to obtain a solution, reported in the legend and summarized in Table 6.5, varies significantly. For the Panthera's case, which was already established as a simpler problem, LGR collocation generally finds a solution in less than half the time. This is expected, as LGR is supposed to be the more efficient method. Looking at the HY4 case, however, the opposite is true. Since the HY4 is pushed to its performance limits, the problem is more complex. Using the less efficient, but also less complex, Hermite-Simpson collocation for this case results in solution obtained in a third of the time (depending on the range and problem size). This shows that going for the most efficient method might not be the best course of action. For complex problems, the added complexity of the LGR algorithm could hinder the optimizer in finding a solution.

## 6.4 MultiPhase Problems

Unfortunately, the multiphase problem failed to yield solutions when using either LGR collocation. Therefore, the switch is made to HS collocation for the solutions discussed in this section. The reason for this is unknown at the time of writing, but considering that there were no problems when using HS collocation, it is possible that a software issue in ICLOCS is preventing the use of orthogonal collocation for multiphase problems. Since HS collocation uses local inter-

Table 6.5: Run time, formatted as h:mm, to find a solution for the minimum flight time problem

| Aircraft | Coll. method | Range case<br>100km | <br>300km | <br>500km | <br>1000km |
|---|---|---|---|---|---|
| Panthera | HS | 0:05 | 0:09 | 0:06 | 0.:05 |
| | LGR | 0:02 | 0:03 | 0:03 | 0:03 |
| HY4 | HS | 0:13 | 1:00 | 0:22 | - |
| | LGR | 0:14 | 3:23 | 1:00 | - |

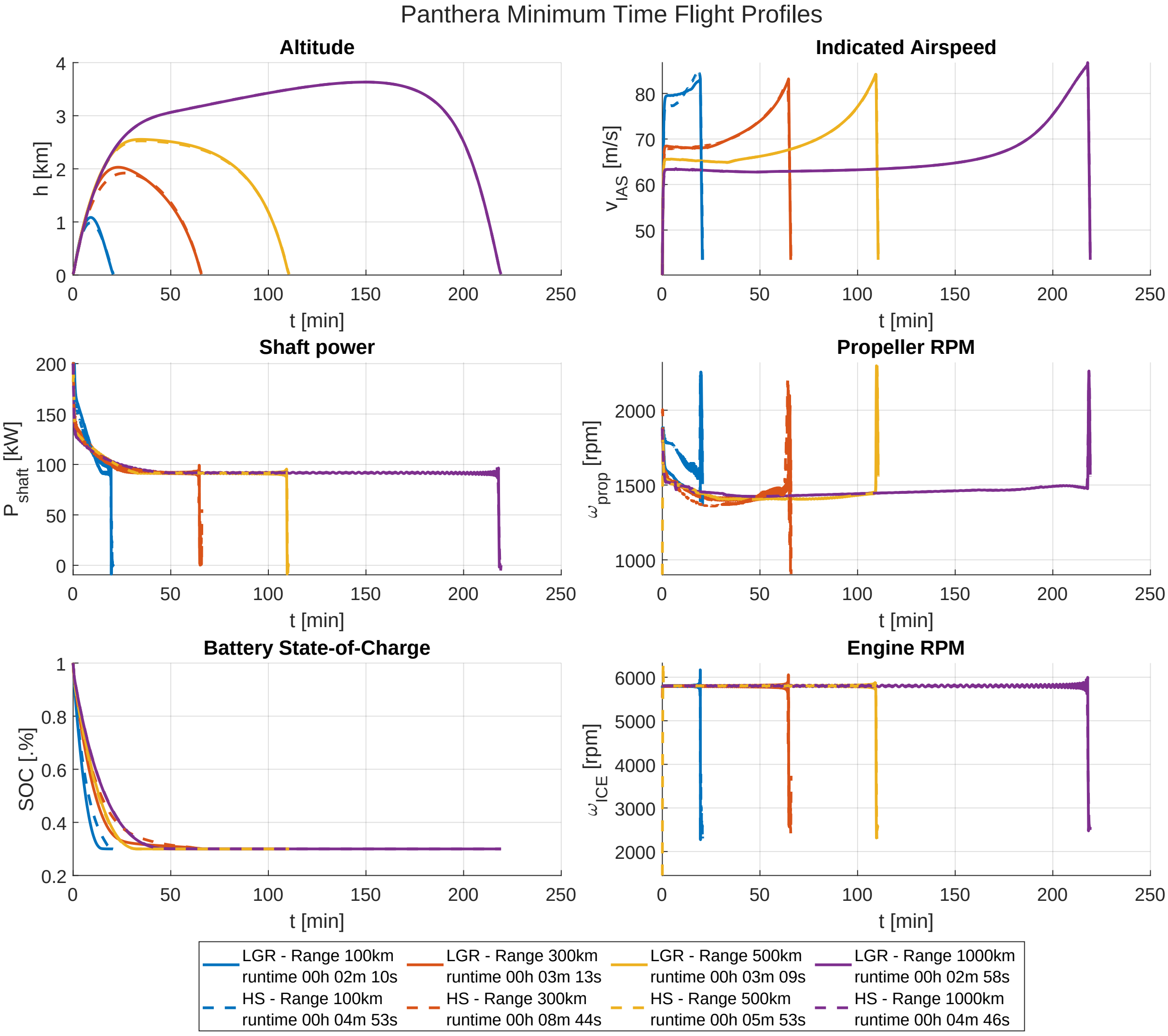

Figure 6.11: Comparison between HS and LGR collocation solutions for the Panthera time minimization problem.

polation, and no derivative constraints are present for the control functions, the default cubic interpolation used by ICLOCS leads to noisy functions for the controls.

The fuel mass consumption values for both the HY4 and Panthera, obtained using the multiphase problem setup, are given in Figure 6.13, including visualization of the fuel used for each flight phase. Comparing the values of total fuel mass used to the ones given in Figures 6.1

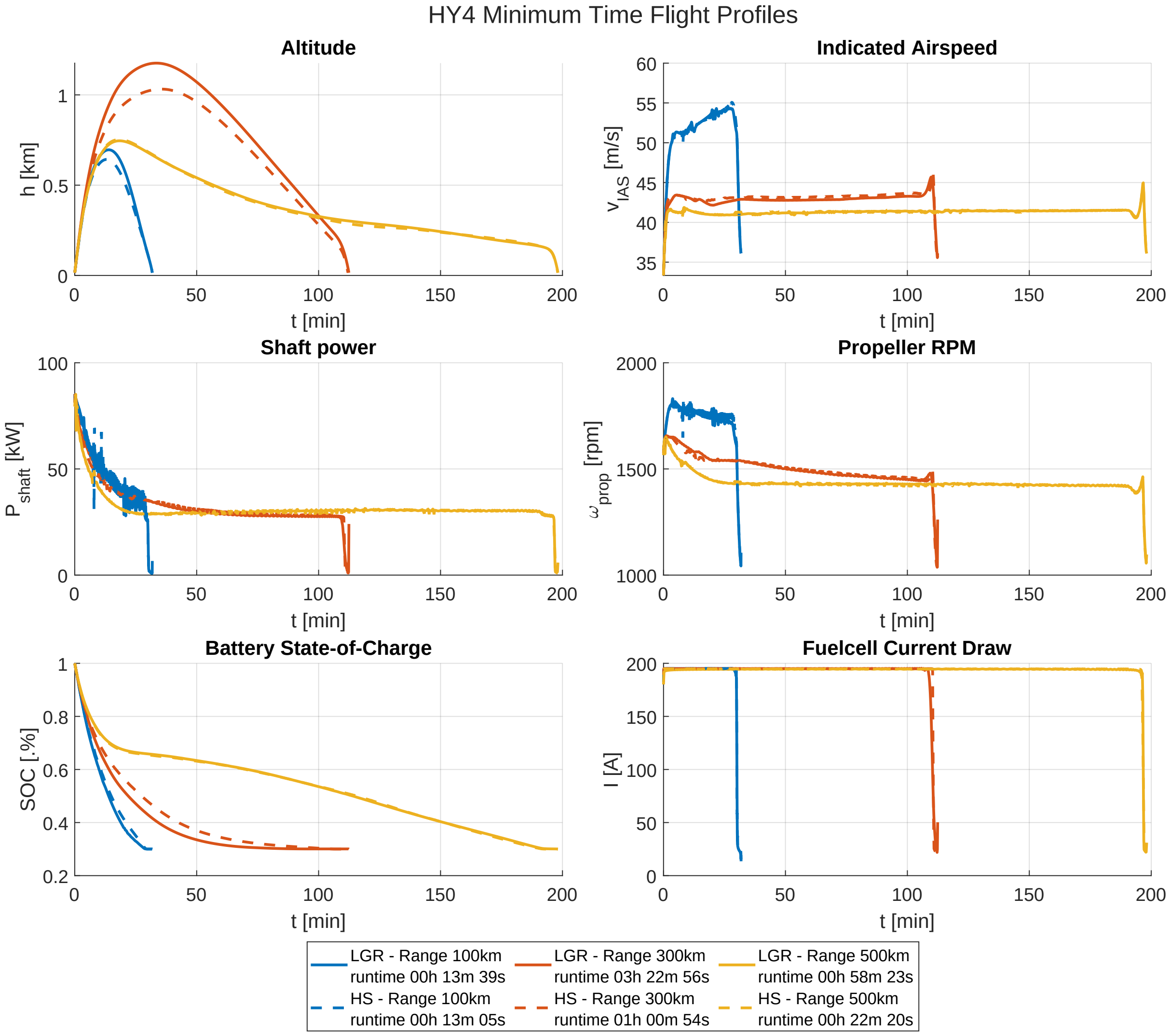

Figure 6.12: Comparison between HS and LGR collocation solutions for the HY4 time minimization problem.

and 6.6 it can be seen that the difference is only in the order of a couple of hundred grams for both aircraft. However, comparing the trajectories for the HY4 in particular, shown in Figure 6.14 for a range of 500 km, the altitude profile in different significantly. It is important to keep in mind that for the multiphase problem, there was no altitude cost needed to force a climb with the HY4, yet the cruise altitudes are higher than the minimum required cruise altitude of $h_{cruise_{min}} = 300\,\mathrm{m}$. Most other parameter functions are similar between the single and multiphase solutions, with the minor exception of the discharge rate which accounts for the difference in power draw during the climb and descent phases due to the different altitude profiles. As range increases, the differences between single and multiphase solutions become smaller. Additional plots comparing single and multiphase solutions are provided in Appendix G.2.1.

It is worth noting that for the 500 km range case, if the minimum climb rate bound $\dot{h}_{min} \geq 0.1\,\mathrm{m\,s^{-1}}$ was not applied, the multiphase solution for the fuel-optimal trajectory for the HY4 again showed reluctance to climb, with the aircraft leveling off as soon as the initial climb phase was completed. The altitude would then remain constant during the climb phase until the last moment, where a steep climb was performed to 300 m to satisfy the final boundary condition for the climb phase. Similar behavior was observed for the descent phase if no constraint for minimum descent rate was present. This lead to a higher total fuel consumption compared to

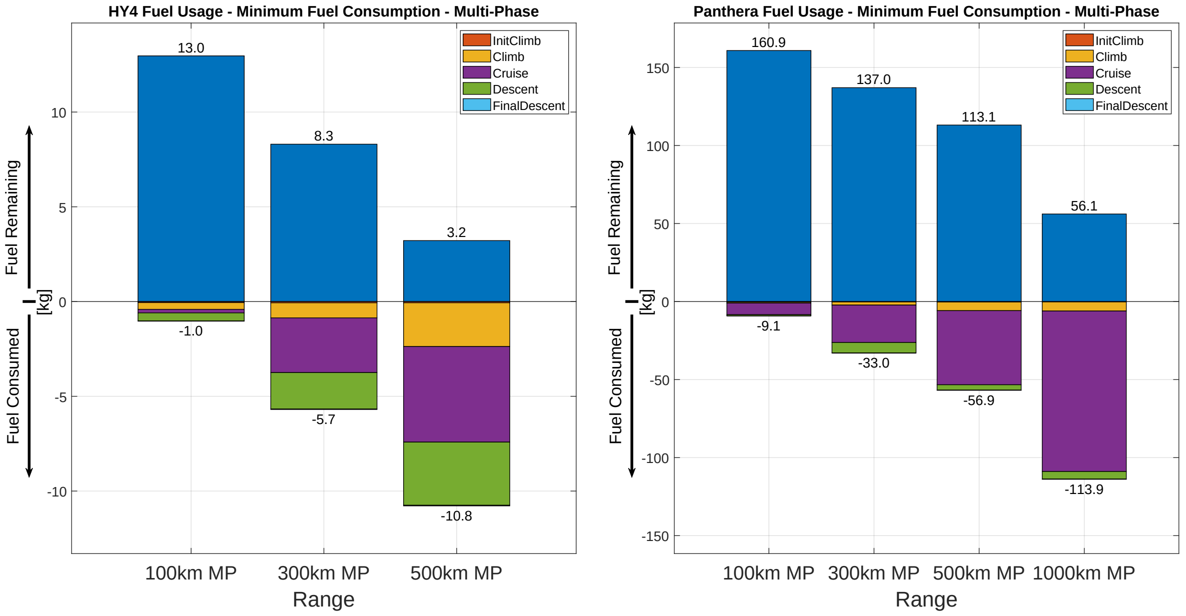

(a) Fuel consumption of the HY4 for different ranges.

(b) Fuel consumption of the Panthera for different ranges.

Figure 6.13: Fuel mass consumption of the HY4 and Panthera for trajectories obtained using the multiphase problem setup.

the trajectories shown with the minimum climb rate constraint applied, indicating a potential local minimum.

Comparing the solutions for the Panthera, plotted in Figure 6.15 for a range of 500 km, shows that the difference between the two problem definition approaches is minimal. Similar comparison plots are provided for more range cases in Appendix G.1.1. However, the difference between the two is more noticeable for short ranges. From Section 6.1.1 it is known that at shorter ranges, the batteries have the largest contributions to the total power and energy. This explains why the altitude profile in Figure G.4 in particular is so different. The multiphase problem has a strict climb requirement where the first phase must be completed in as short of a distance as possible, while the single phase problem has no such requirement. The climb is therefore steeper in the multiphase solution, requiring more power. As higher power draw increases energy losses, the optimizer compensates by reducing the total length of the climb and, with it, the final altitude reached. This is reflected in the other parameter functions too. While the battery discharge rate is more or less equal during the first phase, the engine power setting is higher to allow for the steeper climb of the multiphase solution. Once the climb is completed, discharge rate is lower compared to the single phase solution, since the higher initial fuel consumption must be compensated by lowering the energy losses of the batteries. The single phase solution, on the other hand, ‘wasted’ less energy during the climb, and can therefore afford slightly higher discharge rates without compromising too much on the total fuel consumption. Additionally, the more gradual climb results in a slightly higher airspeed, which in turn leads to a lower total flight time for the single phase solution.

When range increases, the differences between the single and multiphase solutions become smaller. The only notable difference remains the discharge rate, which accounts for the steeper climbs. For the Panthera, the differences in discharge rates become more prominent with increasing range, as the larger contributions to power of the batteries during climb, require lower discharge rates during the longer cruise phases to compensate. While only the solutions for 100 km and 500 km ranges are plotted, the differences between single- and mutli-phase solutions

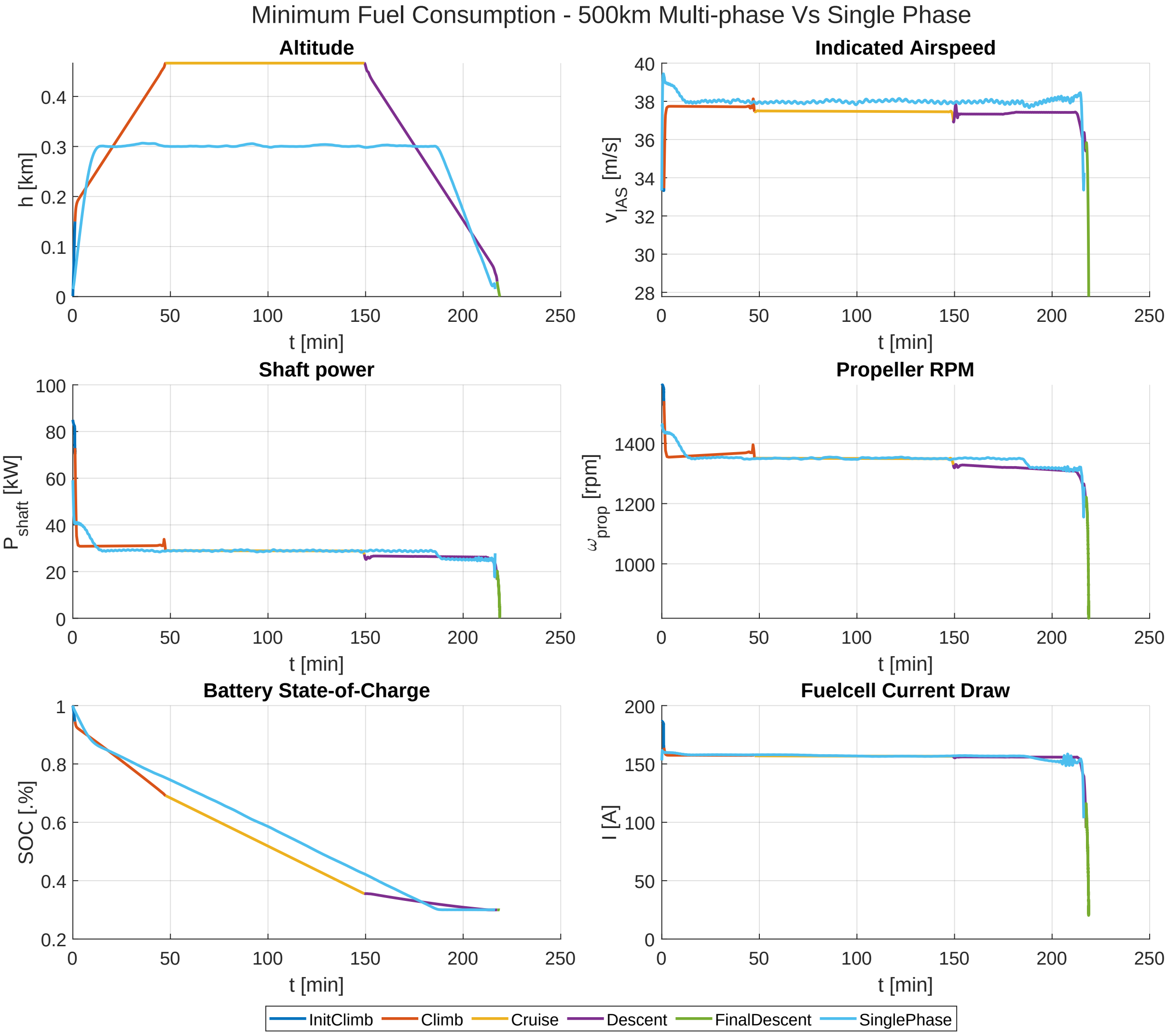

Figure 6.14: Fuel consumption of the HY4 500km multiphase.

are consistent for all ranges.

Comparing the solutions for maximum range shows that the difference in the final range values between single and multiphase solutions are again negligible compared to the magnitude of their values. For the HY4, the multiphase problem yields a maximum range which is 13 km, or 2%, lower than the single phase solution. Likewise, for the Panthera the maximum range is 17 km or 1% lower. Plots are again available in Appendices G.1.1 and G.2.1.

Finally, the biggest downside of the multiphase problem setup is the time required to find a solution. Instead of a single large problem, each phase is its own subproblem which must be solved. The runtimes are listed in Table 6.6. For the case of the Panthera, the multiphase problem can take more than ten times as long to yield a solution, compared to its singlephase equivalent. However, similar to what was observed when comparing LGR and HS collocation, the same is not always true for the case of the HY4. This is likely due to the additional altitude cost, Equation 6.2, no longer being required to force a climb, as the altitude boundary conditions and minimum climb rate bounds applied to the climb phases already take care of this. Since the main goal of this work is to identify optimal energy management, single phase generally seems like the better option, but clealy the m

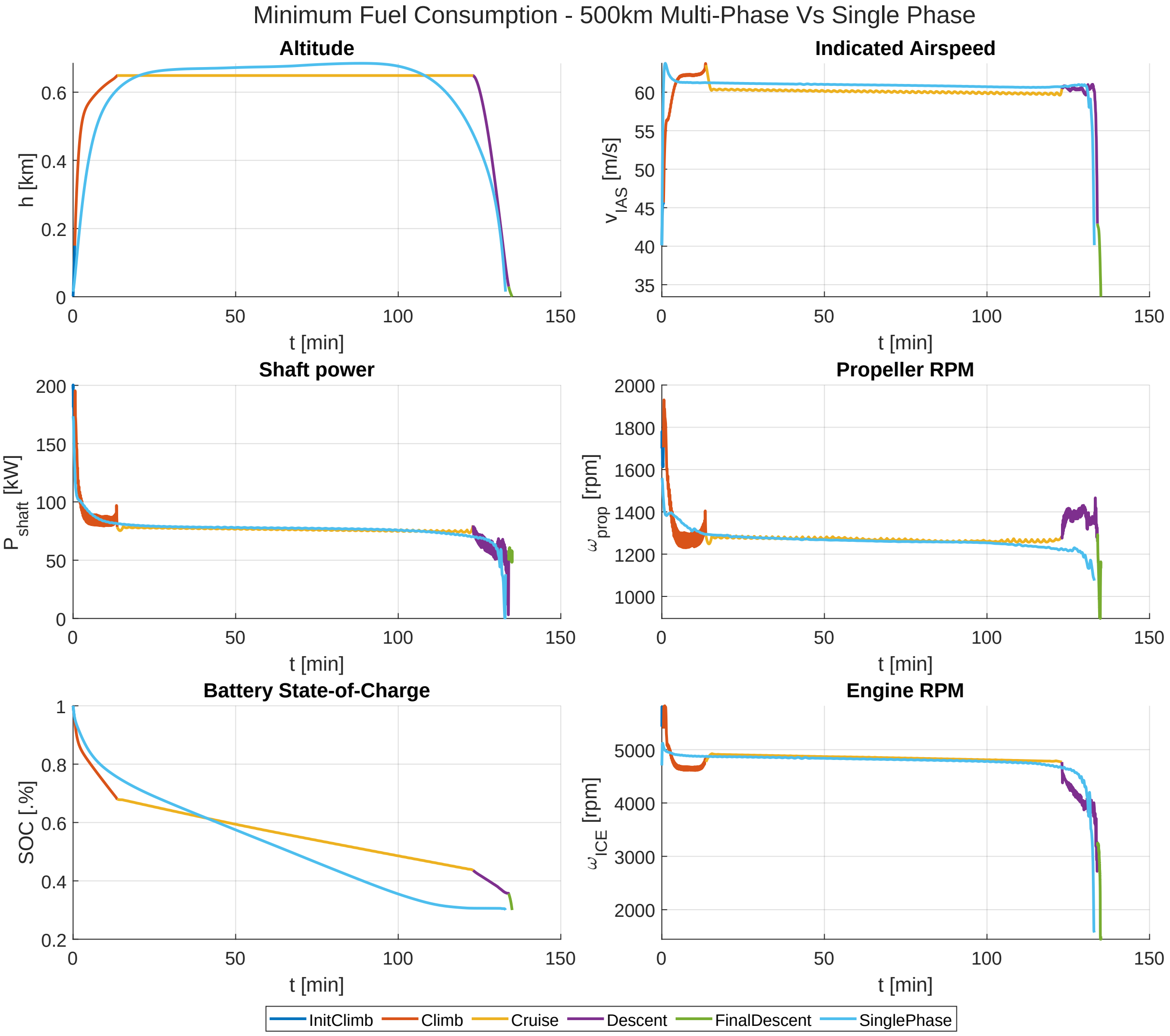

Figure 6.15: Fuel consumption of the panthera 500km multiphase.

Table 6.6: Run time, formatted as h:mm, to find a solution for the minimum fuel problem

| | | Range case | | | |
|---|---|---|---|---|---|
| Aircraft | Coll. method | 100km | 300km | 500km | 1000km |
| Panthera | SP | 0:02 | 0:03 | 0:03 | 0.:03 |
| | MP | 0:22 | 0:48 | 0:17 | 0:47 |
| HY4 | SP | 0:14 | 3:23 | 1:00 | - |
| | MP | 0:26 | 2:45 | 0:56 | - |

This page is intentionally left blank.

# 7 Conclusions

The overall energy management strategy for best fuel economy is similar for both aircraft covered, even though they have different powertrain configurations and aerodynamic characteristics. The power source which consumes fuel, be it a fuel cell or a combustion engine, is run at an approximately constant power output corresponding to the power required during the cruise section of the flight. Additional power required during take-off and climb is provided by the batteries. Once the climb is completed, electrical load on the batteries reduces, such that the constant discharge rate is at its minimal value which still fully depletes the cells by the time the descent starts. This slow continuous discharge ensures maximal discharge efficiency while still using the battery's full capacity.

For complex problems with a clear solution, such as the minimum fuel case for the Panthera, LGR collocation yields both better results with lower objective values and does so in a fraction of the time compared to HS collocation. The difference in solutions obtained between the two methods reduces when switching to a simpler problem, like time minimization. However, LGR collocation is still faster. If the problem is complex, and has a less obvious solution, such as the fuel-optimal trajectory optimization which pushes the performance limits of the under-powered HY4, it appears the LGR-transcribed problem becomes too complex, and the opposite becomes true. In this, using HS collocation yielded much smoother results, in less than half the run time. For the time minimization problem, solutions became equivalent, but HS collocation was still slightly faster compared to LGR.

Using the single phase problem definition, it is possible to identify general parameter targets such as best airspeed and power settings for best fuel economy. In case of the Panthera, defining these values is straightforward, considering the trajectories are consistent for all ranges. For the HY4, it is possible to identify the best airspeed, but altitude should be kept as low as possible, due to the climb requiring a high power load and causing higher energy losses.

Using a multiphase problem setup can offer more control over the trajectory, but results in a suboptimal solution because of the added constraints and costs. For the Panthera, results were mostly consistent with the single phase solutions, with the exception of the battery discharge rates. Due to the higher power draw during climb, the current draw during the following cruise phase is reduced to compensate for the energy losses during climb. For the HY4, control functions were consistent with the single phase results, and so were the airspeed values. The altitude profile, however, differed significantly, with higher altitudes being reached. Regardless, differences in total fuel consumption were negligible between the two problem definitions. This phenomenon where large differences in altitude profile still had negligible effect on total fuel consumption is something which remained consistent for all cases, indicating a relatively 'flat' objective function. For best fuel economy, flying at a minimum drag airspeed, and keeping a constant power setting, proved more important than the choice of altitude. This was more noticeable for the HY4, with its relatively low power available and good aerodynamic properties following from its glider-based airframe.

Considering the mutliphase problem only yielded results when using Hermite-Simpson collocation, and failed when using LGR collocation, combined with the significantly increased time required to find a solution, leads to the conclusion that unless a certain constrained trajectory is required, it is best to use the single phase setup to obtain general optimal solutions. If, however, a certain trajectory is predefined with known limitations, the single phase problem is less suited, as there are only a limited amount of modification can be made to the constraint and cost functions to force a certain outcome.

## 7.1 Recommendations For future Work

One of the first things which should be done, is performing a new validation as soon as new, error-free flight test data becomes available. This will make it clear if there are sources of error in any of the models used. Additionally, providing more details on the components, will increase the accuracy of the models and any parameter estimations used. The value of the inverter efficiency is a very conservative one, to account for any additional power requirements or unknown components. More data would improve the estimation of these values and improve the solutions. The HY4 especially would benefit from any increase in power or powertrain efficiency, as it is being pushed to its performance limits for the fuel-optimal case. Example plots are provided in Appendix G.2.2 which show how alleviating the load on the fuel cells and batteries improves overall performance.

An additional verification could be performed by comparing the results obtained using ICLOCS to results obtained through a different transcription tool, such as the widely adopted commercial tool GPOPS2 [41]. If solutions are found to be similar, then it might be beneficial to switch to a different optimal control problem solution method entirely, as the collocation methods used for this work appeared to struggle, especially with the HY4 case.

Following the SOLID principles, the code is made to be expanded. Therefore, more component and powertrain models can be added. One example of functionality which can be added is energy recuperation of the propeller. whilst this would introduce a discrete switch in the power delivery, which is generally not ideal in NLPs, combining it with a multiphase problem setup which contains a dedicated energy recuperation phase could mitigate this. Although fuel savings are likely minimal, considering the recuperation phase would be during a descent to land, there is a potential to save on battery charging time.

In a distant future, adding a parameterized aircraft model and having the optimizer look not only for the optimal state and control functions, but also these constant aircraft design parameters, could result in a simulation-based aircraft design tool.

# References

[1] Directorate-General for Mobility & Transport and Directorate-General for Research & Innovation. *Flightpath 2050 - Europe's vision for aviation : maintaining global leadership and serving society's needs.* Publication Office of the European Union, July 2011. URL: `http://ec.europa.eu/transport/sites/transport/files/modes/air/doc/flightpath2050.pdf`.

[2] MAHEPA Consortium. *Concept of Modular Architecture for Hybrid Electric Propulsion of Aircraft.* URL: `https://mahepa.eu/`.

[3] *HY4.* URL: `https://hy4.org`.

[4] Mateo Emanuele Piccio and Alessandro Porrini. "Planning and simulation of the flight test campaign for a hydrogen hybrid electric aircraft". MA thesis. Politecnico Di Milano, 2020.

[5] *DLR - Hy4: Electric flight powered by fuel cell.* URL: `https://dlr.de/content/en/images/2017/4/hy4-electric-flight-powered-by-fuel-cell_28722.html`.

[6] *Pipistrel Vertical Solutions.* URL: `http://pipistrel-aircraft.com/`.

[7] Robert C. Martin. *Clean Architecture: A Craftsman's Guide to Software Structure and Design.* Prentice Hall, 2018. ISBN: 978-0-13-449416-6.

[8] Matthew P. Kelly. *Transcription Methods for Trajectory Optimization: a beginners tutorial.* 2017. arXiv: `1707.00284 [math.OC]`.

[9] Matthew Kelly. "An Introduction to Trajectory Optimization: How to Do Your Own Direct Collocation". In: *SIAM Rev.* 59.4 (Jan. 2017), pp. 849–904. ISSN: 0036-1445. DOI: `10.1137/16M1062569`. URL: `https://doi.org/10.1137/16M1062569`.

[10] Imperial College London. *ICLOCS2 Optimal Control Software.* URL: `http://www.ee.ic.ac.uk/ICLOCS/default.htm`.

[11] Coin-Or. *IPOPT - Interior Point Optimizer.* URL: `https://github.com/coin-or/Ipopt`.

[12] Jeffrey R. Chasnov. *Numerical Methods for Engineers - Coursera Lecture Notes.* The Hong Kong University of Science and Technology - Department of Mathematics. 2020. URL: `https://www.math.hkust.edu.hk/~machas/numerical-methods-for-engineers.pdf`.

[13] Santiago Vera Rendon. "Trajectory planning based on collocation methods for multiple aerial and ground autonomous vehicles". PhD thesis. Universidad de Sevilla - Escuela Técnica Superior de Ingeniería, 2015.

[14] Divya Garg. "Advances in Global Pseudospectral Methods for Optimal Control". PhD thesis. University of Florida, 2011.

[15] Sander Hartjes. "An Optimal Control Approach to Helicopter Noise and Emissions Abatement Terminal Procedures". PhD thesis. Delft University of Technology, 2015. ISBN: 978-94-6295-100-6. DOI: `https://doi.org/10.4233/uuid:ca4b93ac-6a39-4c89-8699-e0a351e7fe2f`.

[16] Francesco Topputo and Chen Zhang. "Survey of Direct Transcription for Low-Thrust Space Trajectory Optimization with Applications". In: *Abstract and Applied Analysis* 2014 (June 2014), pp. 1–15. DOI: `10.1155/2014/851720`.

[17] Geoffrey T. Huntington and Anil V. Rao. “A Comparison between Global and Local Orthogonal Collocation Methods for Solving Optimal Control Problems”. In: *2007 American Control Conference*. Vol. 31. 2007, pp. 1950–1957. DOI: `10.1109/ACC.2007.4282393`.

[18] Divya Garg et al. “Direct Trajectory Optimization and Costate Estimation of General Optimal Control Problems Using a Radau Pseudospectral Method”. In: *Computational Optimization and Applications* 49 (June 2011), pp. 335–358. DOI: `10.1007/s10589-009-9291-0`.

[19] Snorri Gudmundsson, ed. *General Aviation Aircraft Design*. Butterworth-Heinemann, 2014. ISBN: 978-0-12-397308-5. DOI: `https://doi.org/10.1016/C2011-0-06824-2`. URL: `https://www.sciencedirect.com/book/9780123973085/general-aviation-aircraft-design`.

[20] Ausilio Bauen et al. *Fuel cell technology handbook*. Ed. by GregorEditor Hoogers. Handbook Series for Mechanical Engineering. CRC Press, 2003. ISBN: 0849308771.

[21] National Energy Technology Laboratory for the U.S. Department of Energy. *Fuel Cell Handbook*. 7th edition. University Press of the Pacific, 2005. ISBN: 1410219607,9781410219602.

[22] Toyota. URL: `https://media.toyota.co.uk/wp-content/files_mf/1444919532151015MToyotaMiraiTechSpecFinal.pdf`.

[23] *2019 Honda Clarity Fuel Cell Specifications & Features*. July 2019. URL: `http://hondanews.com/en-US/honda-automobiles/releases/release-0748feefcc68437a94892c160e085aa7-2019-clarity-fuel-cell-specifications-features`.

[24] James Larminie and Andrew Dicks. *Feul Cell Systems Explained*. 2nd ed. John Wiley, 2003. ISBN: 047084857X.

[25] Colleen Spiegel. *PEM Fuel Cell Modeling and Simulation Using Matlab*. Elsevier Science, 2008.

[26] Frano Barbir. *PEM fuel cells: theory and practice*. 2nd ed. Elsevier/Academic Press, 2013. ISBN: 978-0-12-387710-9.

[27] F. Gao et al. “PEM Fuel Cell Stack Modeling for Real-Time Emulation in Hardware-in-the-Loop Applications”. In: *IEEE Transactions on Energy Conversion* 26.1 (2011), pp. 184–194. DOI: `10.1109/TEC.2010.2053543`.

[28] F. Barbir and T. Gómez. “Efficiency and economics of proton exchange membrane (PEM) fuel cells”. In: *International Journal of Hydrogen Energy* 22.10 (1997), pp. 1027–1037. ISSN: 0360-3199. DOI: `https://doi.org/10.1016/S0360-3199(96)00175-9`. URL: `http://www.sciencedirect.com/science/article/pii/S0360319996001759`.

[29] K. Priya, K. Sathishkumar, and N. Rajasekar. “A comprehensive review on parameter estimation techniques for Proton Exchange Membrane fuel cell modelling”. In: *Renewable and Sustainable Energy Reviews* 93 (2018), pp. 121–144. ISSN: 1364-0321. DOI: `https://doi.org/10.1016/j.rser.2018.05.017`. URL: `http://www.sciencedirect.com/science/article/pii/S1364032118303642`.

[30] S.O. Mert, I. Dincer, and Z. Ozcelik. “Performance investigation of a transportation PEM fuel cell system”. In: *International Journal of Hydrogen Energy* 37.1 (2012). 11th China Hydrogen Energy Conference, pp. 623–633. ISSN: 0360-3199. DOI: `https://doi.org/10.1016/j.ijhydene.2011.09.021`. URL: `http://www.sciencedirect.com/science/article/pii/S0360319911021008`.

[31] Jay Pukrushpan. "Modeling and Control of Fuel Cell Systems and Fuel Processors". In: (Jan. 2003).

[32] J.C. Amphlett et al. "Performance Modeling of the Ballard Mark IV Solid Polymer Electrolyte Fuel Cell". In: *Journal of the Electrochemical Society* 142.1 (1995).

[33] Jinhao Meng et al. "Overview of Lithium-Ion Battery Modeling Methods for State-of-Charge Estimation in Electrical Vehicles". In: *Applied Sciences* 8.5 (Apr. 2018), p. 659. ISSN: 2076-3417. DOI: `10.3390/app8050659`. URL: `http:%20//dx.doi.org/10.3390/app8050659`.

[34] Abbas Fotouhi et al. "A review on electric vehicle battery modelling: From Lithium-ion toward Lithium–Sulphur". In: *Renewable and Sustainable Energy Reviews* 56 (2016), pp. 1008–1021. ISSN: 1364-0321. DOI: `https://doi.org/10.1016/j.rser.2015.12.009`. URL: `http://www.sciencedirect.com/science/article/pii/S1364032115013921`.

[35] John G. Hayes and Gordon A. Goodarzi. *Electric powertrain: energy systems, power electronics and drives for hybrid, electric and fuel cell vehicles.* Wiley, 2018.

[36] Min Chen and G. A. Rincon-Mora. "Accurate electrical battery model capable of predicting runtime and I-V performance". In: *IEEE Transactions on Energy Conversion* 21.2 (2006), pp. 504–511. DOI: `10.1109/TEC.2006.874229`.

[37] Rotax Aircraft Engines. *Operators Manual for Rotax Engine type 915 i A series.* PDF. 2017.

[38] M. Ahmad. *High Performance AC Drives.* 2010. DOI: `https://doi.org/10.1007/978-3-642-13150-9_2`.

[39] Quentin R. Wald. "The aerodynamics of propellers". In: *Progress in Aerospace Sciences* 42.2 (2006), pp. 85–128. ISSN: 0376-0421. DOI: `https://doi.org/10.1016/j.paerosci.2006.04.001`. URL: `http://www.sciencedirect.com/science/article/pii/S0376042106000455`.

[40] Ger J.J. Ruijgrok. *Elements of airplane performance.* 2nd ed. Delft Academic Press, 2009. ISBN: 978-90-6562-203-7.

[41] Michael A. Patterson and Anil V. Rao. "GPOPS-II: A MATLAB Software for Solving Multiple-Phase Optimal Control Problems Using Hp-Adaptive Gaussian Quadrature Collocation Methods and Sparse Nonlinear Programming". In: *ACM Trans. Math. Softw.* 41.1 (2014). ISSN: 0098-3500. DOI: `10.1145/2558904`. URL: `https://www.gpops2.com/`.

[42] Thibault Clar. *A strategy for the optimal flight control of a hybrid electric powered aircraft via a Multi-Phase Pseudo-Spectral Method.* Delft University of Technology, Feb. 2019.

[43] Joris Stolwijk. "A Hybrid Optimal Control Approach to Multi-Aircraft Formation Flying". MA thesis. Delft University of Technology, 2017.

[44] S. Hartjes, Marco H. van Hellenberg, and H. G. Visser. "Multiple-phase trajectory optimization for formation flight in civil aviation". In: *CEAS Aeronautical Journal* 10 (2019). DOI: `https://doi.org/10.1007/s13272-018-0329-9`.

This page is intentionally left blank.

# A Aircraft Data

## A.1 HY4 Aircraft and Powertrain Details

Table A.1: HY4 Specifications [4]

| *Parameter* | Symbol | Value | Unit |
|---|---|---|---|
| Service ceiling | $h_{max}$ | 3900 | m |
| **Wing dimensions** | | | |
| Surface area | $S$ | 23.87 | $\mathrm{m}^2$ |
| **Masses** | | | |
| Maximum take-off mass | $m_{TO_{max}}$ | 1715 | kg |
| Maximum fuel mass | $m_{fuel_{max}}$ | 14 | kg |
| **Airspeeds [IAS]** | | | |
| Stall speed | $v_s$ | 27.8 | $\mathrm{m\,s^{-1}}$ |
| Flap stall speed | $v_{s_0}$ | 25.2 | $\mathrm{m\,s^{-1}}$ |
| Maneuver speed | $v_a$ | 45.8 | $\mathrm{m\,s^{-1}}$ |
| Maximum airspeed | $v_{NE}$ | 61.1 | $\mathrm{m\,s^{-1}}$ |
| **Aerodynamic coefficients** | | | |
| Zero-angle-of-attack lift coefficient | $C_{L_0}$ | 0.1111 | - |
| Zero-lift drag coefficient | $C_{D_0}$ | 0.0114 | - |
| Induced drag coefficient | $K$ | 0.0314 | - |
| Cooling drag coefficient | $C_{D_{cooling}}$ | 0.0027 | - |
| Cooling drag factor | $c_{cooling}$ | 0.5 | - |

Table A.2: HY4 Hybrid Fuel Cell Powertrain Specifications [4]

| *Parameter* | Symbol | Value | Unit |
|---|---|---|---|
| **Propeller** | | | |
| Number of blades | $n_{blades}$ | 4 | – |
| Diameter | $D_{prop}$ | 2.02 | m |
| Maximum RPM | $\Omega_{prop_{max}}$ | 2200 | $\mathrm{min}^{-1}$ |
| **Electric motor** | | | |
| Maximum RPM | $\Omega_{EM_{max}}$ | 4000 | $\mathrm{min}^{-1}$ |
| Maximum torque | $\tau_{EM_{max}}$ | 500 | N m |
| Maximum power | $P_{EM_{max}}$ | 200 | kW |
| **Fuel cell** | | | |
| Number of fuel cell stacks | $n_{FCS}$ | 4 | – |
| Number of cells per stack | $n_{FC}$ | 120 | – |
| Membrane area | $A_m$ | 0.006 | $\mathrm{m}^2$ |
| Operating temperature | $T_{oper}$ | 343 | K |
| Blower mass flow | $Q_{bl}$ | 0.025 | $\mathrm{m}^3\,\mathrm{s}^{-1}$ |
| Maximum current | $I_{max}$ | 195 | A |
| Fuel excess ratio | $\Lambda_{H_2}$ | 1.05 | – |
| Air excess ratio | $\Lambda_{air}$ | 1.7 | – |
| **Batteries** | | | |
| Number of cells in series | $n_{series}$ | 76 | – |
| Number of series cell strings in parallel | $n_{parallel}$ | 0 | – |
| Rated cell capacity | $Q_{rated}$ | 75 | A h |
| Rated cell energy | $E_{rated}$ | 277 | W h |
| Maximum state of charge | $SOC_{max}$ | 1.0 | – |
| Minimum state of charge | $SOC_{min}$ | 0.3 | – |
| Rated discharge rate | $C_{rated}$ | 0.2 | – |
| Rated discharge current | $I_{rated}$ | 15 | A |
| Maximum discharge rate | $C_{max}$ | 3 | – |
| Maximum discharge current | $I_{max}$ | 225 | A |
| Maximum cell voltage | $V_{max}$ | 4.2 | V |
| Minimum cell voltage | $V_{min}$ | 2.7 | V |
| Rated cell voltage | $V_{rated}$ | 3.7 | V |

## A.2 Panthera Aircraft and Powertrain Details

Table A.3: Panthera Specifications

| *Parameter* | Symbol | Value | Unit |
|---|---|---|---|
| Service ceiling | $h_{max}$ | 7600 | m |
| **Wing dimensions** | | | |
| Surface area | $S$ | 11.2 | $\mathrm{m^2}$ |
| **Masses** | | | |
| Maximum take-off mass | $m_{TO_{max}}$ | 1315 | kg |
| Maximum fuel mass | $m_{fuel_{max}}$ | 170 | kg |
| **Airspeeds [IAS]** | | | |
| Stall speed | $v_s$ | 33.4 | $\mathrm{m\,s^{-1}}$ |
| Flap stall speed | $v_{s_0}$ | 30.8 | $\mathrm{m\,s^{-1}}$ |
| Maneuver speed | $v_a$ | 74.6 | $\mathrm{m\,s^{-1}}$ |
| Maximum airspeed | $v_{NE}$ | 113.2 | $\mathrm{m\,s^{-1}}$ |
| **Aerodynamic coefficients** | | | |
| Zero-angle-of-attack lift coefficient | $C_{L_0}$ | 0.3968 | - |
| Zero-lift drag coefficient | $C_{D_0}$ | 0.0208 | - |
| Induced drag coefficient | $K$ | 0.0875 | - |

Table A.4: Panthera Hybrid Electric Powertrain Specifications [42]

| *Parameter* | Symbol | Value | Unit |
|---|---|---|---|
| **Propeller** | | | |
| Number of blades | $n_{blades}$ | 5 | – |
| Diameter | $D_{prop}$ | 1.98 | m |
| Maximum RPM | $\Omega_{prop_{max}}$ | 2250 | $\mathrm{min}^{-1}$ |
| **Electric motor** | | | |
| Maximum RPM | $\Omega_{EM_{max}}$ | 12000 | $\mathrm{min}^{-1}$ |
| Maximum torque | $\tau_{EM_{max}}$ | 120 | N m |
| Maximum power | $P_{EM_{max}}$ | 200 | kW |
| **Engine - Rotax915** | | | |
| Maximum RPM | $\Omega_{ICE_{max}}$ | 5800 | $\mathrm{min}^{-1}$ |
| Idle RPM | $\Omega_{ICE_{idle}}$ | 1450 | $\mathrm{min}^{-1}$ |
| Maximum power | $P_{ICE_{max}}$ | 105 | kW |
| Maximum continuous power | $P_{ICE_{cont}}$ | 99 | kW |
| **Batteries** | | | |
| Number of cells in series | $n_{series}$ | 216 | – |
| Number of series cell strings in parallel | $n_{parallel}$ | 8 | – |
| Rated cell capacity | $Q_{rated}$ | 2.4 | A h |
| Rated cell energy | $E_{rated}$ | 8.8 | W h |
| Maximum state of charge | $SOC_{max}$ | 1.0 | – |
| Minimum state of charge | $SOC_{min}$ | 0.3 | – |
| Rated discharge rate | $C_{rated}$ | 0.4 | – |
| Rated discharge current | $I_{rated}$ | 0.96 | A |
| Maximum discharge rate | $C_{max}$ | 14.5 | – |
| Maximum discharge current | $I_{max}$ | 34.8 | A |
| Maximum cell voltage | $V_{max}$ | 4.2 | V |
| Minimum cell voltage | $V_{min}$ | 2.7 | V |
| Rated cell voltage | $V_{rated}$ | 3.7 | V |

# B Parameter Estimation Results

## B.1 Fuel Cell Parameter Estimation Results

Values of the fuel cell parameters found using parameter estimation with experimental data of the HY4 are given in Table B.1. Initial guesses are those found by Amphlett et al. for the Ballard MkIV fuel cell.

Table B.1: Fuel cell detailed parameter estimation results

| Parameter | Symbol | Unit | Initial value | estimated value |
|---|---|---|---|---|
| Membrane area | $A_m$ | $\mathrm{cm}^2$ | 50 | 61 |
| Membrane resistance | $R_m$ | $\Omega \times \mathrm{m}^2$ | $1.5 \times 10^{-5}$ | $7.5 \times 10^{-6}$ |
| Anode exchange current density | $i_{0_{an}}$ | $\mathrm{A\,cm^{-2}}$ | 50 | 40 |
| Cathode exchange current density | $i_{0_{cat}}$ | $\mathrm{A\,cm^{-2}}$ | $1 \times 10^{-3}$ | $8 \times 10^{-4}$ |
| Anode transfer coefficient | $\alpha_{an}$ | – | 0.5 | 1 |
| Cathode transfer coefficient | $\alpha_{cat}$ | – | 0.25 | 0.30 |
| Limit current density | $i_{lim_{an}}$ | $\mathrm{A\,cm^{-2}}$ | $1.3 \times 10^4$ | $3.8 \times 10^4$ |
| Limit current density | $i_{lim_{cat}}$ | $\mathrm{A\,cm^{-2}}$ | $1.3 \times 10^4$ | $3.8 \times 10^4$ |

## B.2 Battery Parameter Estimation Results

Detailed results of the battery parameter estimation results for the Panthera (Appendix B.2.2), and the HY4 (Appendix B.2.1).

### B.2.1 HY4 Batteries

The values for coefficients $K_1$ through $K_9$, resulting from the parameter estimation for the HY4's KOKAM batteries, and the respective initial guesses, are given in Table B.2. Initial guesses were determined iteratively

Table B.2: Parameter estimation results for the KOKAM battery cells

| Coefficient | Initial value | estimated value |
|---|---|---|
| $K_1$ | 0.1 | 0.0986 |
| $K_2$ | 300 | 292.1653 |
| $K_3$ | 0.1 | 0.1097 |
| $K_4$ | 6.0 | 6.3877 |
| $K_5$ | 15 | 14.6278 |
| $K_6$ | 1.0 | 1.1472 |
| $K_7$ | 0.1 | 0.3473 |
| $K_8$ | -10 | -9.6117 |
| $K_9$ | 0.1 | 0.0935 |

### B.2.2 Panthera Batteries

The values for coefficients $K_1$ through $K_9$, as well as the initial guesses, can be seen in Table B.3. Initial guesses were determined iteratively. The RMSPE values for each of the discharge curves separately are given in Table B.4 for the respective current draw values.

Table B.3: Parameter estimation results for the Samsung battery cells

| Coefficient | Initial value | estimated value |
|---|---|---|
| $K_1$ | 0.1 | 0.0273 |
| $K_2$ | 125 | 124.6630 |
| $K_3$ | 1.0 | 0.7500 |
| $K_4$ | 1.0 | 0.7670 |
| $K_5$ | 10 | 9.1283 |
| $K_6$ | 1.0 | 1.0214 |
| $K_7$ | -0.1 | -0.1206 |
| $K_8$ | -0.1 | -0.1447 |
| $K_9$ | 0.1 | 0.1476 |

Table B.4: RMSPE values for each of the battery discharge curves shown in Figure 3.7

| Current Value [A] | $\varepsilon_{RMSP}$ [%] |
|---|---|
| 1 | 0.89 % |
| 5 | 0.74% |
| 15 | 0.61% |
| 30 | 0.89% |

# C Aircraft Model Class Diagram

The partial class diagrams of the aircraft and both powertrains are shown in Figures C.1 to C.3. These are combined in the complete class diagram of the aircraft model shown in Figure C.4. For ease of use, each aircraft has its own class definition file in which the aircraft's properties are defined, allowing for quick creation of the aircraft object without the need to pass input arguments each time.

Some important clarifications on the notations used:

- All properties have public read or get-access. They can always be called by the user.
- Symbols in front of properties indicate the write permission or set-access:
    - Properties marked with a minus (−) are constant. Their values are set in the class definition file.
    - Octothorps (#) indicate protected properties. These can be set once, by passing their name-value pair to the constructor, after which they become read-only. This ensures property values are not changed accidentally.
    - Properties preceded by a tilde (∼) are dependent and are given a value automatically based on other properties.
    - Properties with both an Octothorp and a tilde (# ∼) are conditionally dependent or optional. They can be set by the user, or become dependent if left blank, in which case they are given a value automatically based on other property values.
- Dependent properties under "handles" are used in the optimal control problem definition to ensure the correct component objects are referenced regardless of the powertrain configuration used.
- Methods marked with a plus sign (+) are public and can be called at will
- Methods with a minus sign (+) are protected or private, and can not be called by the user. These methods are used internally, but included here for completion.

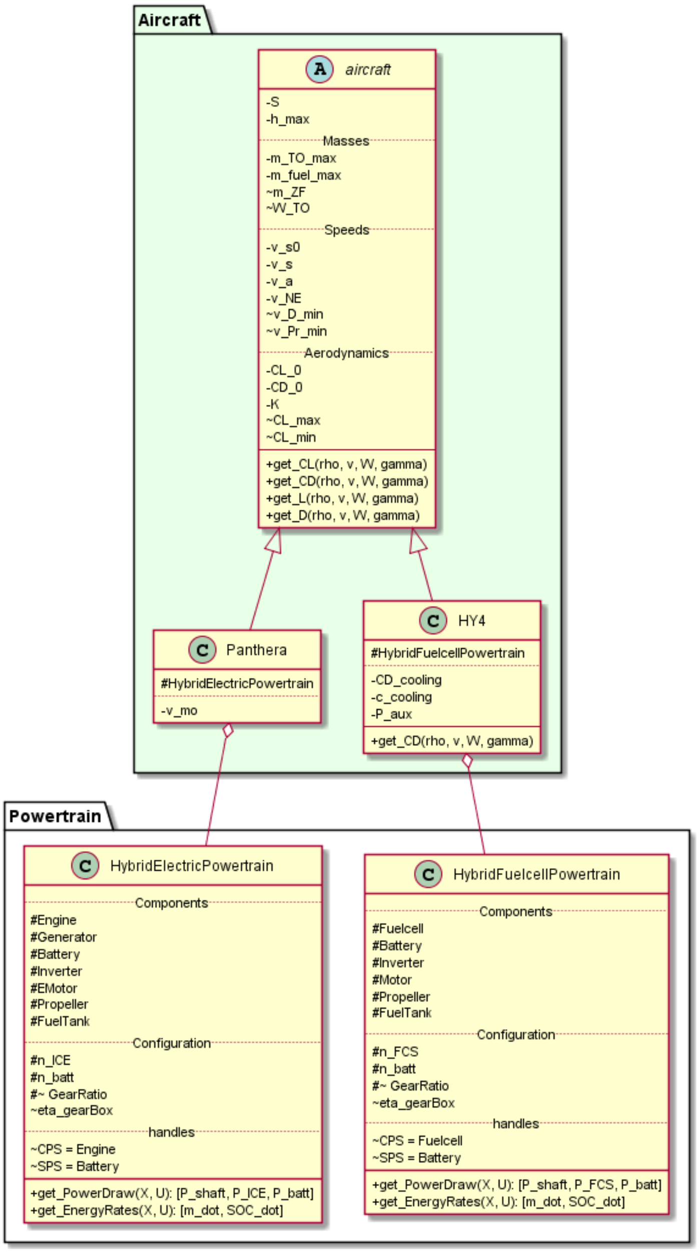

Figure C.1: Partial class diagram showing aircraft objects

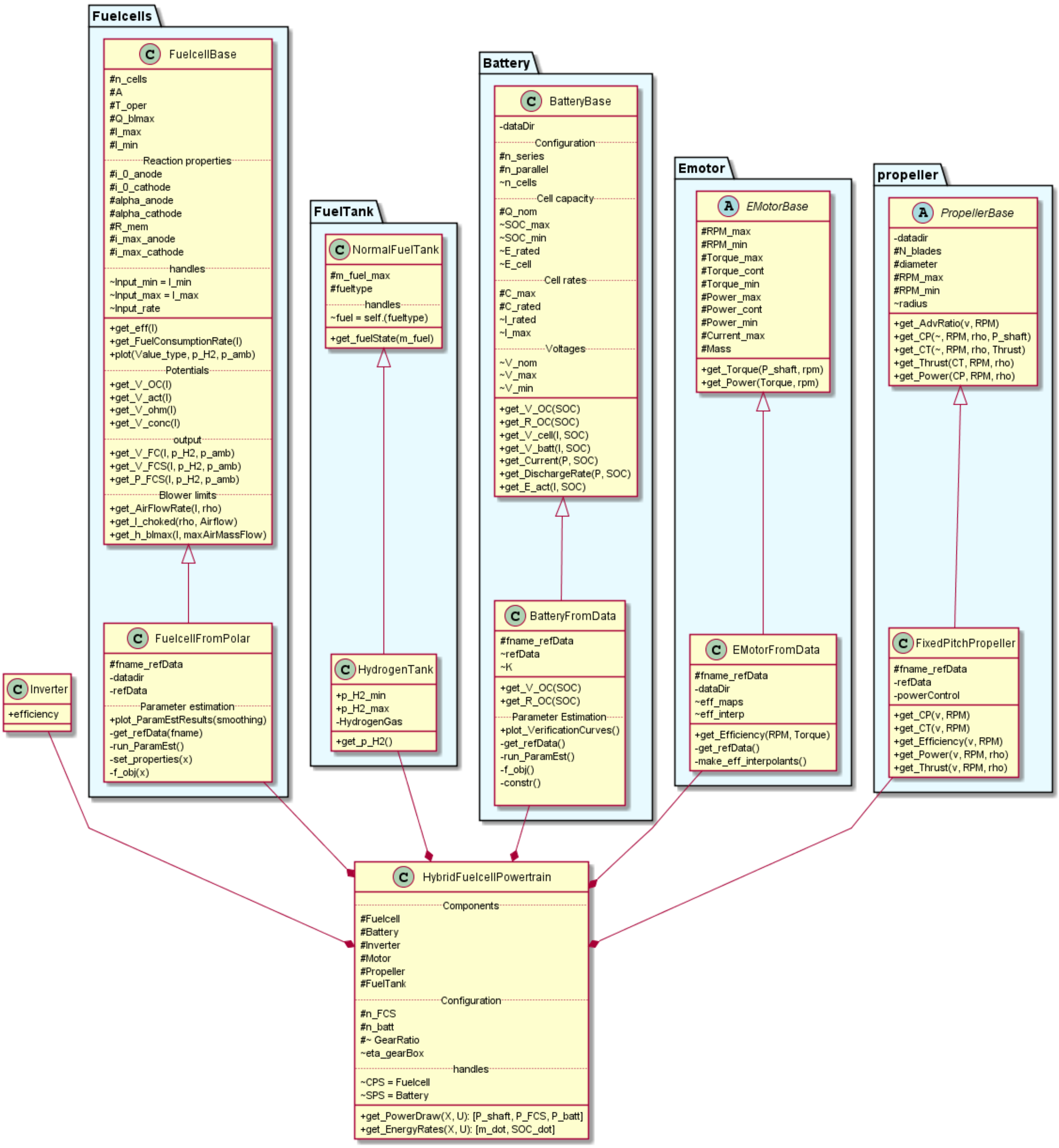

Figure C.2: Partial class diagram of the hybrid fuel cell powertrain

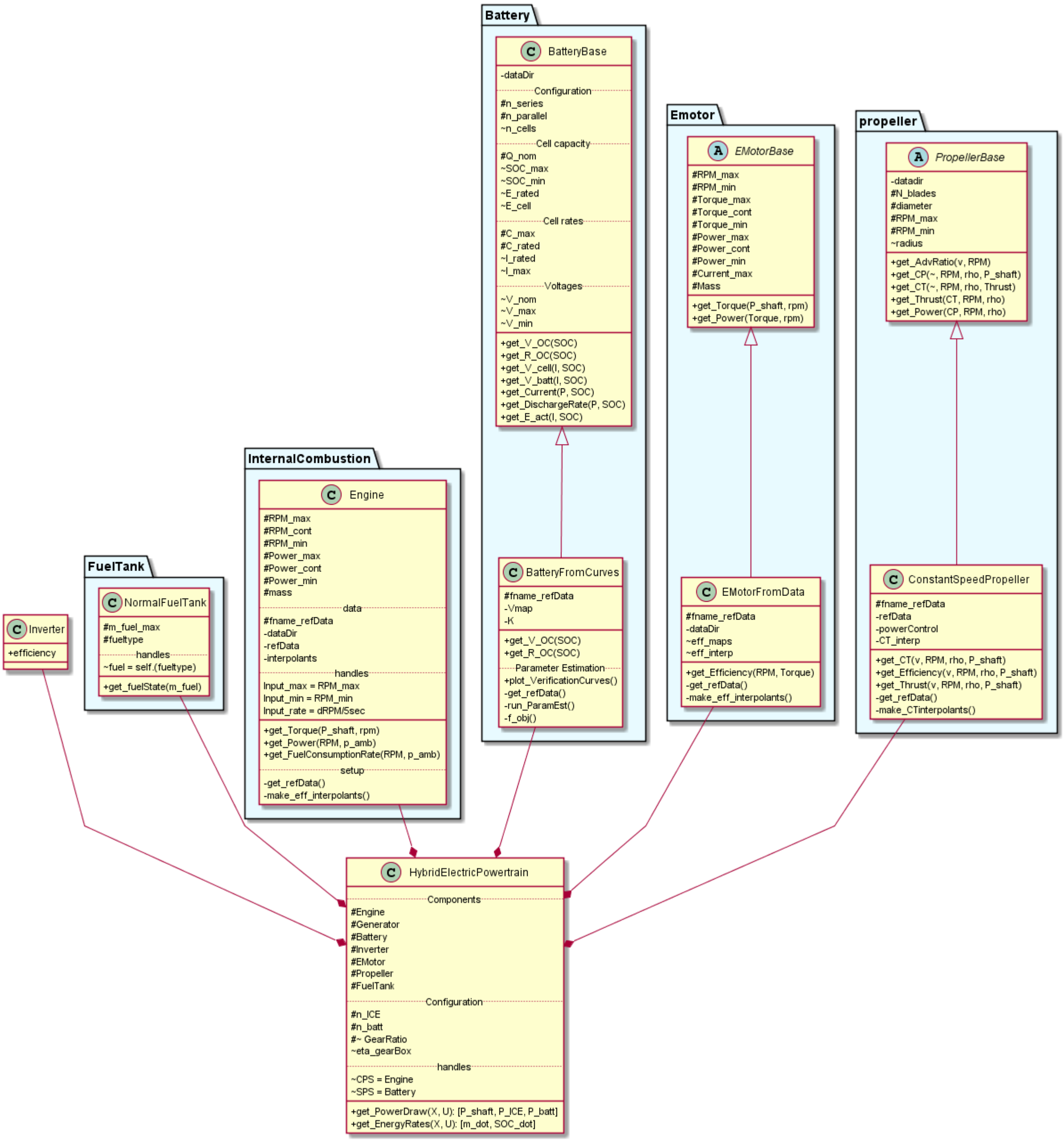

Figure C.3: Partial class diagram of the hybrid electric powertrain

Figure C.4: Complete class diagram of both aircraft

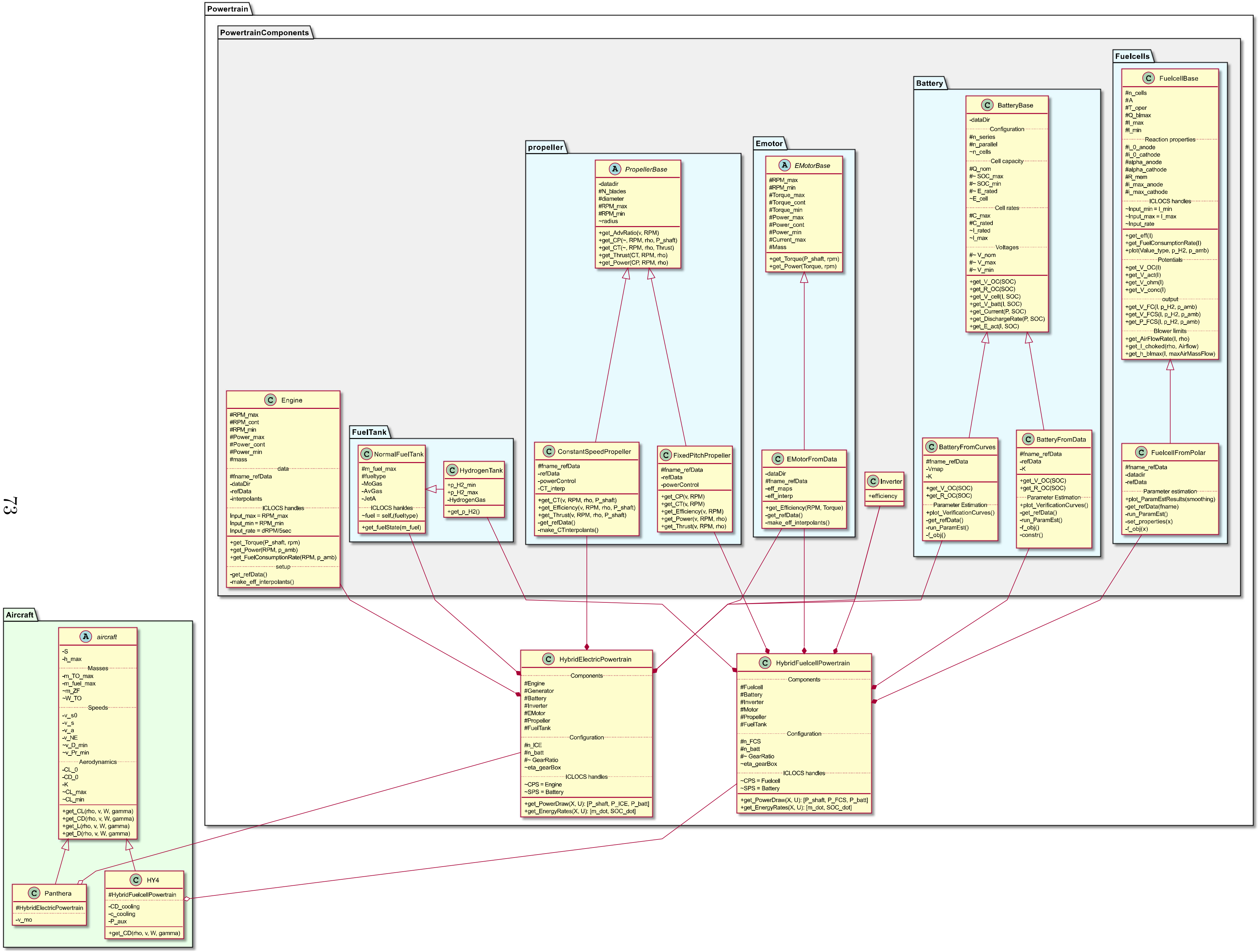

This page is intentionally left blank.

# D Point-mass Dynamics Model

A simple sketch of the point-mass model is shown in Figure D.1. $L$ and $D$ represent the lift and drag forces respectively, $W$ is the aircraft weight, $T$ is the thrust produced, and $v$ is the true airspeed. $\alpha$ is the angle of attack, e.i. the angle between the airframe body axis $x_b$ and the velocity vector axis $x$. The flight path angle $\gamma$ is the angle between the horizontal axis $x_h$ and the airspeed vector axis $x$.

Summing the forces parallel and perpendicular to the velocity vector yields Equations D.1 and D.2 respectively [19, 40]. Lift is assumed to equal weight of the aircraft times the cosine of the flight path angle. Therefore, the right-hand term in Equation D.2 is assumed to equal zero, and any changes in local curvature of the flight path or changes in flight path angle are assumed to be the result of pilot input only. [43, 44]

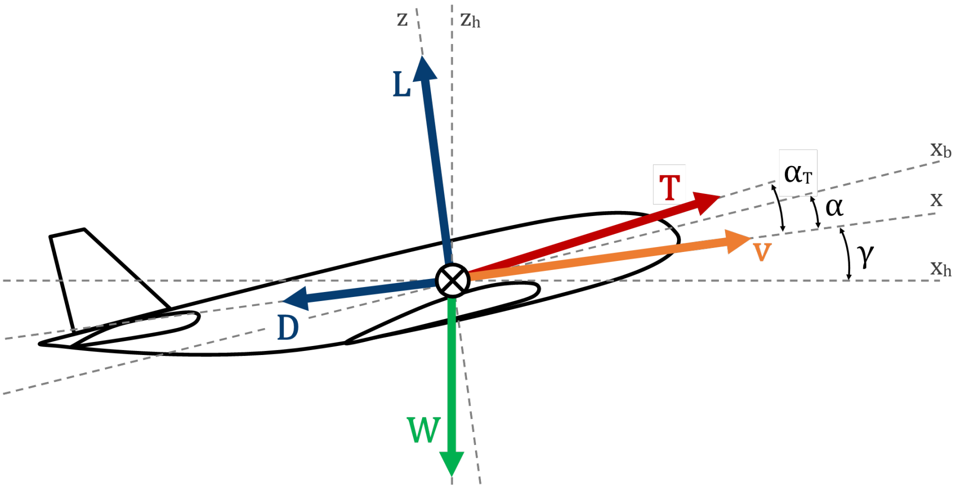

Figure D.1: Point-mass model diagram

$$\sum F_{\parallel v} \quad : \quad T\cancelto{1}{\cos\alpha_T} - D - W\sin\gamma = m\dot{v} \tag{D.1}$$

$$\sum F_{\perp v} \quad : \quad L - W\cos\gamma + T\cancelto{0}{\sin\alpha_T} = mv\cancelto{0}{\dot{\gamma}} \tag{D.2}$$

From Equation D.1, an expression for the change in true airspeed, $\dot{v}$, can be derived, shown in Equation D.3. Substituting Equation D.4 in Equation D.2 yields the expression for the lift coefficient in Equation D.5.

$$\dot{v} = \frac{T - D}{m} - g_0 \cdot \sin\gamma \tag{D.3}$$

$$L = \frac{1}{2}\rho v^2 S C_L \tag{D.4}$$

$$C_L = \frac{W\cos\gamma}{\frac{1}{2}\rho v^2 S} \tag{D.5}$$

The horizontal and vertical components of the airspeed are the ground speed or distance rate, $\dot{d}$, and climb rate, $\dot{h}$, respectively, as shown in Equations D.6 and D.7.

$$\dot{d} = v\cos\gamma \tag{D.6}$$

$$\dot{h} = v \sin \gamma \tag{D.7}$$

## Additional Assumptions

The point-mass dynamics model is subject to the following additional assumptions:

$\alpha_T = 0$
: The thrust angle is zero, and therefore thrust vector is in-line with the velocity vector.

$mv\dot{\gamma} = 0$
: Change in flight path angle due to lift force is ignored. Lift force equals the weight of the aircraft times the cosine of the flight path angle, and any local radius of curvature of the flight path are solely due to control inputs. [43, 44]

# E Additional Mathematical Background on Direct Transcription

## E.1 Construction of the Interpolating Polynomial and Collocation Constraints for Hermite-Simpson Collocation

The cubic Hermite spline is determined by first defining a simple cubic polynomial and its derivative, given in Equations E.1 and E.2. If the length of a segment between two knot points is $h = t_{k+1} - t_k$, the time domain is defined as $t \in [0, h] = [t_k, t_{k+1}]$, where $k$ and $k+1$ refer to the boundary points. Using the state and derivative values in the boundary points to apply boundary constraints $x(0) = x_k$, $\dot{x}(0) = \dot{x}_k = f_k$, $x(h) = x_{k+1}$, $\dot{x}(h) = \dot{x}_{k+1} = f_{k+1}$, making it possible to determine the polynomial coefficient with Equation E.3. Substituting the coefficients in Equation E.1 yields the Cubic Hermite interpolation polynomial for that segment Equation E.4.

$$x(t) = a_0 + a_1 t + a_2 t^2 + a_3 t^3 \tag{E.1}$$

$$\dot{x}(t) = a_1 + 2a_2 t + 3a_3 t^2 \tag{E.2}$$

$$\begin{bmatrix} a_0 \\ a_1 \\ a_2 \\ a_3 \end{bmatrix} = \begin{bmatrix} 1 & 0 & 0 & 0 \\ 0 & 1 & 0 & 0 \\ -\frac{3}{h^2} & -\frac{2}{h} & \frac{3}{h^2} & -\frac{1}{h} \\ \frac{2}{h^3} & \frac{1}{h^2} & -\frac{2}{h^3} & \frac{1}{h^2} \end{bmatrix} \begin{bmatrix} x_k \\ f_k \\ x_{k+1} \\ f_{k+1} \end{bmatrix} \tag{E.3}$$

$$\begin{aligned} x(t) = x_k + f_k(\frac{t-t_k}{h}) - (\frac{3}{h_k^2}x_k + \frac{2}{h_k}f_k - \frac{3}{h_k^2}x_{k+1} + \frac{1}{h_k}f_{k+1})(\frac{t-t_k}{h})^2 \\ + (\frac{2}{h_k^3}x_k + \frac{1}{h_k^2}f_k - \frac{2}{h_k^3}x_{k+1} + \frac{1}{h_k^2}f_{k+1})(\frac{t-t_k}{h})^3 \end{aligned} \tag{E.4}$$

For the control functions simple linear interpolation is used, shown in Equation E.5 [13, 16].

$$u(t) = \frac{u_k + u_{k+1}}{2} \tag{E.5}$$

To apply the collocation constraint using the derivative form, first the derivative of Equation E.4 is taken to get a piece-wise quadratic spline which approximated the continuous dynamics functions. Equation E.6 is then used to obtain an expression for the state derivatives at the collocation points in the segment midpoint $t_{k+\frac{1}{2}}$. Since these must equal the output of the dynamics functions, substituting Equation E.6 into Equation E.7, and rearranging, yields the collocation constraint shown in Equation E.8. Finally, integrals, e.g. in the (Lagrange) objective function, are approximated using Simpson's quadrature rule, given in Equation E.9.[16]

$$\begin{aligned} \dot{x}(t) = f_k - 2(\frac{3}{h^2}x_k + \frac{2}{h}f_k - \frac{3}{h^2}x_{k+1} + \frac{1}{h}f_{k+1})(\frac{t-t_k}{h}) \\ + 3(\frac{2}{h^3}x_k + \frac{1}{h^2}f_k - \frac{2}{h^3}x_{k+1} + \frac{1}{h^2}f_{k+1})(\frac{t-t_k}{h})^2 \end{aligned} \tag{E.6}$$

$$\dot{x}_{k+\frac{1}{2}} = f_{k+\frac{1}{2}} \tag{E.7}$$

$$x_{k+1} - x_k = \frac{h}{6}\left(f_k + 4f_{k+\frac{1}{2}} + f_{k+1}\right) \tag{E.8}$$

$$\int_{t_0}^{t_f} f(t)dt \approx \sum_{k=0}^{N-1} \frac{h}{6}\left(f_k + 4f_{k+\frac{1}{2}} + f_{k+1}\right) \tag{E.9}$$

Alternatively, Kelly[9] presents a different approach, using the integral form of the dynamics constraint. The interpolation polynomials are obtained through integration in that case, instead of differentiation. First, a quadratic interpolation polynomial is constructed for the dynamics, Equation E.10. After integration, the state interpolation polynomial is obtained, which is no longer a function of the state in the final boundary point $x_{k+1}$, but only of $x_k$, $f_k$, $f_{k+\frac{1}{2}}$, and $f_{k+1}$.

Finally, writing the collocation constraint in integral form, Equation E.12, and applying Simpson quadrature from Equation E.9 to the right-hand side will result in the exact same collocation constraint found previously in Equation E.8. Figure E.1 is a reworked version of Figure 2.4 specifically showing the which information is used to construct the cubic state interpolation polynomial for HS collocation when using the integral and derivative forms of the collocation constraint.

$$\dot{x} = f(t) = \frac{2}{h^2}\left(t - t_k - \frac{h}{2}\right)(t - t_k - h)\, f_k - \frac{4}{h^2}(t - t_k)(t - t_k - h)\, f_{k+\frac{1}{2}} + \frac{2}{h^2}(t - t_k)\left(t - t_k - \frac{h}{2}\right) f_{k+1} \tag{E.10}$$

$$\begin{aligned} x(t) = x_k + f_k\left(\frac{t - t_k}{h}\right) + \frac{1}{2}\left(-3f_k + 4f_{k+\frac{1}{2}} - f_{k+1}\right)\left(\frac{t - t_k}{h}\right)^2 \\ + \frac{1}{3}\left(2f_k - 4f_{k+\frac{1}{2}} + 2f_{k+1}\right)\left(\frac{t - t_k}{h}\right)^3 \end{aligned} \tag{E.11}$$

$$\int_{t_k}^{t_{k+1}} \dot{x}dt = \int_{t_k}^{t_{k+1}} f dt \tag{E.12}$$

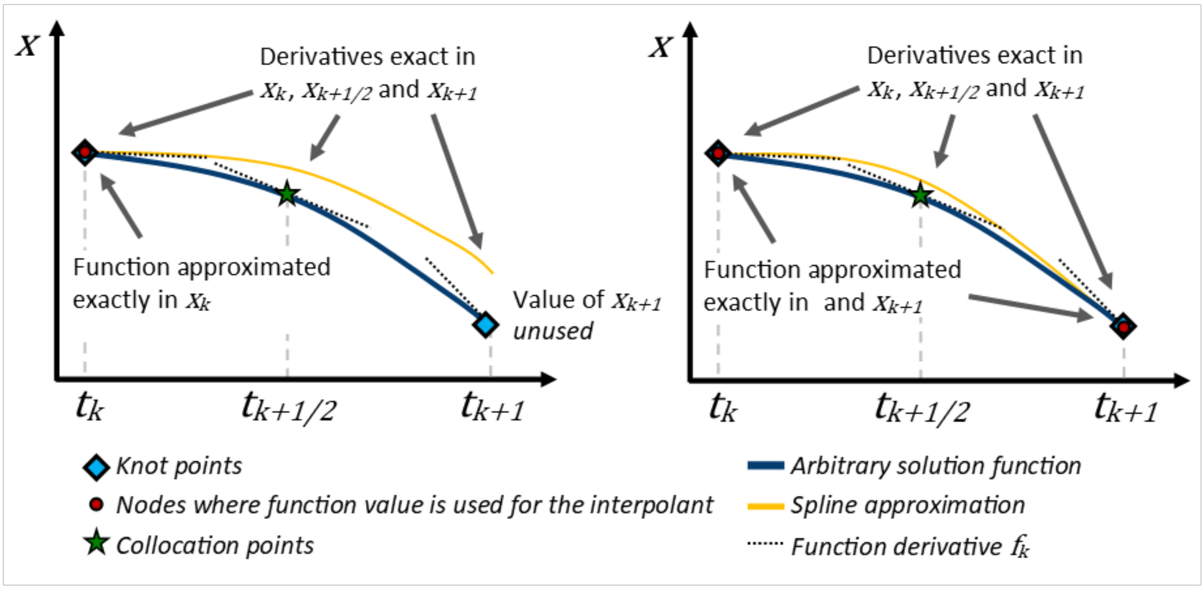

Figure E.1: Visualization of the information used to construct the cubic interpolation polynomial when using the integral (left) and derivative (right) form of the collocation constraint [8]

This approach is given here for informational purposes only, as the majority of publications agree on the derivative form being used for simultaneous transcription methods. [15, 16, 13, 14, 18]

## E.2 Construction of the Interpolating Polynomial and Collocation Constraints for Legendre-Gauss-Radau Collocation

For Legendre-Gauss quadrature, the time domain must be projected onto the normalized time domain $t' \in [-1, 1]$ using Equation E.13.

$$\tau = \frac{2t - (t_0 + t_f)}{t_f - t_0} \tag{E.13}$$

Next, $n-1$ collocation point and $n-2$ nodes are placed in the roots of the Legendre polynomial $\mathcal{P}_n(t')$, obtained from the general form given by Equations E.14 to E.16[13]. One additional node and collocation point are placed in the first knot point $t'_0 = -1$. This is equivalent to placing $n$ collocation points and $n$ nodes in the roots of $\mathcal{P}_{n-1}(t') + \mathcal{P}_n(t')$. One final node is placed in the final knot point $t'_f = 1$. The final knot point is not collocated, meaning there are a total of $n$ collocation points, but $n + 1$ nodes.

$$\mathcal{P}_0(x) = 1 \tag{E.14}$$

$$\mathcal{P}_1(x) = x \tag{E.15}$$

$$\mathcal{P}_n(x) = \frac{2(n-1)}{n} x\mathcal{P}_{n-1}(x) - \frac{n-1}{n}\mathcal{P}_{n-2}(x) \tag{E.16}$$

The $n + 1$ nodes are used to construct an integrating polynomial, given in Equation E.17, which is a linear combination of the Lagrange basis functions defined in Equation E.18. To approximate the state dynamics, the derivative of Equation E.17 yielding Equation E.19. With this information, the collocation constraints can be applied using Equation E.20.

$$x(t') = \sum_{i=1}^{n+1} \mathcal{L}_i(t') x(t'_i) \tag{E.17}$$

$$\mathcal{L}_i(t') = \prod_{j=1, j\neq i}^{n+1} \frac{t' - t'_j}{t'_i - t'_j} \tag{E.18}$$

$$\dot{x}(t') = \sum_{i=1}^{n+1} \dot{\mathcal{L}}_i(t') x(t'_i) \tag{E.19}$$

$$\dot{x}_i = f_i \ , \quad i \in [1, ..., n] \tag{E.20}$$

Finally, integrals in the objective function are approximated using Legendre-Gauss quadrature, given in Equation E.21, where the first weight is found using Equation E.22, and subsequent weights are obtained using Equation E.23. [15, 13, 14, 16]

$$\int_{-1}^{1} f(t')dt' \approx w_1 f(-1) + \sum_{i=2}^{n} w_i f\left(t'_i\right) \tag{E.21}$$

$$w_1 = \frac{2}{n^2} \tag{E.22}$$

$$w_i = \frac{1 - t'_i}{n^2 (\mathcal{P}_{n-1}(t'_i))^2} \tag{E.23}$$

# F Optimization Set-up

## F.1 Variable Bounds

The values of the bounds depend on the aircraft model used, and are determined by the aircraft object properties, or problem definition (in case of the range). The bounds imposed on the state variables are given by Equations F.1 to F.3, F.5, F.6 and F.9.

$$0 \leq d \leq range \tag{F.1}$$

$$0 \leq h \leq h_{max} \tag{F.2}$$

$$v_s \leq v \leq v_{NE} \tag{F.3}$$

$$-10 \leq \gamma \leq 10 \tag{F.4}$$

$$0 \leq m_{fuel} \leq m_{fuel_0} \tag{F.5}$$

$$SoC_{min} \leq SoC \leq 1 \tag{F.6}$$

The bounds on the control variables are given by Equations F.7 to F.10

$$0 \leq P_{shaft} \leq P_{EM_{max}} \tag{F.7}$$

$$500 \leq \Omega_{prop} \leq \Omega_{prop_{max}} \tag{F.8}$$

$$-10 \leq \dot{\gamma} \leq 10 \tag{F.9}$$

$$\begin{gathered} 0 \leq \mathcal{U}_{CPS} = I_{FC} \leq I_{FC_{max}} \\ or \\ \Omega_{ICE_{idle}} \leq \mathcal{U}_{CPS} = \Omega_{ICE} \leq \Omega_{ICE_{max}} \end{gathered} \tag{F.10}$$

## F.2 XDSM diagrams

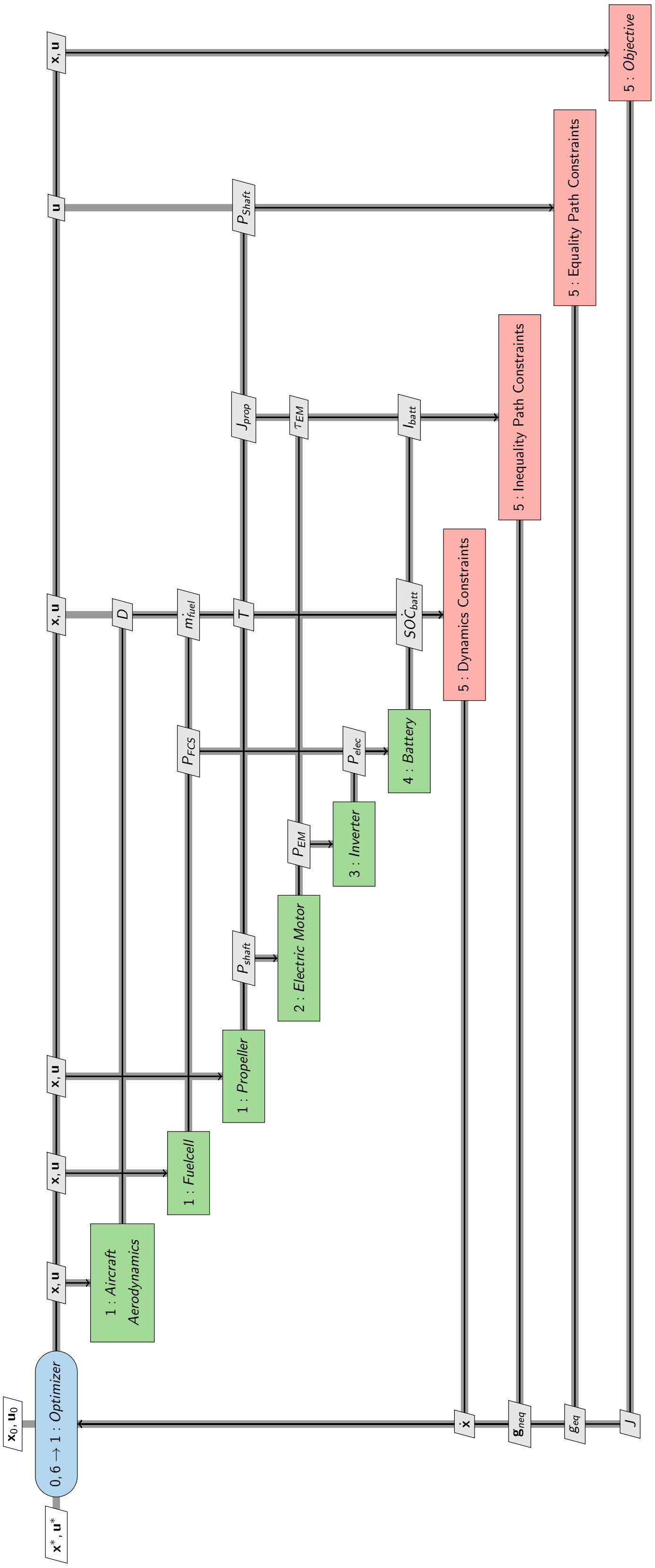

Figure F.1: XDSM diagram describing the optimization process and information flow in case of the HY4 aircraft model with fuel cells and a fixed pitch propeller.

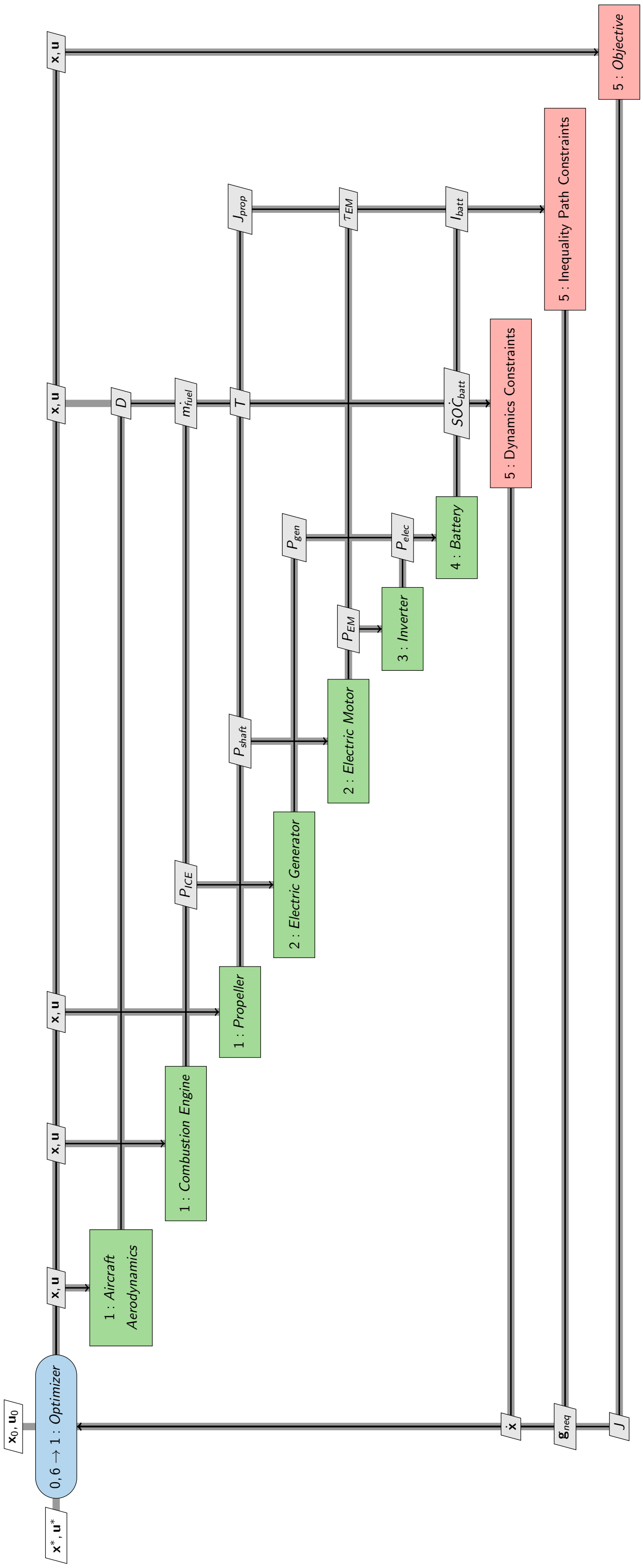

Figure F.2: XDSM diagram describing the optimization process and information flow in case of the Panthera aircraft model with a piston engine-generator combo and a variable pitch propeller.

# G Optimization results plots

The "constructed" term in the figure titles indicates the plots show the constructed, or interpolated, time-continuous solutions for all state and control parameters.

## G.1 Pipistrel Panthera - Additional solution plots

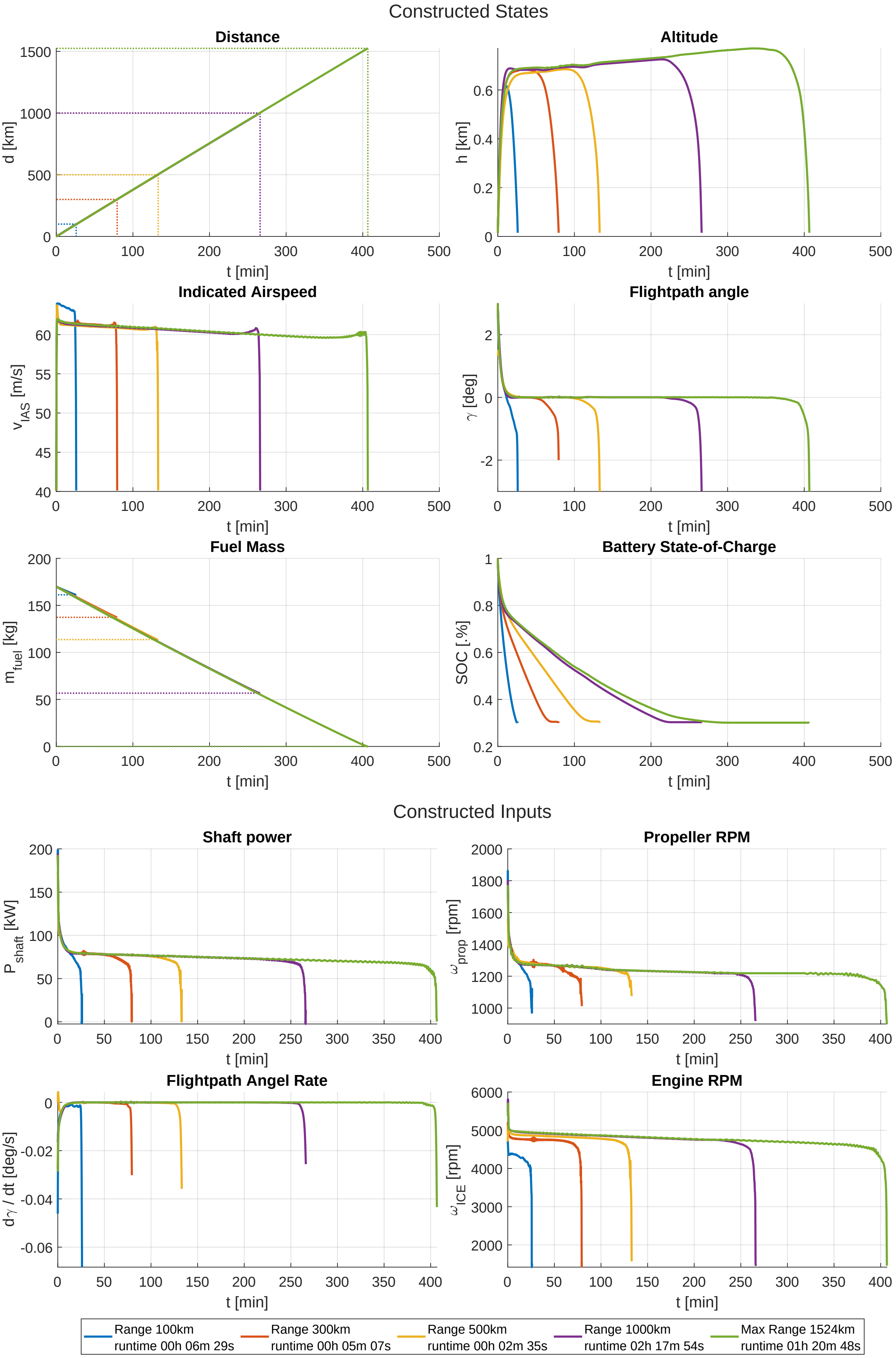

Figure G.1: Minimum Fuel optimal trajectories for the Panthera for different Ranges

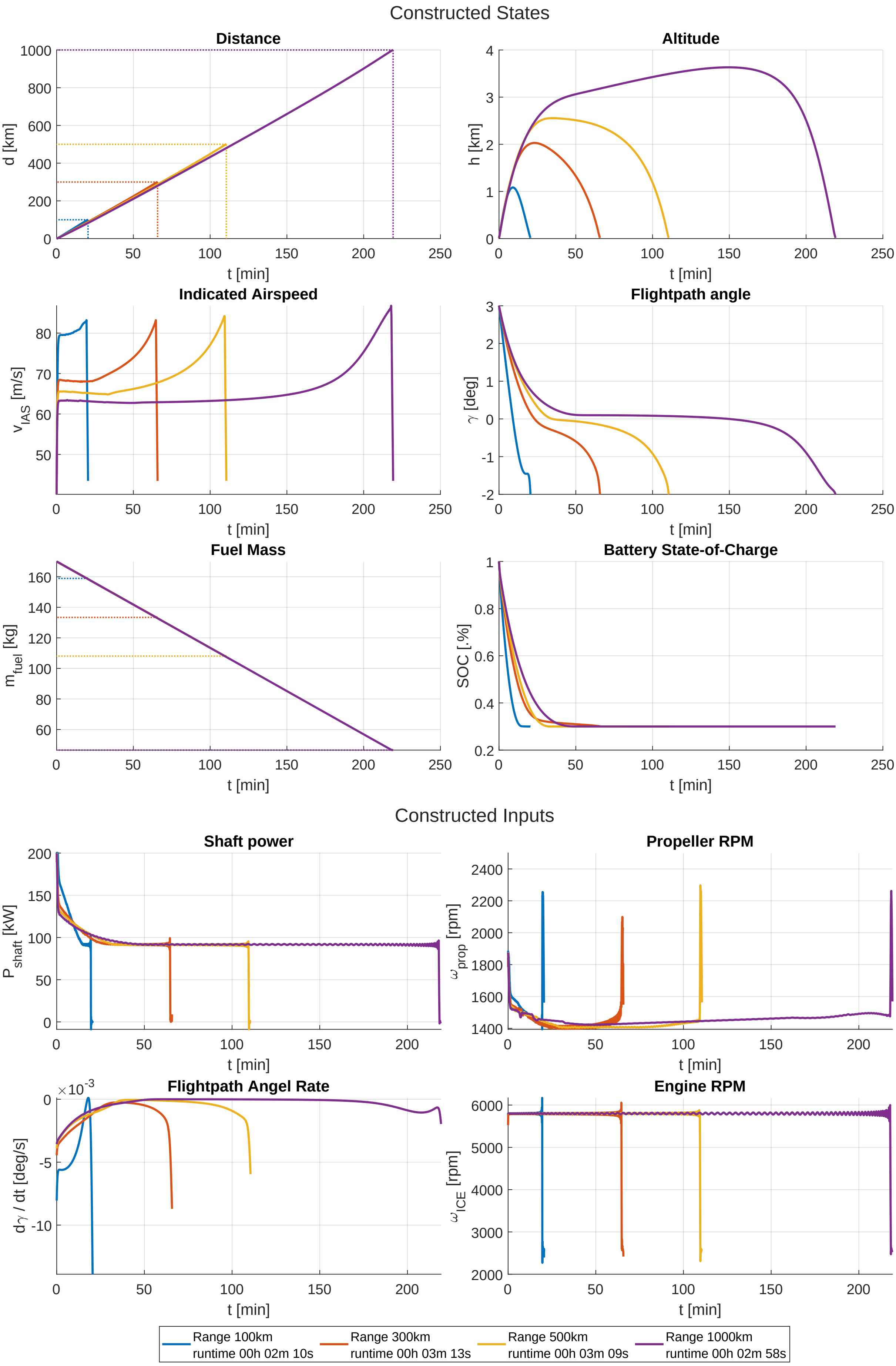

Figure G.2: Minimum Time optimal trajectories for the Panthera for different Ranges

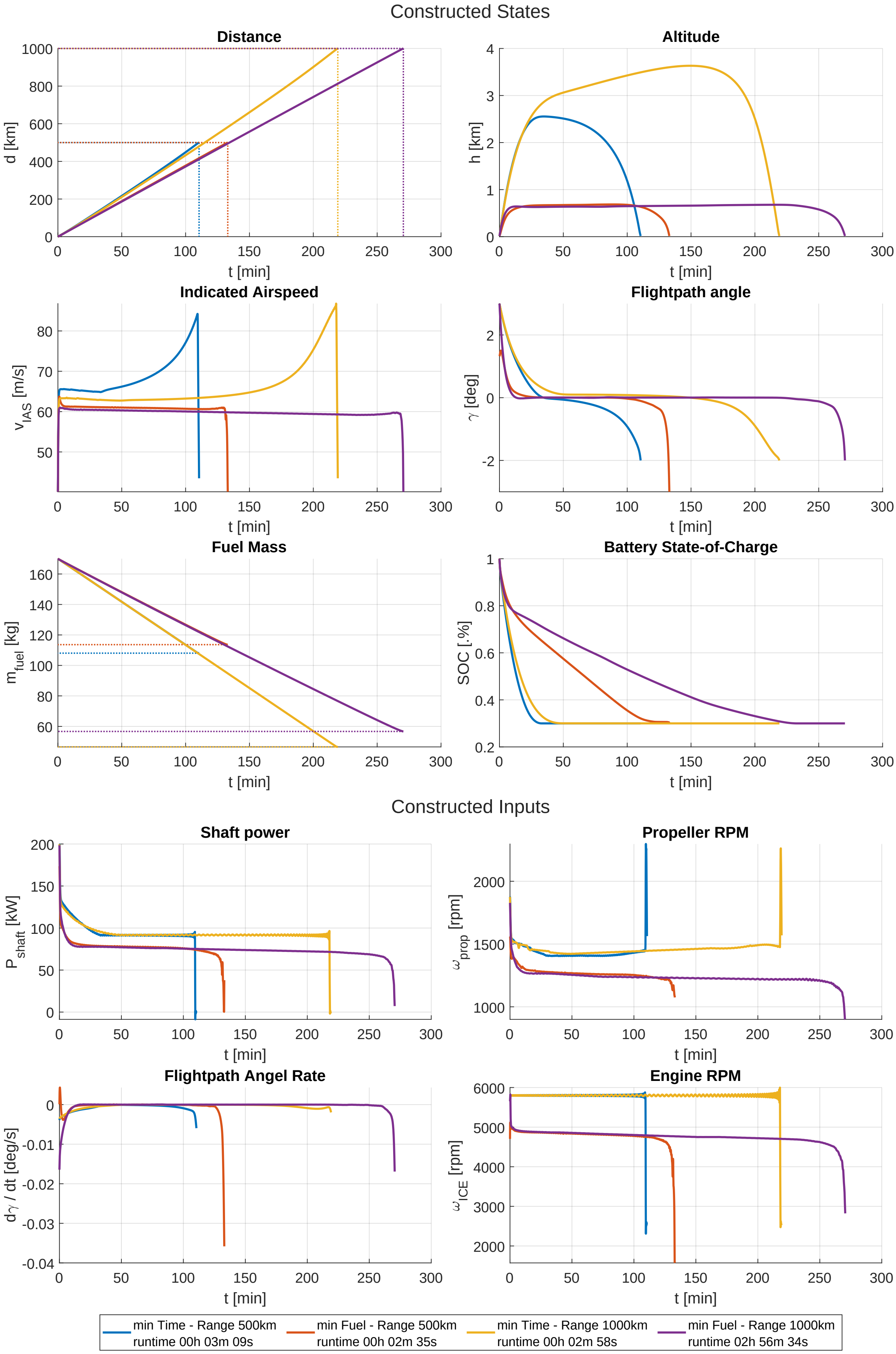

Figure G.3: Comparison between minimum fuel and minimum time results for the Panthera for ranges 500km and 1000km

### G.1.1 Single Phase Vs Multiphase results

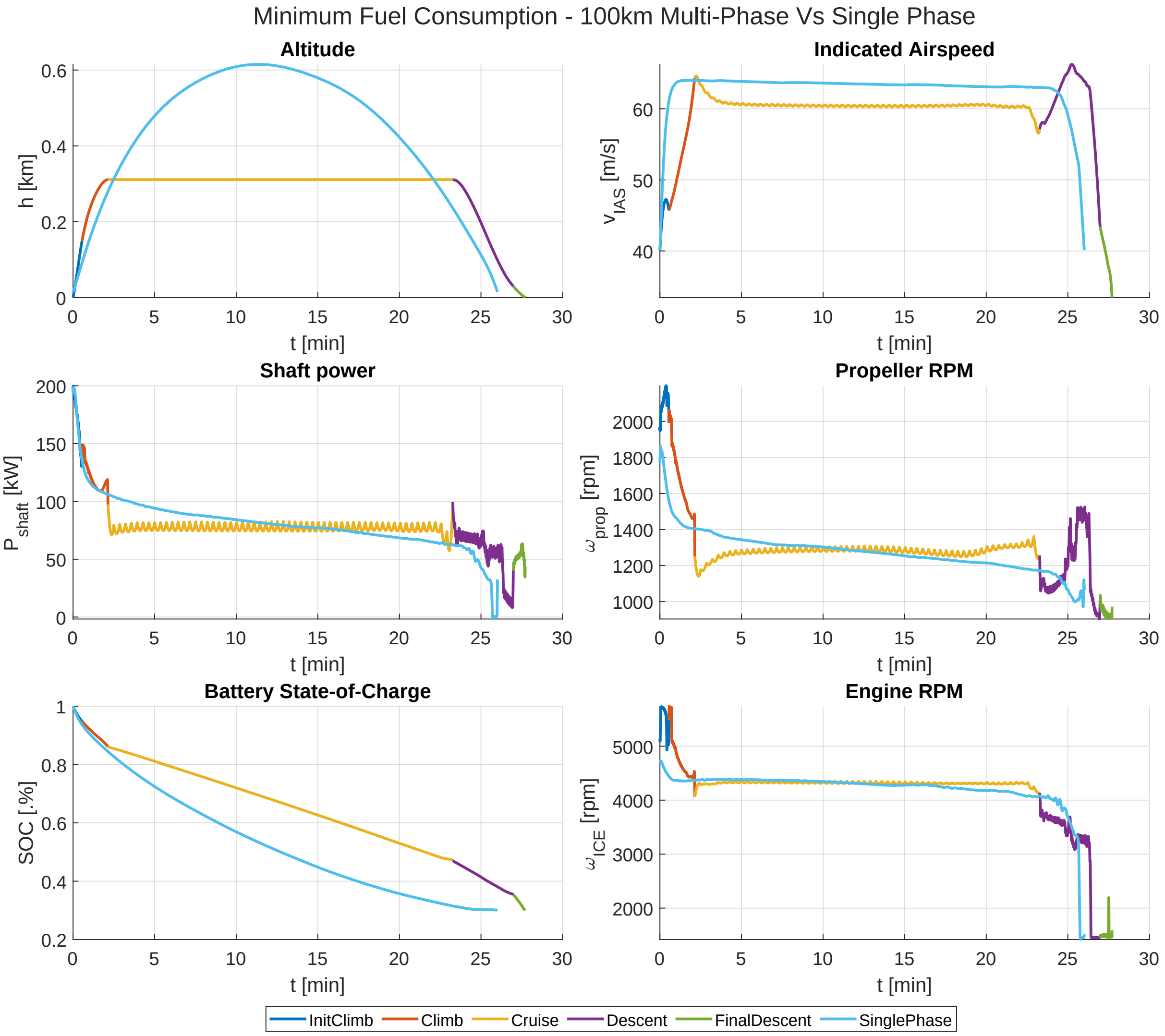

Figure G.4: Fuel-optimal single and multiphase solutions for the Panthera for a range of 100km.

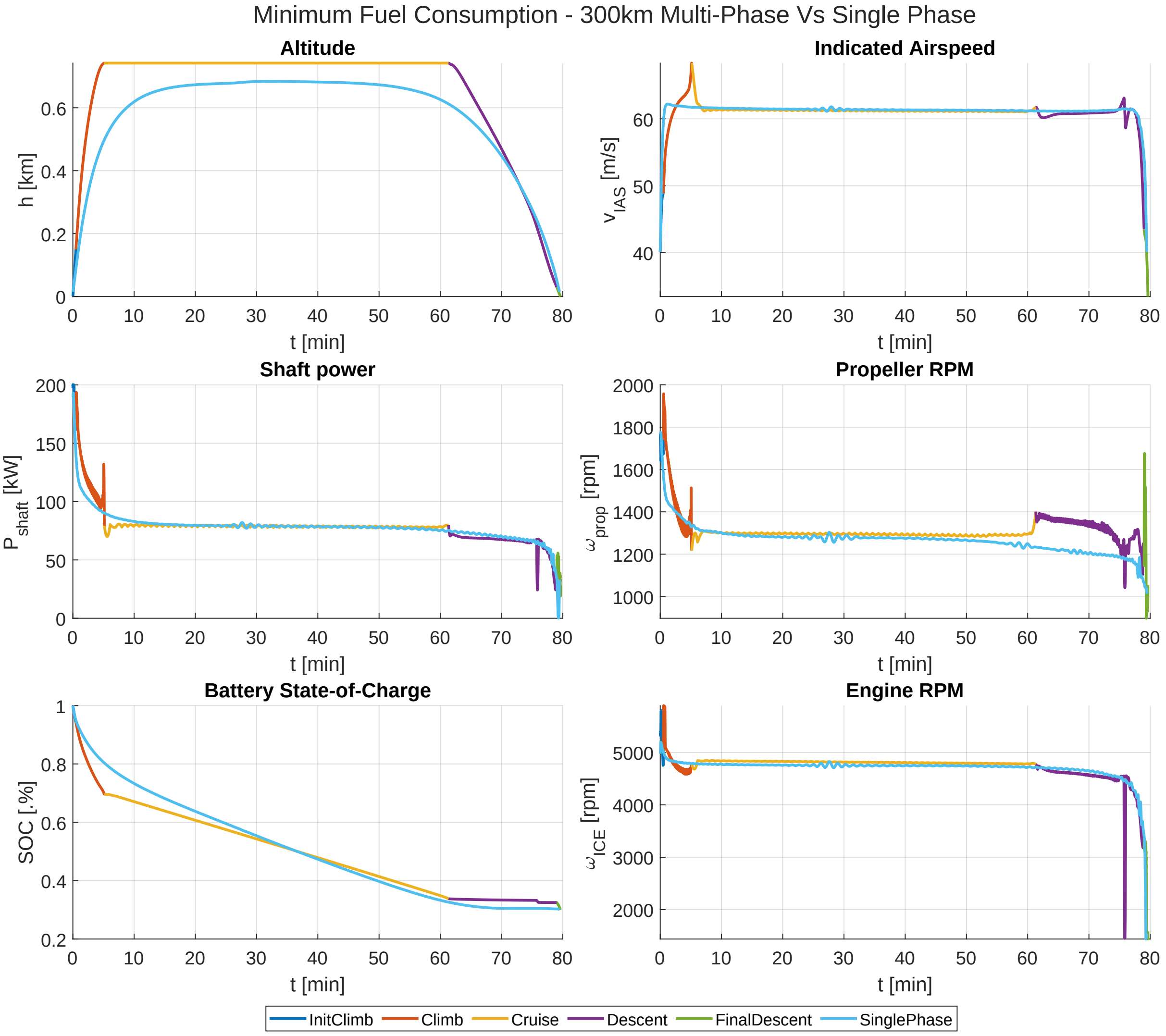

Figure G.5: Fuel-optimal single and multiphase solutions for the Panthera for a range of 300km.

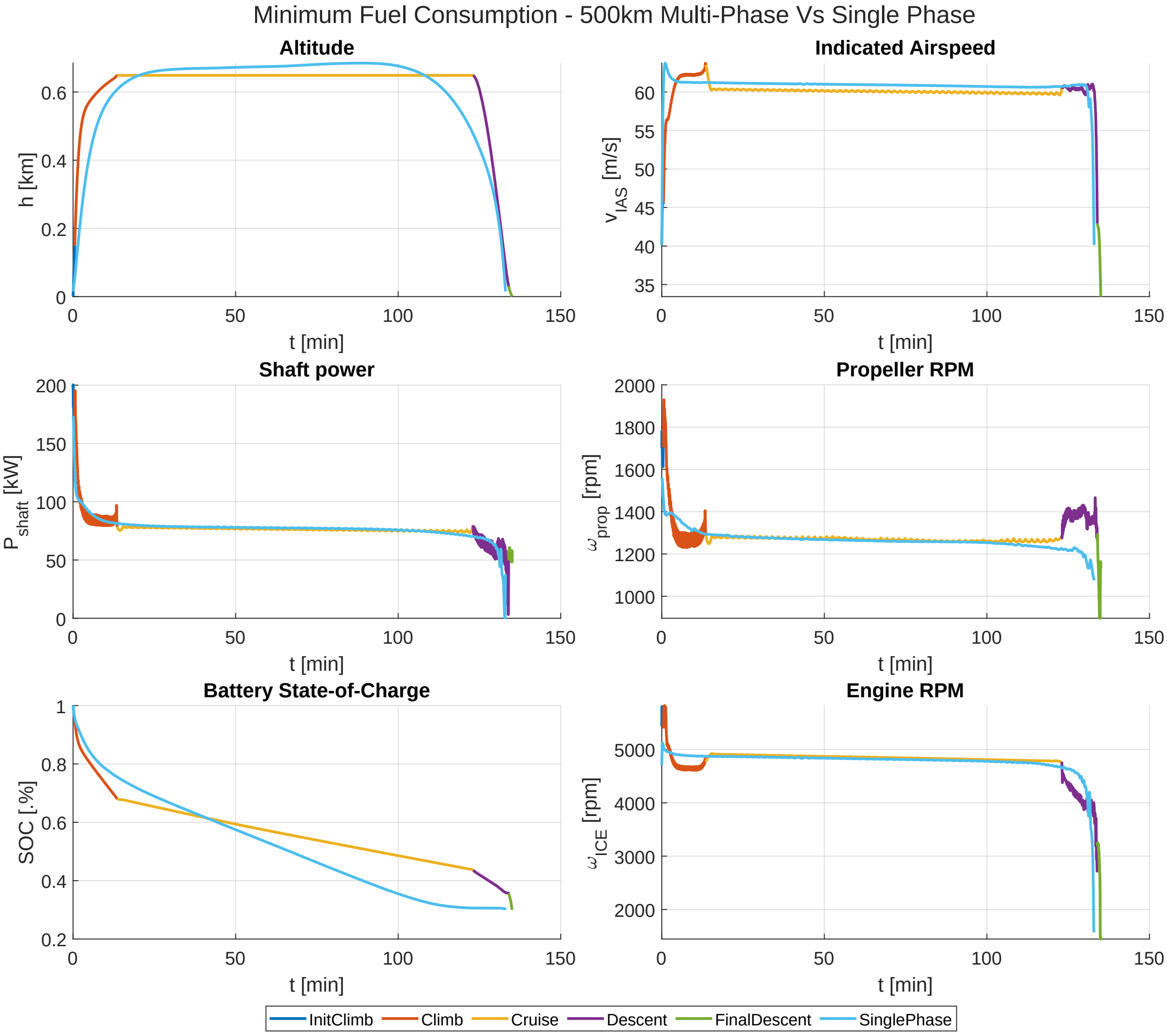

Figure G.6: Fuel-optimal single and multiphase solutions for the Panthera for a range of 500km.

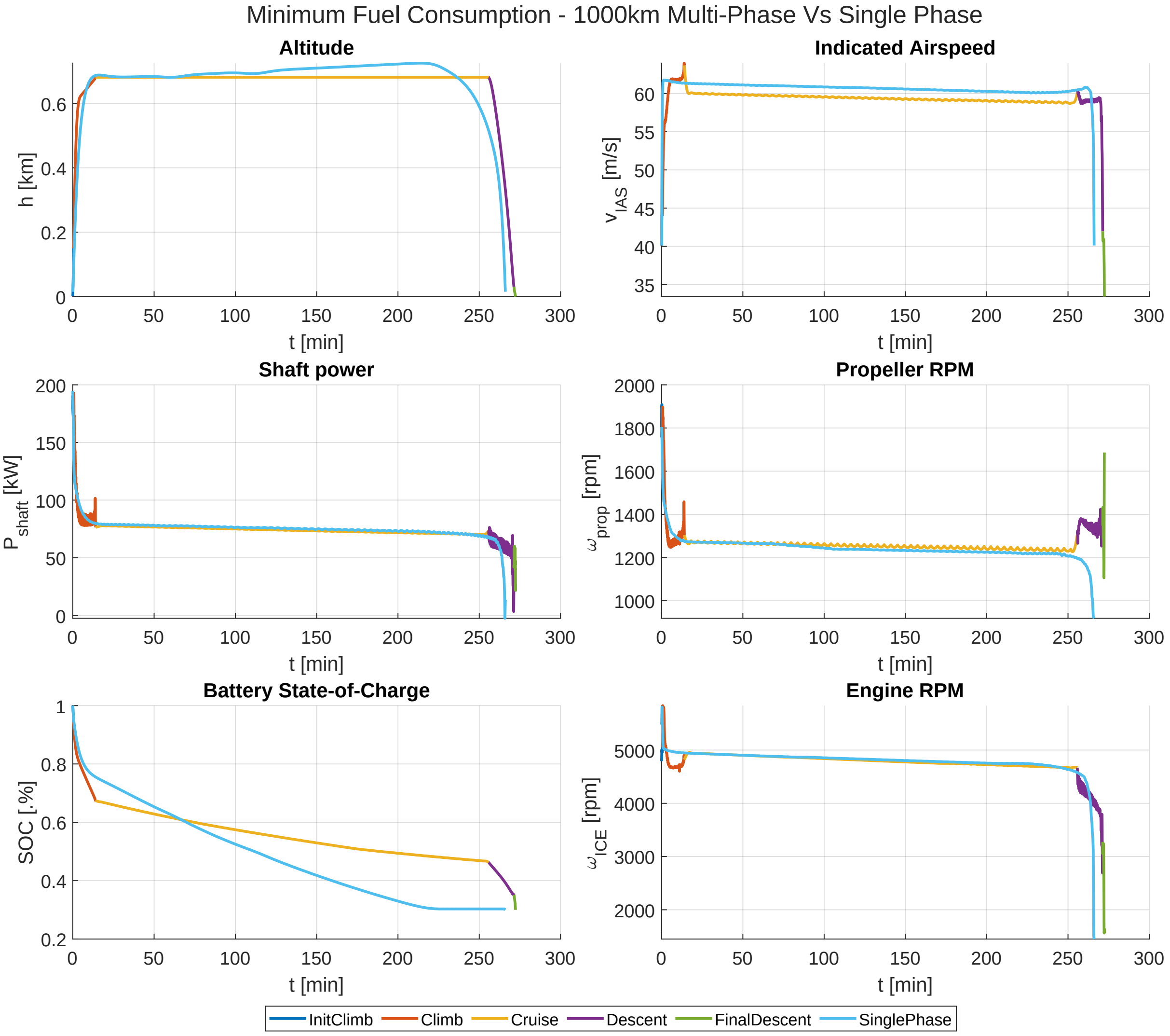

Figure G.7: Fuel-optimal single and multiphase solutions for the Panthera for a range of 1000km.

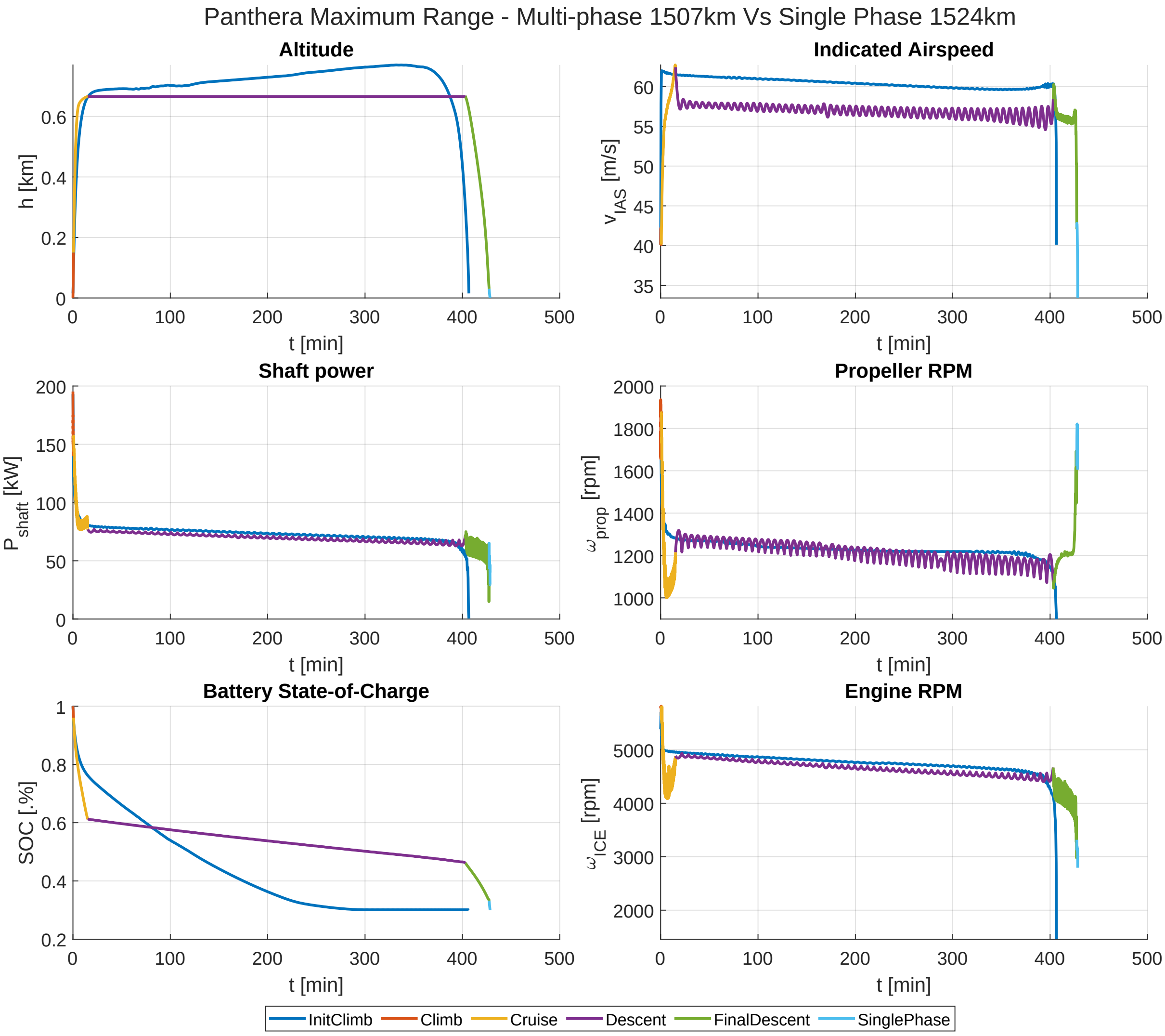

Figure G.8: Single and multiphase maximum range solution for the Panthera.

## G.2 HY4 - Additional solution plots

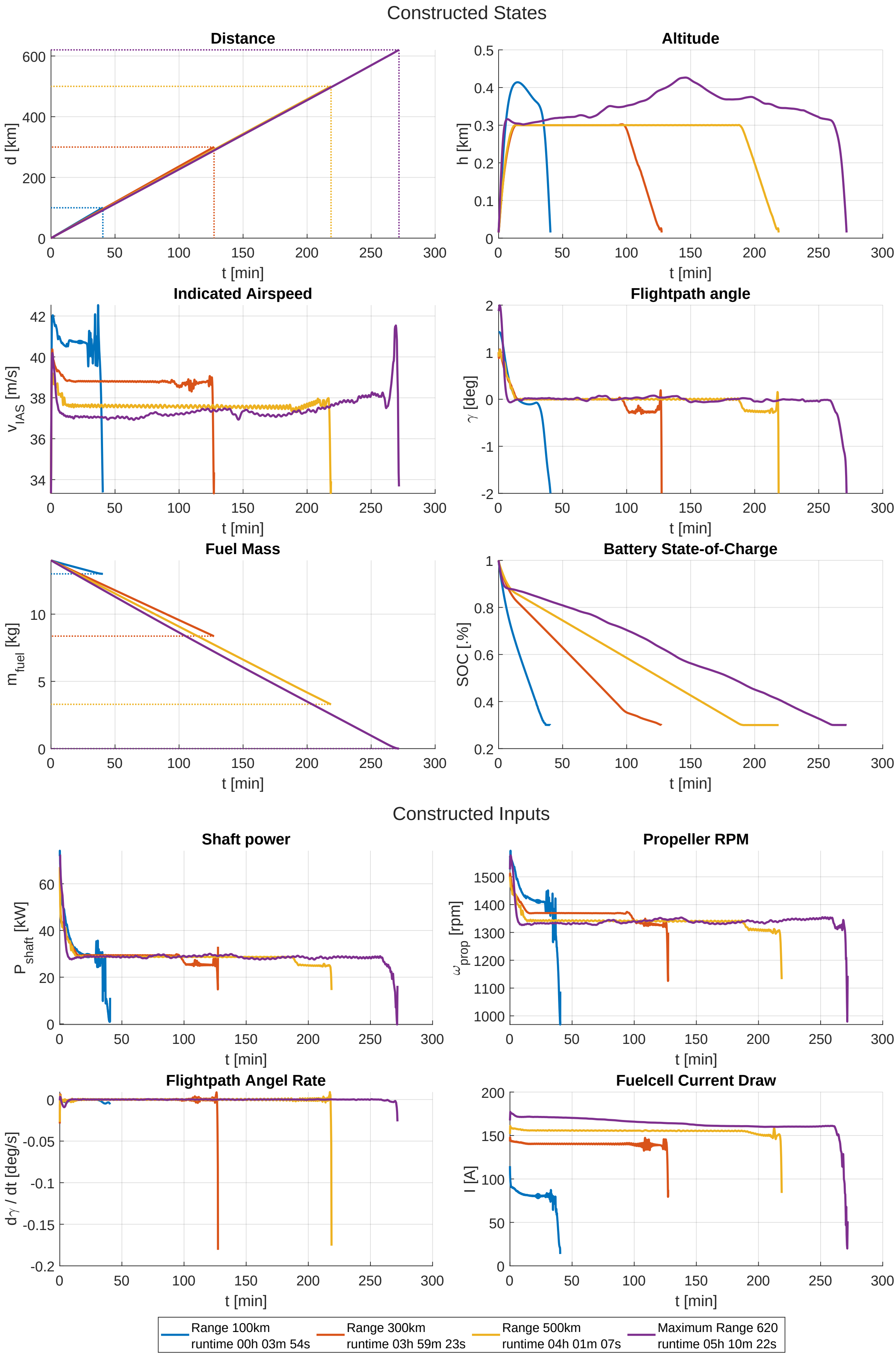

Figure G.9: Minimum Fuel optimal trajectories for the HY4 for different Ranges

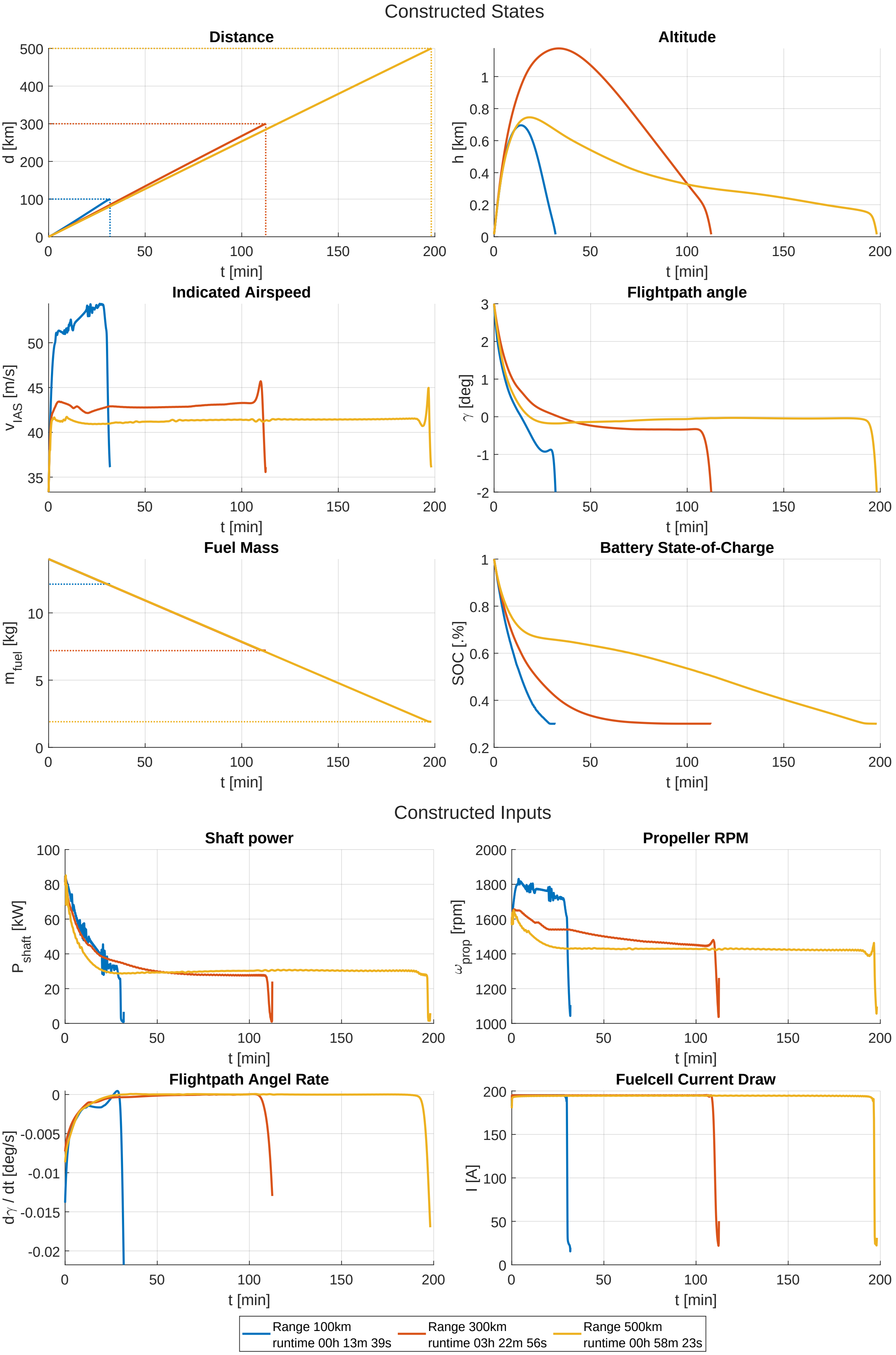

Figure G.10: Minimum Time optimal trajectories for the HY4 for different Ranges

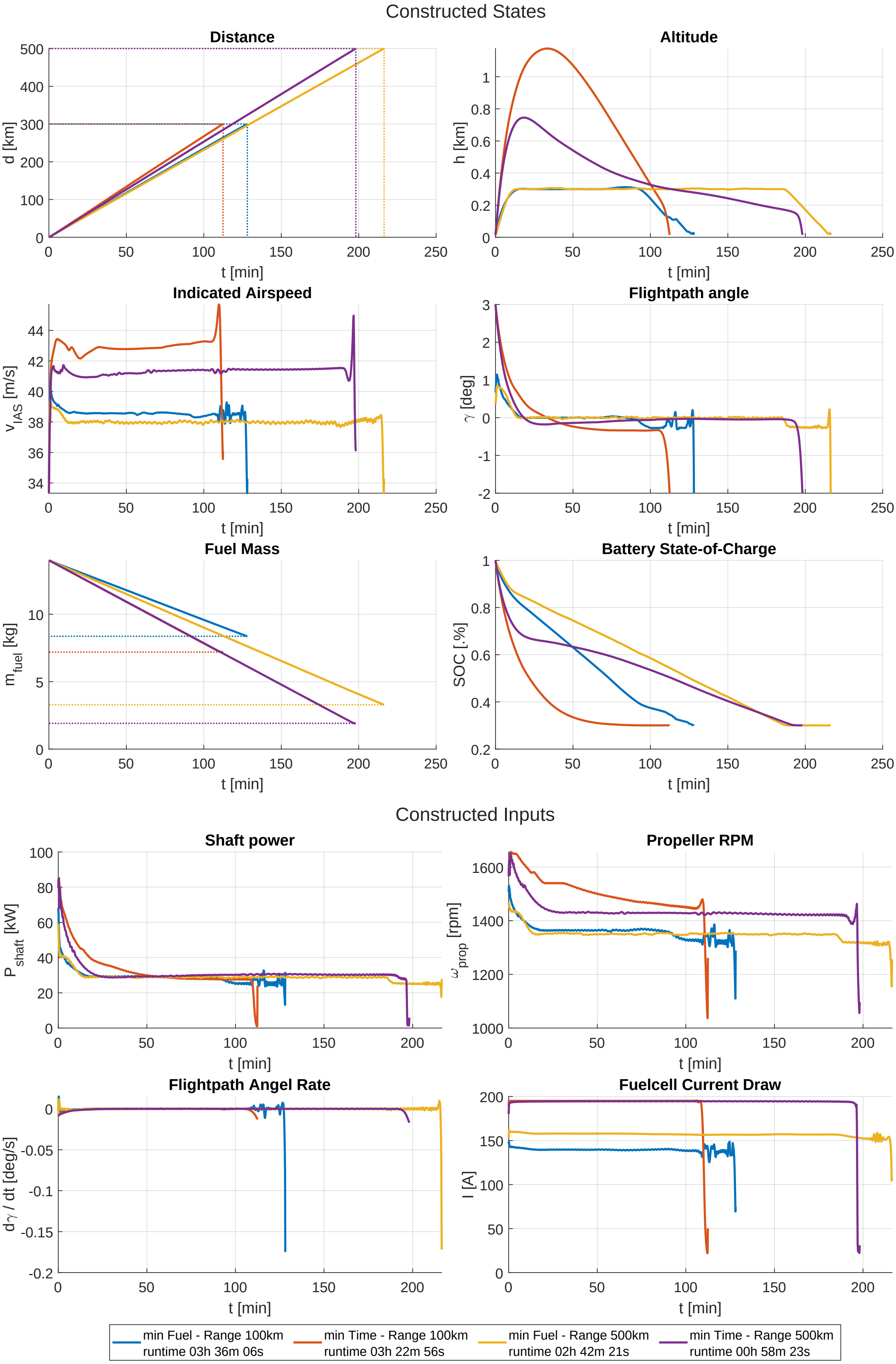

Figure G.11: Comparison between minimum fuel and minimum time results for the HY4 for ranges 300km and 500km

### G.2.1 Single Phase Vs Multiphase results

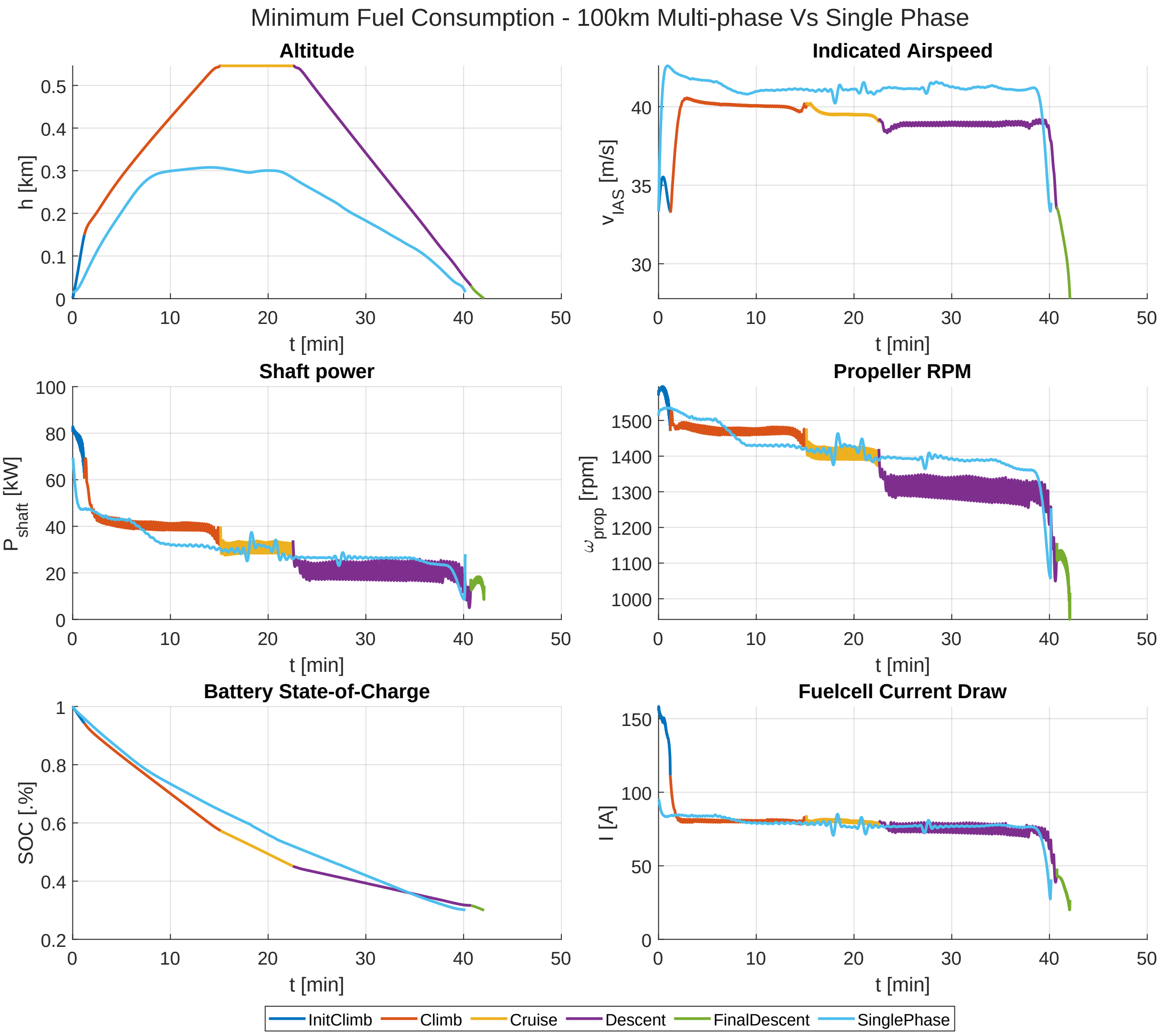

Figure G.12: Fuel-optimal single and multiphase solutions for the HY4 for a range of 100km.

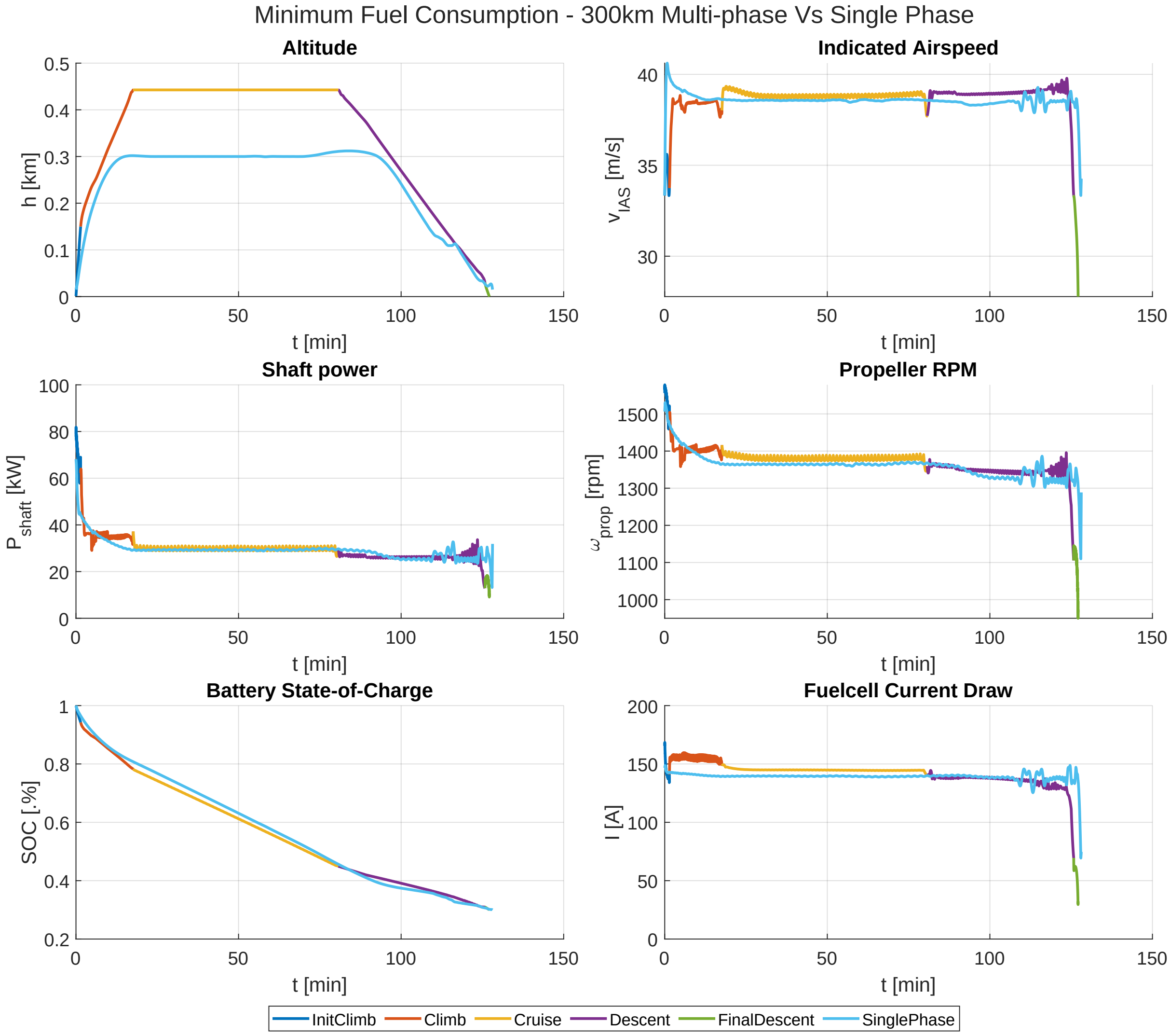

Figure G.13: Fuel-optimal single and multiphase solutions for the HY4 for a range of 300km.

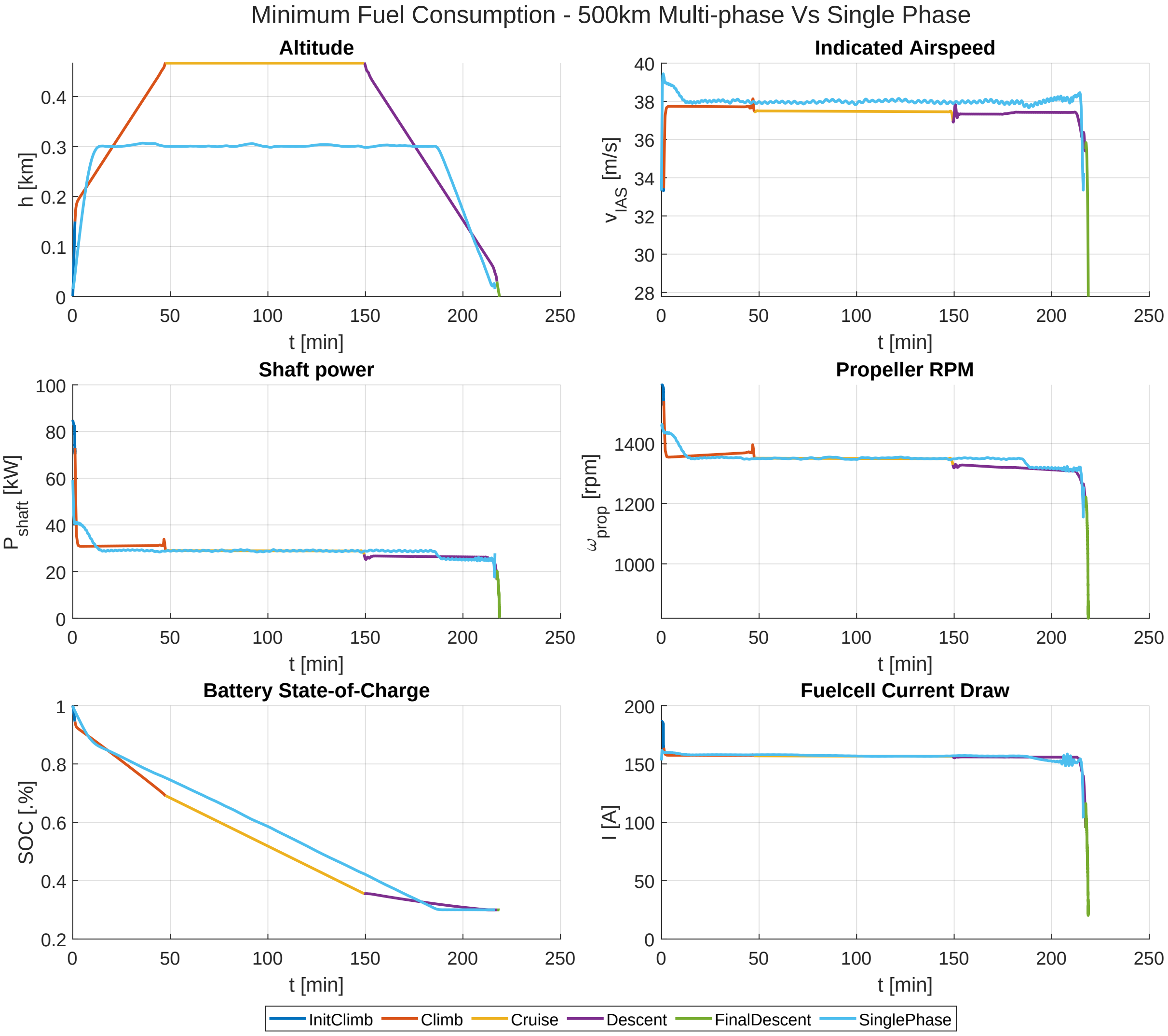

Figure G.14: Fuel-optimal single and multiphase solutions for the HY4 for a range of 500km.

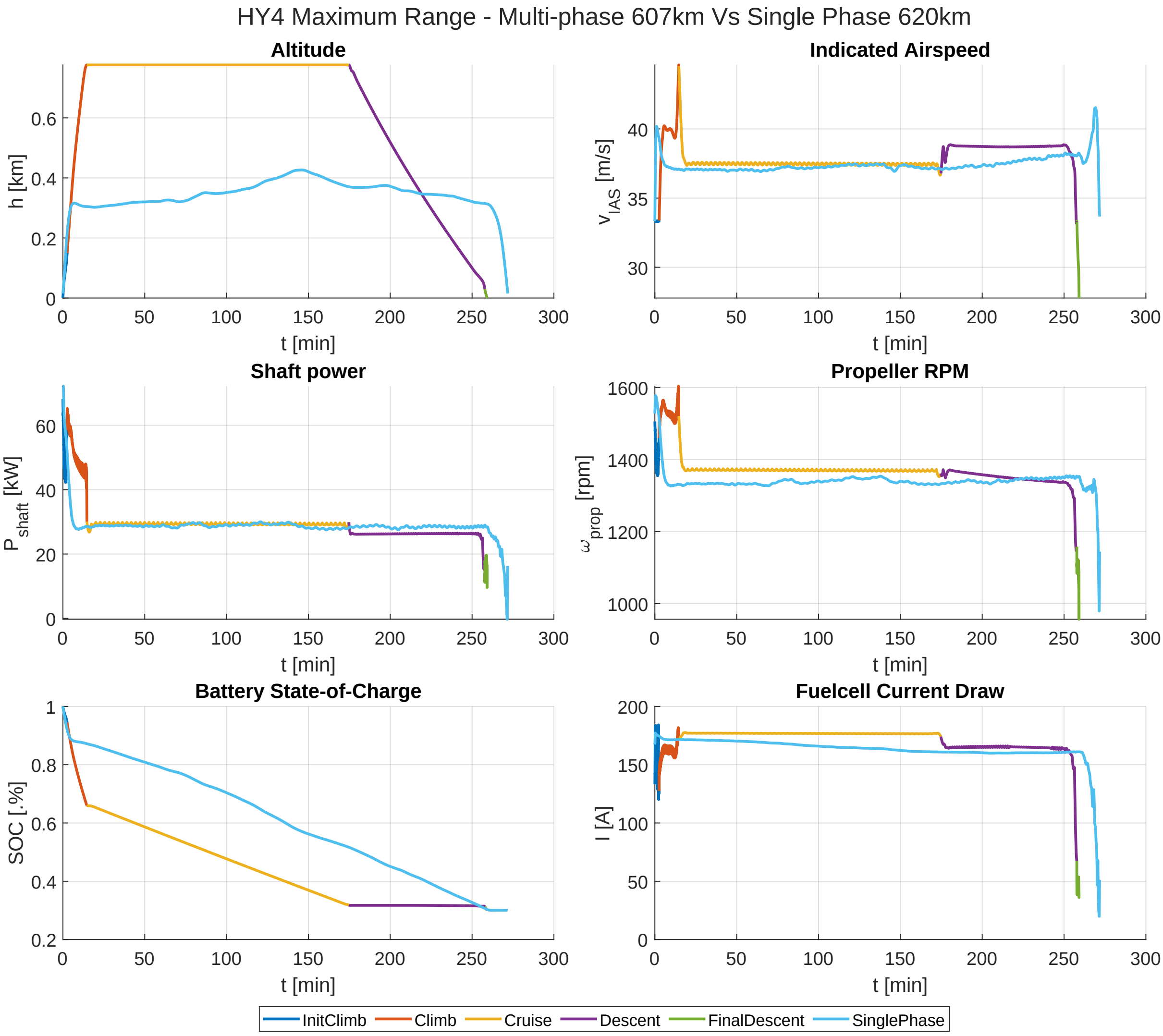

Figure G.15: Single and multiphase maximum range solution for the HY4.

### G.2.2 Trajectories With Increased Available Power

Figure G.16 shows the fuel consumption for the HY4 trajectories when increasing the available power by 10%. The trajectories themselves are plotted in Figure G.17. Figure G.18 compares trajectory results for the 300km case for different amounts of added power, compared to the base power which gave the results discussed in Chapter 6. The 10% added power is obtained by increasing inverter efficiency. The 400% power case is setup by doubling the amount of cells in each fuel cell stack, and doubling the number of fuel cell systems / stacks, meaning there are 8 fuel cells of 240 cells each in that case.

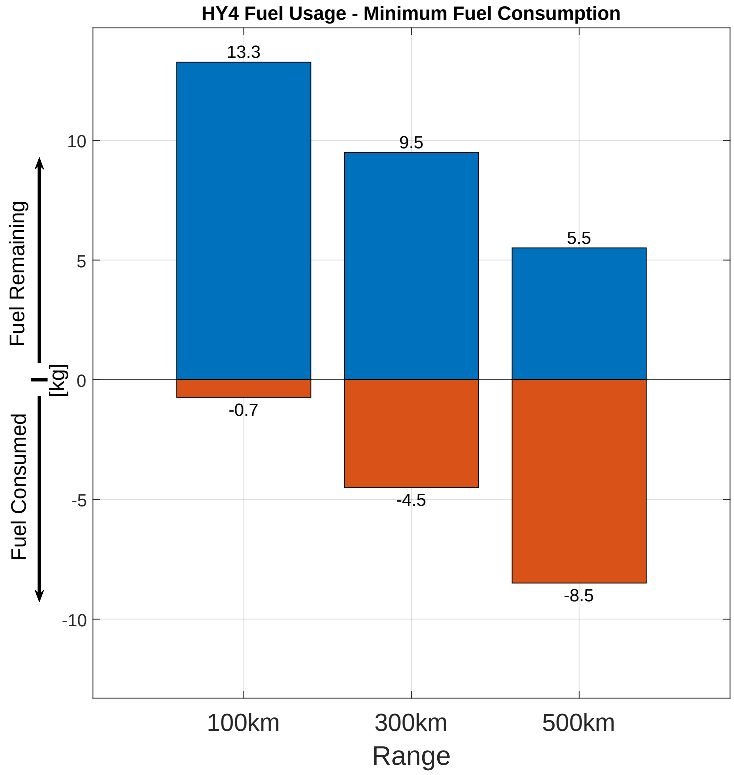

Figure G.16: Fuel consumption values for the HY4 for fuel-optimal trajectories with a 5% increase in overall powertrain efficiency.

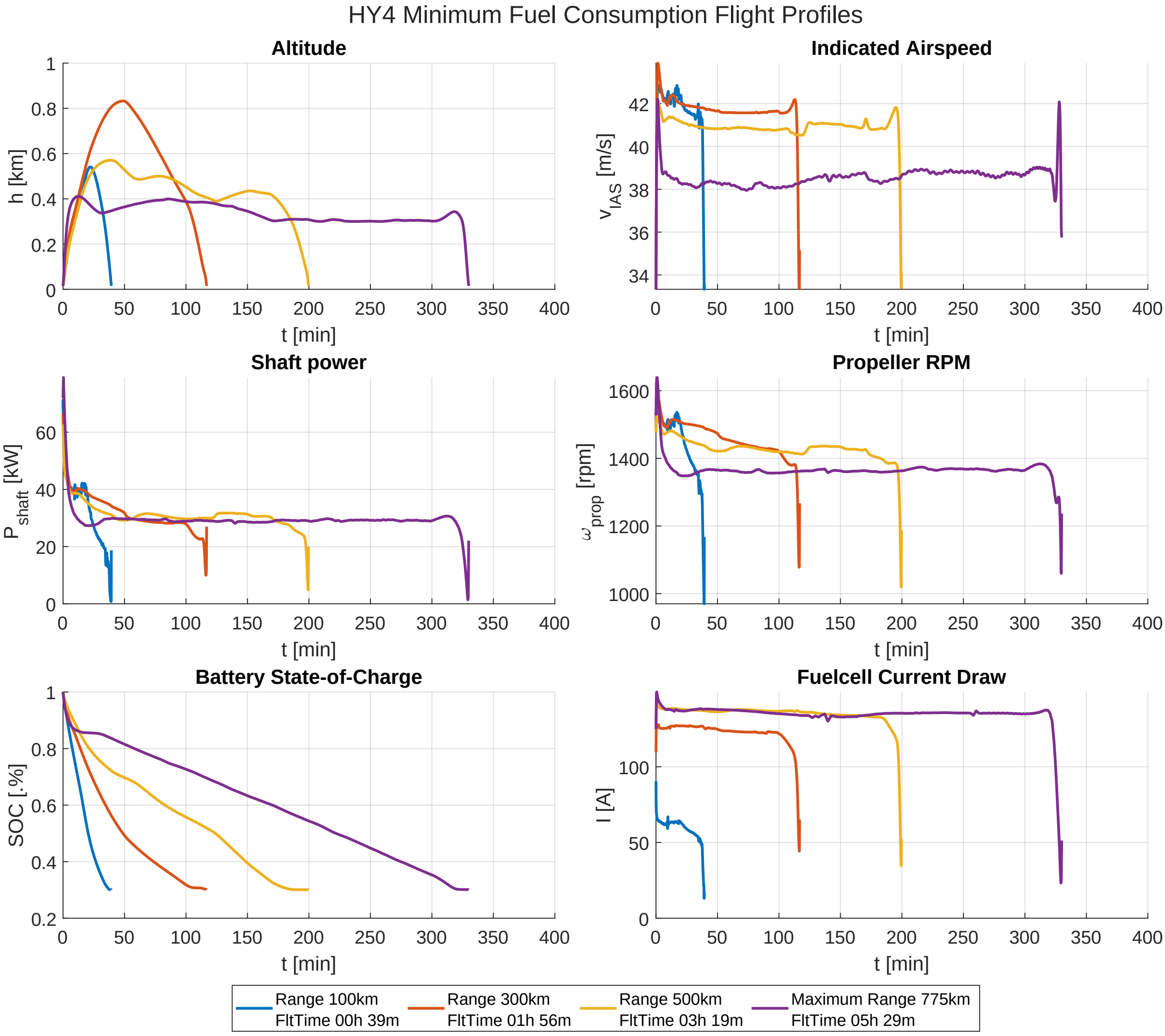

Figure G.17: HY4 fuel-optimal trajectories with a 5% increase in overall powertrain efficiency.

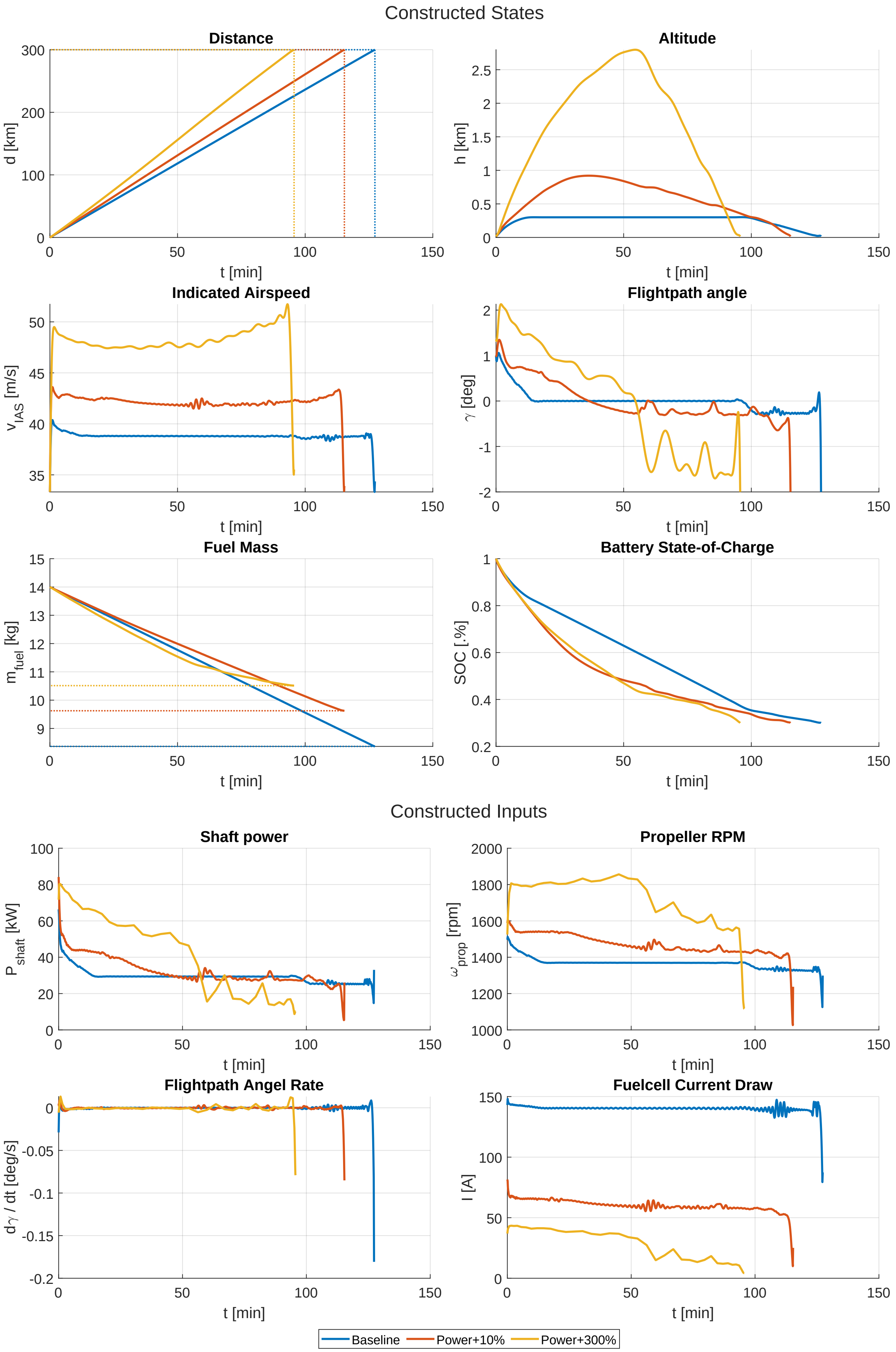

Figure G.18: Trajectory solutions for different amounts of additional power